The University Of Sheffield.

Nonlinear propagating exciton-polaritons in microcavity wires and waveguides

Lucy Estefania Tapia Rodriguez

Thesis submitted for the degree of Doctor of Philosophy

Department of Physics and Astronomy
The University of Sheffield

April 2019

Abstract

Exciton-polaritons are the quasiparticles resulting from the strong coupling between photons and excitons. The strong nonlinearity due to their particle-particle interaction and the capability of accessing their spin from outside, are of great importance for fundamental physics research and possible future applications.

In this thesis we study the nonlinear propagation of polaritons in waveguides and microcavity wires. Both systems have inherent advantages that make them promising building blocks for future polariton circuits. Whilst waveguides are easier to fabricate and usually show longer propagation distances, microwires have a characteristic energy-momentum dispersion with finite energies at k=0 which, as I will show in this thesis, is required for the formation of Cherenkov radiation and bright conservative solitons. The study of polariton propagation in both systems is necessary as they could be used for different technological applications, such as amplifiers and optical processing and transmission.

Firstly, we experimentally demonstrate amplification and nonlinear modulation of pico-Joule pulses in a polariton waveguide. We achieved a maximum gain of 4.3 dB for a pump region 0.1 mm long. We explain the interplay of nonlinearity and gain as a result of stimulated scattering from a continuous-wave reservoir of excitons and polaritons generated by the pump, that amplifies the polariton field.

In the second part of the thesis, we study propagation of conservative bright solitons in microwires and its accompanying effects. We observed Cherenkov radiation travelling in the opposite direction to the solitons emitting it. We show that the formation and propagation direction of the Cherenkov radiation is determined by the microwire polariton dispersion.

Finally, we study the polarization of bright solitons propagating in microwires. We recorded polarization precession at low excitation powers and domain formation at higher powers. We explain the observed polarization domains as a result of spin-dependent polariton-polariton interactions and an imbalance of polariton spin populations.

Publications and conferences

Publications

D. V. Skryabin, Y. V. Kartashov, O. A. Egorov, M. Sich, J. K. Chana, L. E. Tapia Rodriguez, P. M. Walker, E. Clarke, B. Royall, M. S. Skolnick and D. N. Krizhanovskii. "Backward Cherenkov radiation emitted by polariton solitons in a microcavity wire". *Nature Communications* 8(1554), 2017.

Maksym Sich, Lucy E. Tapia-Rodriguez, Helgi Sigurdsson, Paul M. Walker, Edmund Clarke, Ivan A. Shelykh, Benjamin Royall, Evgeny S. Sedov, Alexey V. Kavokin, Dmitry V. Skryabin, Maurice S. Skolnick, and Dmitry N. Krizhanovskii "Spin Domains in One-Dimensional Conservative Polariton Solitons" ACS Photonics 2018 5 (12), 5095-5102 DOI: 10.1021/acsphotonics.8b01410

Lucy E. Tapia Rodriguez, Paul M. Walker, Helgi Sigurdsson, Ben Royall, Ian Farrer, David A. Ritchie, Alexey V. Yulin, Ivan A. Shelykh, Maurice S. Skolnick, and Dmitry N. Krizhanovskii, "Amplification of nonlinear polariton pulses in waveguides," Opt. Express 27, 10692-10704 (2019)

Conference Presentations

L. E. Tapia Rodriguez, M. Sich, J.K. Chana, D.V. Skryabin, Y.V. Kartashov, O.A. Egorov, P.M. Walker, E. Clarke, B. Royall, M.S. Skolnick, and D.N. Krizhanovskii. "Backward Cherenkov radiation in a polariton microcavity wire". *International Conference on Optics of Excitons in Confined Systems (OECS)* Bath, UK, 2017.

L.E. Tapia Rodriguez, M. Sich, J.K. Chana, P.M. Walker, E. Clarke, B. Royall, E. Sedov, A. Kavokin, D.V. Skryabin, Y.V. Kartashov, O.A. Egorov, M.S. Skolnick, and D.N. Krizhanovskii. "Polarization of conservative solitons

and backward Cherenkov radiation in a microwire". *International Conference on Terahertz Emission, Metamaterials and Nanophotonics (TERAMETANANO-3)* Uxmal, Mexico, 2018.

Invited seminar. L. E. Tapia Rodriguez "Cherenkov radiation and polariton solitons in a microcavity wire" *Seminario Francisco Mejia Lira* Universidad Autonoma de San Luis Potosi, Mexico.

Acknowledgements

First of all, I would like to thank my supervisor Dr. Dmitry Krizhanovskii for all his support from before starting my PhD to the last day. None of the research presented here could have been done without his guidance and help, as his student I am deeply grateful because he was truly involved in the investigation and helped me to grow as a researcher with patience and respect.

I would also like to acknowledge and thank Prof. Maurice Skolnick, who as an independent supervisor, gave us guidance from the beginning of the project. His ideas and advice were vital to progress throughout the research. He was always present on the group discussions and made them fruitful.

I must express my gratitude to Dr. Paul Walker, for all his help in and out of the lab. I wish to thank him especially for answer all my questions, no matter if they were really basic, with respect and politeness. And to Dr. Maksym Sich, whose direction and experience helped a lot to solve the everyday problems in the lab and to achieve all the experimental results related to solitons in the present thesis.

I wish to thank Dr. Branislav Dzurnak for introducing me to the lab at the beginning of my PhD and maintain a fun and relax work environment. And to Dr. Charles Whittaker, for helping me understanding the basic of the polaritons research and being a good friend when I had just moved to Sheffield. I was also very lucky to work in the lab with Ruggero Emmanuele and Toby Dowling, who made the time in there much more enjoyable.

Many thanks to the whole group of Low dimensional structures and devices, for making these 3.5 years a great pleasure.

I am grateful to Dr. Alfonso Lastras Martinez, who was my supervisor when doing the master degree, he is an excellent professor and person, and helped me to build skills and academic knowledge to feel confident enough to pursue a PhD in UK. And to Dr. Luis Felipe Lastras and Dr. Raul Balderas, for being very

supportive since the time I was studying the bachelors degree and for introduced me to the polaritons research.

Finally, but not less important, I wish to thank my parents for their support and love and to my brother, who I consider a very dedicated and enthusiastic person. Thanks to all my friends, in Mexico and around the world, for make this journey a real joy. And thanks to Jose Guadalupe for always saying You can do it! and for being waiting in Mexico to celebrate.

Especial thanks to the Mexican National Council of Science and Technology (CONACYT), who sponsored my PhD at the University of Sheffield.

Contents

List of Figures

Chapter 1

Introduction

Over the years, exciton-polaritons have proved their importance in basic science as well as technological applications. Since their first observation in 1992 [1], fundamental research has been done in polaritonic systems such as superfluidity [2,3] and condensation [4] and their applications have started to emerge, polariton lasers [5], logical gates [6, 7], spin switches [8] and many more devices have been proposed and developed.

One of the technological final goals of the exciton-polariton research is the development of a polaritonic optical circuit, and this dream seems to be getting closer to realization. In this context, the study of nonlinear propagation of polaritons is of vital importance.

This thesis is dedicated to the study of the nonlinear propagation of exciton-polaritons in waveguides and microwires.

On one hand, waveguides have shown important advantages over microcavities such as easier fabrication, stronger exciton-photon coupling and longer polariton propagation distances, making them suitable for applications in optical integrated circuits. The study of gain and nonlinear modulation presented in this thesis, opens the possibility of future all-optical information processors.

On the other hand, polariton microwires are also promising building blocks for future all-polariton information processing circuits, in comparison to waveguides, the shape of the energy-momentum dispersion allows the formation of conservative bright solitons and backwards Cherenkov radiation, which could be of use in information transmission. They could also be used for future polariton spinoptronic devices, and the observation of polarization domains occurring in

the propagating solitons, presented in this work, supports this possibility.

The thesis is organized as follows. Chapter 2 gives an introduction to the physics behind exciton polaritons. Especial attention is given to the two systems used in this work: polariton waveguides and microcavity wires, a summary of their main properties and fabrication techniques is included. Topics related to this thesis and studied in polaritonic systems, such as superfluidity, Bose-Einstein condensation and parametric scattering are reviewed. The second part of the chapter, as the second part of the thesis, is dedicated to the study of solitons, this chapter includes an introduction to the different kinds of solitons studied in optical systems, condensates and polariton systems.

In Chapter 3 we present the two samples and the experimental setups used for all the experiments presented in this work. Chapter 4 is dedicated to the study of nonlinear propagation of picosecond pulses in polariton waveguides. We experimentally demonstrate polariton amplification and nonlinear modulation of pico-Joule pulses at sub-millimetre length scales.

In Chapter 5 and Chapter 6 we investigate the propagation of solitons and its accompanying effects in polariton microwires. The first observation of polariton bright conservative solitons and its associated Cherenkov radiation is presented in Chapter 5.

Chapter 6 focuses on the polarization of the formed bright solitons. We experimentally observed the creation of polarization domains. The relation between this effect and the spin-dependent polariton-polariton interactions is discussed.

Finally, chapter 7 gives the main conclusions and future perspectives of the presented work.

Chapter 2

Background

The main purpose of this chapter is to present the physical background behind exciton polaritons. Microcavities and waveguides are extensively discussed as they are used to study the propagation of polaritons in the following chapters: polariton waveguides were used for the study of optical amplification (Chapter 4) and 1D microwires for the study of conservative bright solitons and its accompanying effects (Chapter 5 and 6). An introduction to the most relevant phenomena previously observed in polariton systems related to the work presented in this thesis such as parametric scattering, polariton condensation, superfluidity and soliton formation is also included.

2.1 Introduction to Exciton-Polaritons

Exciton polaritons are the bosonic quasi-particles resulting of the strong coupling between light (photons) and matter (excitons). The first prediction of strong matter-light coupling was made by Pekar in 1957 [9], and one year later, the term polariton was used by Hopfield [10] for the theoretical prediction of strong coupling between electrical dipoles (excitons) and photons in a bulk semiconductor. Bulk polaritons were experimentally observed shortly after [11–13].

After polaritons were observed in bulk crystals the transition between 3D to 2D could not be achieved until 1992, when the fabrication techniques for vertical-cavity surface emitting lasers (VCSELs) have been developed. The necessity to create new structures, and change from bulk semiconductors to 2D microcavities emerged with the aim to increase the interaction between excitons and photons,

achieving the strong matter-light coupling. Strong coupling was more difficult to observe in bulk semiconductors because excitons and photons only couple when they have the equal wavevector and energy, whilst in a 2D structure, only the in-plane wave vector has to match, which together with a bigger oscillator strength for confined excitons facilitates the observation of polaritons. In 1992, Weisbuch and his team at The University of Tokyo [1] reported the first observation of strong coupling in a GaAs microcavity, marking the beginning of microcavity exciton polariton's research.

Apart from microcavities, another kind of structure has also been used for polariton experiments, the waveguides. The polariton waveguide scheme have been investigated from the late 1980's, when Ogawa et al. observed a reduction in the group velocity of an incident light pulse transmitted through the quantum well of the structure [14]. Even though the delay time measured by Ogawa's group was the first experimental evidence of polaritons in waveguides, it was not enough to claim strong coupling behaviour. It wasn't till 2013 that direct observation of the dispersion anti-crossing (which is the clearest signature of strong-coupling) was reported [15]. Inside waveguides, the strong coupling regime is achieved by the confinement of the photonic component due to total internal reflection. They present some advantages over microcavities and are extensively discussed in section 2.4.

On the 26 years from the first observation of microcavity exciton polaritons, 2D microcavities, have enabled the study of multiple phenomena such as superfluidity [16], Bose-Einstein condensation [4], the optical spin Hall effect [17], parametric scattering [18], bright [19] and dark [20] solitons, quantized vortices [21], etc. In addition, microcavities have been modified creating new different structures to enhance certain properties of the polaritons. The fabrication of 2D microcavities, 1D microwires (and waveguides) and finally 0D micropillars, have given the opportunity to study topological effects [22] including the recent achievement of a topological insulator [23], phenomena related to polariton-polariton interactions such as polariton condensates [24] and solitons Walker2017 have also been observed in these structures and their possible applications in optical circuits make them especially interesting for future technology.

2.2 Excitons in Quantum Wells

Quantum Wells (QWs) are a fundamental part in exciton-polariton systems. They consist of thin layers (typically a few nanometers thick) of a semiconductor material with a band gap smaller than the energy band gap of the surrounding

material (Figure 2.1). Usually GaAs QWs are sandwiched by $Al_xGa_{1-x}As$ and, $In_xGa_{1-x}As$ QWs are surrounded by pure GaAs or $Al_xGa_{1-x}As$ barriers.

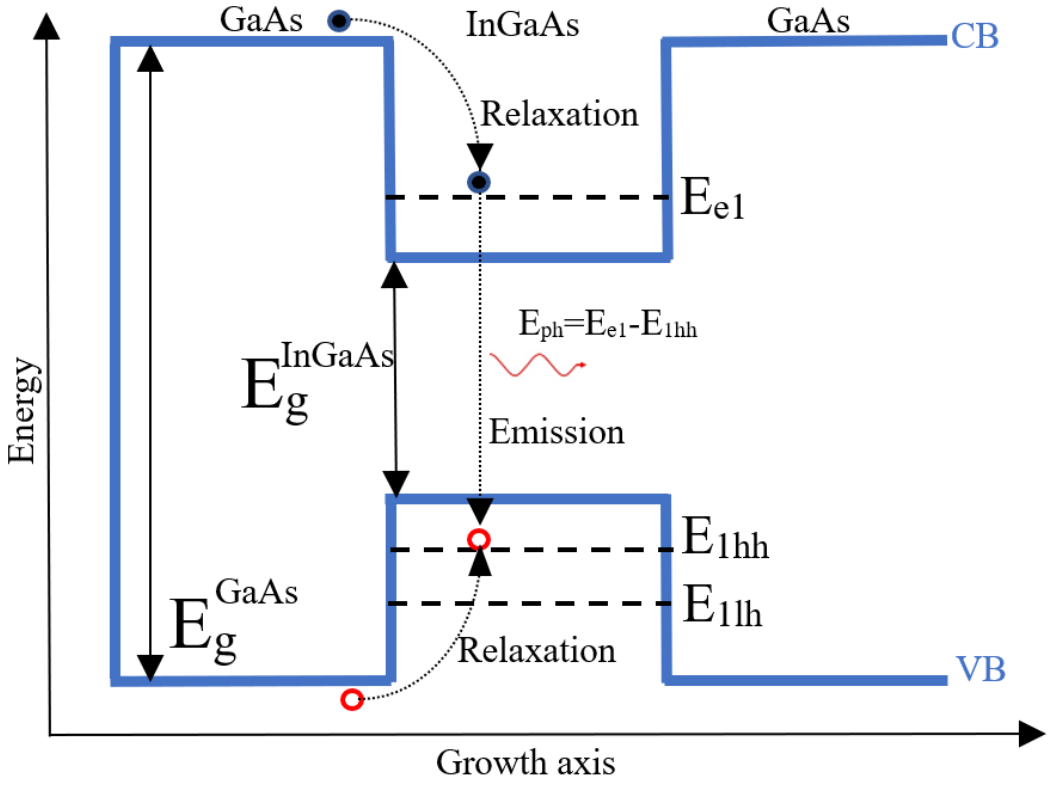

Figure 2.1: Diagram of the energy bands in a Quantum Well. The QW is formed by a heterostructure of GaAs/InGaAs/GaAs. The figure shows the electron and hole relaxation to their lowest energy bands and the recombination of the electron and heavy hole producing photon emission

When an electron is excited, it leaves a hole (with positive charge +e) in the Fermi sea of electrons of the valence band. Electrons and holes are confined in the quantum well plane (figure 2.1), and because they have opposite charges they experience Coulomb attraction and form a new bounded state known as exciton. It is called exciton because it is created by the smallest possible excitation of the system: the excitation of an electron from the valence band to the conduction band. The motion of an electron (or a hole) inside a crystal can be represented in a similar way to a free electron, but with an effective mass characteristic of the specific band. The effective mass is inversely proportional to the curvature of the band ($m^* = \hbar^2(d^2/dk^2E)^{-1}$). Exciton effective mass M_X is the sum of the electron and hole effective mass.

An important advantage of GaAs, $In_xGa_{1-x}As$ and $Al_xGa_{1-x}As$ is that they have a direct band gap, (the conduction band minimum and the valence band maximum are at the same position in k-space) making the process of exciton creation and recombination by photon emission more probable than in indirect semiconductors.

Excitons have a resonance energy below the energy band gap (E_g) due to the Coulomb attraction. Their presence is confirmed by discrete absorption peaks/dips observed in luminescence, absorption and reflection spectra. Exciton energy dispersion in bulk semiconductors is described by:

$$E_X = E_{gap} + E_{XB,3D} + \frac{\hbar^2 K^2}{2M_X} \tag{2.1}$$

Where E_{gap} is the energy gap between the valence and conduction bands, K is the center of mass wavevector and $E_{XB,3D}$ is the bulk exciton binding energy, which is given by the solutions of the particle with reduced mass $\mu = \frac{m_e^* m_h^*}{m_e^* + m_h^*}$ in a Coulomb potential (in a similar way to the hydrogen atom). The binding energy is then given by:

$$E_{XB,3D} = -\frac{R^*}{n^2} = \frac{\mu e^4}{2\hbar^2 \epsilon^2 n^2}$$

where n is the principal quantum number (n=1 corresponds to excitons ground state and n=2,3,4.. are the excited states), R^* is the Rydberg constant and ϵ is the dielectric constant. Because of the large dielectric constant in semiconductors, the excitons binding energy is smaller than E_{gap} and the Bohr radius ($a = \hbar\epsilon/e^2\mu$) is bigger than the lattice constant. In bulk GaAs, the exciton binding energy is ≈ -4.8 meV and $E_{gap} \approx 1.519\ eV$, it has a lattice constant of $\approx 0.565\ nm$ and Bohr radius of 11.6 nm. This long distance between the hole and the electron is what defines them as the so-called Wannier Mott excitons [25].

When using QWs whose thickness is smaller than the Bohr radius a strong confinement regime is achieved, meaning a modification in the exciton energy, quantization in the z-direction, an increment in the binding energy and a reduction in the Bohr radius. The exciton energy in a quantum well is given by:

$$E_X = E_{gap} + E_Q + E_{XB,2D} + \frac{\hbar^2 (K_X^2 + K_Y^2)}{2M} \tag{2.2}$$

where E_Q is a quantization energy for electrons and holes due to confinement. For a quantum well the energy is given by the text book solution of a particle in

a 1D potential well with finite barriers. The exciton binding energy ($E_{XB,2D} = R^*/(n-1/2)^2$) is 4 times the bulk value in the fundamental state and the Bohr radius is reduced by half.

Additionally, the probability of recombination in quantum wells is bigger than in bulk semiconductors. Because of the confinement, the oscillator strength is bigger in QWs and since excitons only couple with photons with the same momentum, in the case of quantum wells excitons can couple with a continuum of states because only the momentum in the QW plane has to match, facilitating radiative recombination. And, because the energy depends on the thickness and composition of the QW, it can be designed to bring the exciton energy in resonance with the cavity mode for polaritons formation.

Due to the large mass of the excitons compared to the cavity photons ($m_{ex} \approx 10^{4-5} m_{ph}$), exciton dispersion can be considered constant (Fig. 2.6) for the range of k-vectors of optically active excitons [26–28].

Radiative recombination of excitons only occurs under specific conditions. The first one is related to the wavefuncion symmetry and restrict the radiative excitons to the ones with the quantum number $l = 0$. The ground state excitons satisfy this rule [29].

The second condition is related to the spin. The total spin projection of an exciton is either $J = \pm 2, \pm 1$ or 0, while the spin of a photon is ± 1. Excitons with $J = \pm 2, 0$ can only couple to light after a spin flip process, making it less probable. Excitons with $J = \pm 1$ can directly couple to photons, allowing a radiative recombination.

Excitons that satisfy both conditions mentioned above can interact with light, and are known as "bright excitons".

For a deeper analysis of excitons physics, and the complete deduction of Equations 2.1 and 2.2 the reader is referred to: [26, 30, 31].

2.3 Semiconductor Microcavities

A Quantum Microcavity is a planar Fabry-Perot cavity formed by 2 high reflectivity mirrors separated by a layer called the cavity spacer, with some quantum wells sandwiched inside.

The optical length of the cavity used in this thesis is a half integer multiple

of the wavelength (λ) of the QW excitons and the mirrors are Distributed Bragg Reflectors (DBRs) that alternate $\lambda/4$ layers of low and high refractive index.

Depending on the number of layers, DBRs can reach a reflection of around 99.9 % of light for a given range of wavelengths, which is needed to enhance the life time of the photon inside the cavity. In transmission, light reflected from each interface destructively interferes, giving rise to a photonic band gap. The peak value of the DBRs reflectivity depends on the number of layers and the disparity of the refractive index between layers [32]. If the separation between the DBRs is a multiple of $\lambda/2$, stationary waves are created inside the cavity, then quantum wells are placed at the antinodes of the wave, so that photons confined in the cavity can couple with the excitons trapped in the wells. Figure 2.2 shows an example of a microcavity structure consisting of a $\lambda/2$ cavity between 2 $\lambda/4$ DBRs and its expected reflectivity, the cavity resonance is located at $\lambda = 774nm$ in the centre of the DBR's stop-band reflectivity.

As mentioned before, the first measurement of strong light-matter coupling, made in 1992, was done using a microcavity. It was made of an $L = \lambda$ GaAlAs layer with GaAs Quantum Wells (QWs) between 2 Distributed Bragg Reflectors (DBRs) made of 24 and 33 GaAlAs/GaAs layers each one. Using this kind of structure, Weisbuch et al. reported for the first time the observation of microcavity polaritons and Rabi splitting in microcavities of 2 to 5 Quantum Wells [1], beginning a new era for exciton-polariton research.

2.3.1 Microcavity Photons

Photons that travel in free space have a linear dispersion: $\hbar c|k|$, where k is the wave vector and c is the velocity of light in vacuum. When photons move in a material of a refractive index n the dispersion modifies as:

$$E_{ph}(k) = \frac{\hbar c}{n}\sqrt{k_x^2 + k_y^2 + k_z^2} \tag{2.3}$$

Inside a cavity, the light is reflected by the DBRs allowing only particular optical modes to resonate due to interference. The thickness of the spacer layer (L_c) determines the wavelength of the cavity modes:

$$\lambda_c = \frac{2n_{sl}L_c}{m}$$

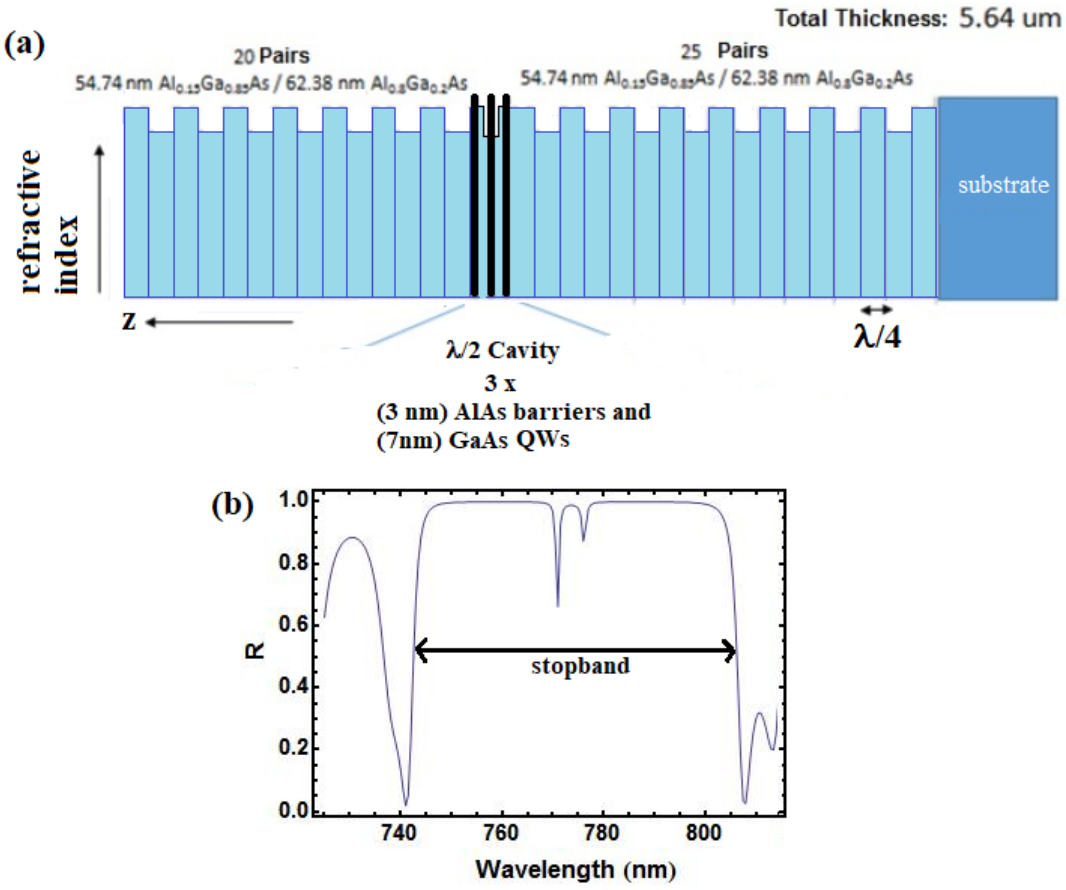

Figure 2.2: (a) Scheme of a microcavity structure consisting of a $\lambda/2$ cavity (with 3 GaAs QWs) in between 2 DBRs with 20 and 25 pairs of $\lambda/4$ $Al_{0.15}Ga_{0.85}As/Al_{0.8}Ga_{0.2}As$. (b)Simulated reflectivity spectrum of the microcavity structure. The two coupled-mode polariton dips appear in the centre of the DBR's stopband, around the cavity resonance of 774 nm.

Where m is the integer mode number and n_{sl} is the refractive index of the spacer layer.

The cavity mode is confined along the growth direction z, so photons can move freely in the x-y plane while in the z direction the wave vector is quantized ($k_z = m\pi/L_c$). We can define the complete k vector as $\vec{k} = k_x\vec{x} + k_y\vec{y} + k_z\vec{z}$ and from equation 2.3 the dispersion becomes:

$$E_{ph}(k) = \frac{\hbar c}{n_{GaAs}}\sqrt{(\frac{m\pi}{L_c})^2 + k_{||}^2} \tag{2.4}$$

Where $\vec{k_{||}} = k_x\vec{x} + k_y\vec{y}$ is the in-plane wave vector and n_{GaAs} is the refractive index of the spacer layer, made of GaAs for the microcavity used in this thesis (3.1.2). For small wavevectors the dispersion curve is parabolic (Figure 2.6), and can be rewritten using Taylor expansion, for the case where m=2:

$$E_{ph}(k_{||}) \approx \frac{\hbar c}{n_{GaAs}}\frac{2\pi}{L_c}[1 + \frac{1}{2}k_{||}^2(\frac{L_c}{2\pi})^2] \tag{2.5}$$

$$E_{ph}(k_{||}) \approx E_{c0} + \frac{\hbar c L_c k_{||}^2}{4\pi n_{GaAs}} \tag{2.6}$$

Where $E_{c0} = \frac{2\hbar\pi c}{L_c n_{GaAs}}$ is the photon energy at $k_{||} = 0$. The effective mass of the photon, deducted from the curvature of the parabolic dispersion is given by:

$$m_{ph} = \frac{hn_c}{cL_c} = \frac{hn_{GaAs}^2}{c\lambda_c}$$

of the order of 10^{-4} times the free electron mass.

The emission angle of the cavity photons is directly related to the inplane wavevector as:

$$k_{||} = \frac{2\pi sin\theta}{\lambda}$$

which allows to access the wavevectors by simply measuring the emission angle ($\theta = (\theta_x, \theta_y)$) from normal incidence and the wavelength (as done for sample characterisation in the following chapters). Figure 2.3 shows an example of a microcavity dispersion where the x axis is the k vector ($k_{||}$) equivalent to the emission angle (θ).

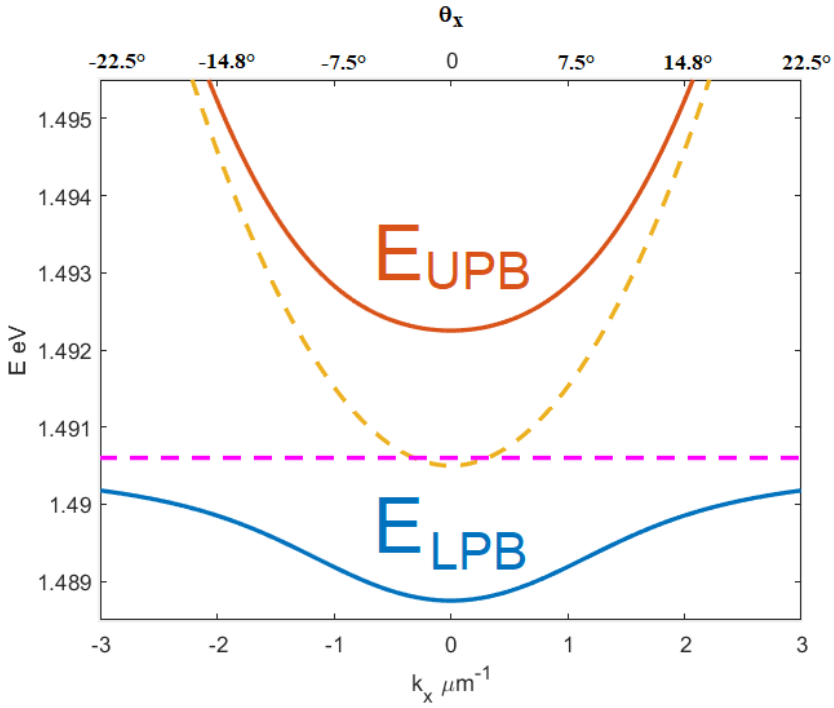

Figure 2.3: Example of a microcavity energy-momentum dispersion. Pink and yellow dotted lines correspond to the uncoupled exciton and cavity photon energy, respectively. The lower and upper polariton branches are shown in blue and red respectively. The x axis shows the correspondance between the emission angle (θ) and the in-plane wavevector (k_x).

2.3.2 Quality Factor and Finesse

An optical resonator, as a microcavity, is characterized by two values: the quality factor Q and the finesse. They are related to the time during which the energy is stored compared with the loss rate [33], in a microcavity the Q factor will describe the rate of optical energy loss per round trip [26].

The quality factor is defined as: [34]

$$Q = \frac{2\pi(stored\ energy)}{energy\ loss\ per\ cycle} = \frac{v_0}{\delta v} \tag{2.7}$$

where v_0 is the cavity resonance and δv is its spectral linewidth.

The finesse F is defined as a function of the free spectral range v_f as:

$$F = \frac{v_f}{v_0} Q \tag{2.8}$$

As a high Q factor indicates lower rates at which the energy stored in the microcavity dissipates, high quality factors are desirable and the evolution on microcavity fabrication techniques has showed an increment in the Q factors achieved, while in 1992 a high quality factor in semiconductor microcavities was considered to be between 100-300 [1], nowadays a high Q is considered$>$ 1000 [19] even reaching factors of 1000000 [35].

2.3.3 Fabrication

The fabrication of high quality microcavities became popular after 1979 when the first VCSEL was produced [36]. Nowadays two main techniques are used in the fabrication of semiconductor microcavities: Molecular Beam Epitaxy and Metal Organic Chemical Vapor Deposition.

Molecular Beam Epitaxy (MBE)

The Molecular Beam Epitaxy technique was developed in the 60s by John Arthur and Alfred Cho, who started with the homoepitaxial growth of GaAs and then migrated to heterojunctions of III-V Semiconductors [37]. The MBE technique consists in deposition of atomic layers on a heated substrate that is in an ultra-high vacuum (at a base pressure of less than $1x10^{-10}$ mbar). To make this process possible the constituent materials (Al, Ga, As, In etc.) are inside different effusion cells and in gaseous state. The cells are directed towards the substrate but blocked by shutters. When the shutters open, the materials, in form of molecular beams, flow to the substrate and are deposited at rates of the order of 1 monolayer per second.

Under normal growth conditions of III-V semiconductors, the composition and the epitaxial growth rate are proportional to the flux of the III components, which are controlled through the temperature of their source effusion cells [38]. The growth of a microcavity usually takes more than 24 hours, and continuous monitoring of the growth rates for each layer in the DBRs is required in order to achieve the right reflectivity (refractive index of each layer, thickness and composition need to be controlled). To measure the growth rates in real time for these specific structures some techniques have been developed as in-situ reflectivity measurements [39–41] and substrate temperature oscillations observed by infrared pyrometry [42].

Metal Organic Chemical Vapour Deposition (MOCVD)

In 1968 Manasevit and his co-workers in Rockwell Corporation invented and patented the Metal Organic Chemical Deposition to deposit GaAs by pyrolysis of a gas mixture of $[Et_3Ga]$ and $[AsH_3]$.A year later, III-V semiconductors compounds started to be produced by this technique [43].

As the MBE technique, MOCVD has been used to fabricate III-V semiconductors heterojunctions, quantum wells and microcavities of very high quality. However, these 2 techniques are very different, first of all, MOCVD does not work with the physical deposition of atomic layers in the substrate but through chemical reactions and secondly, it does not need a high vacuum environment just a gas phase at moderate pressures.

The growth by MOCVD is based on chemical reactions; ultra-pure gases are injected in the reactor, combined at high temperatures producing chemical reactions that allow the deposition of the materials on the substrate. The samples used by Weisbuch et al. in 1992 when they observed the strong-coupling were grown by MOCVD [1].

2.4 Polariton Waveguides

2.4.1 Basic principles behind optical waveguides

Since the invention of the laser in 1960, there has been a lot of interest in the development of technology for telecommunications and networking. Optical fibres are the most popular example of waveguides because they have played a central role on the revolution of optical communications. For polaritons, the interest of using waveguides arises from the possibility of creating complex optical circuits that could combine the advantages of photonics with the nonlinear effects present in polaritonic systems.

The simplest waveguide is formed by 2 different materials: the core and the cladding. The core is the central part of the waveguide and has a refractive index n_2 bigger than the refractive index of the cladding n_1 (Fig. 2.4). Light is guided by the phenomenon of Total Internal Reflection (TIR) which is understood by the Snell Law, which describes the refraction angle of a light ray that goes from

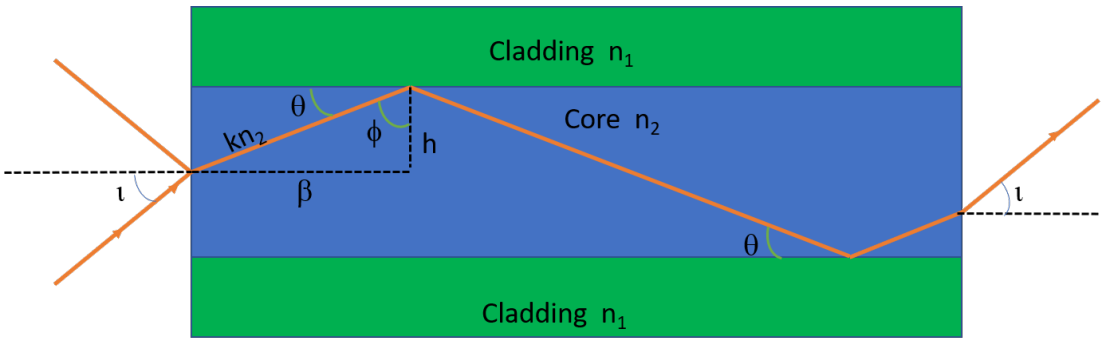

Figure 2.4: Simple waveguide structure, consisting of a core with refractive index n_2 and a cladding n_1, where $n_2 > n_1$. The scheme also shows the orthogonal components (h and β) of the ray travelling inside the waveguide.

one material to another of different refraction index:

$$n_1 sin(\phi_1) = n_2 sin(\phi_2) \tag{2.9}$$

The critical incidence angle needed to achieve total internal reflection in a material, can be obtained from Snell law by assuming $\theta_1 = 90$ °, which means that the light on the material with a refractive index n_2 is completely reflected.

$$\phi_c = sin^{-1}(n_1/n_2) \tag{2.10}$$

By definition, the wavevector $\vec{k}$ describes the direction of propagation of a ray of light, and in a medium with a refractive index n, it has a magnitude of kn. If we decompose the ray travelling inside the waveguide into its orthogonal components (h and β as showed in figure 2.4), and focus on the component parallel to the axis of the waveguide (β), we find that β must be bigger than kn_1:

$$sin(\phi) = \frac{\beta}{kn_2} \tag{2.11}$$

ϕ varies between ϕ_c and $\pi/2$, which means:

$$kn_2 sin(\phi_c) < \beta < kn_2 sin(\pi/2) \tag{2.12}$$

$$kn_1 < \beta < kn_2 \tag{2.13}$$

β is known as the propagation constant, and is the equivalent, inside the waveguide, to the wavenumber k in free space. Equation 2.12 shows that the propagation constant inside the waveguide always has a value between the wavenumbers of the core and the cladding [44]. This range also defines the light cone that contains all the rays that escape the waveguide. In addition, because the phase of any round trip of light on the waveguide must be a multiple of 2π, β can only take up discrete values, corresponding to different propagating modes [45].

2.4.2 Waveguide Photon Dispersion

In contrast with the microcavities where the photonic dispersion is parabolic, the fundamental photonic modes for a waveguide are approximately linear and parallel for the range of energies used in this work (between 1 and 2 meV, see figure 2.6 discussed in section 2.5), and have the form:

$$E_{ph}^{TE}(\beta) = \hbar v_g^c \beta + E_0 \tag{2.14}$$

$$E_{ph}^{TM}(\beta) = \hbar v_g^c \beta + E_0 + \Delta_{TE-TM} \tag{2.15}$$

For the Transverse-Electric (TE) and the Transverse-Magnetic (TM) modes. E_0 is the energy intersection with $\beta = 0$ (for the sample used in chapter 4 can be considered $E_0 = 0$, however instead of using absolute energies we considered the intersection of the photonic and the excitonic mode as the point of E=0), v_g^c is the group velocity of the light inside the system and Δ_{TE-TM} is the TE-TM separation [45].

2.4.3 Optical Losses

There are 3 fundamental causes of transmission losses in a waveguide: scattering, absorption and radiation. The total losses in a waveguide are defined as:

$$Loss = log[\frac{I_{out}}{I_{in}}] = \alpha \tag{2.16}$$

Where α is known as the loss coefficient, and as showed in Eq. 2.16, is a

direct comparison between the initial intensity entering the waveguide (I_{in}) and the one going out (I_{out}). As the losses increase with the waveguide length, the loss coefficient is usually expressed in decibels per unit length (dB/cm).

The most important losses in polariton waveguides are due to absorption. Scattering losses are neglected because their main cause are defects in the crystal, which are strongly reduced by growing the polariton waveguide by MBE. Radiative losses mean dissipation of energy into the cladding or the substrate, and they are small for well confined modes.

Absorption losses can occur by intra- or inter- band transitions. The absorption generated by intra-band transitions are negligible in this work, since all the experiments were carried out at low temperatures (4-12 K). Absorption due to inter-band transitions can be controlled by the operating wavelength. To reduce the losses the photon energy must be well below the absorption in the waveguide material (for GaAs, 1.519 eV at 4K) [45].

2.4.4 Polariton Waveguide Structures

In a polariton waveguide the photonic component is confined by total internal reflection (TIR). The waveguide structure is similar to the one described in section 2.4.1. Polariton waveguides are formed by a core and a cladding, of different refractive index to allow TIR. The core contains excitonic material in form of quantum wells. In our case, we used a polariton waveguide with 3 InGaAs QWs sandwiched by an AlGaAs cladding (see full description of the sample in section 3.1.1). Gratings were etched on the surface to couple the light in and out of the sample.

There are two ways of coupling light in a waveguide. The first one is to directly couple light into the core of the guide by using a laser or an optical fiber directed to the cleaved edge of the sample. However, because the experiments are carried out at low temperatures, the waveguide must be kept inside a cryostat, which makes this approach too complicated.

The second option is surface coupling through diffraction gratings. The gratings work by perturbing the photonic mode in its vicinity. It creates spatial harmonics at multiples of $\pm 2\pi/\triangle$, where $\triangle$ is the grating period. Light is coupled to the guide when one of these harmonics lies within the light cone, which can be adjusted by choosing the right grating period.

Waveguide structures present some advantages over microcavities. The most

relevant may be that they can afford, in principle, smaller losses than microcavities. Because waveguides operate at bigger wavenumbers polaritons can propagate longer distances, making them a good candidate for polariton optical circuits.

2.4.5 Fabrication

Just as microcavities (2.3.3), a waveguide core and cladding can be fabricated by MBE or MOCVD. The grating couplers are etched over the cladding by Electron Beam Lithography (EBL).

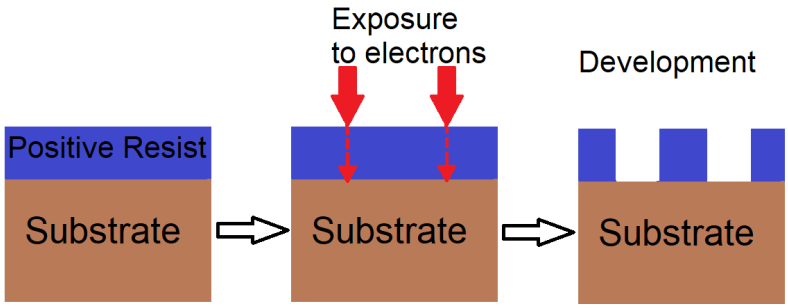

Figure 2.5: Outline of the EBL process using a positive-tone resist

EBL is a nanofabrication technique that allows the creation of 2 dimensional patterns with nanoscale resolution [46]. An arbitrary pattern can be created without a mask, with a focused electron beam that modifies the solubility of a resist material during a subsequent development step (2.5). It is also used for fabrication of complex microcavity structures as the microwire used in chapters 5 and 6.

Fabrication is usually easier than for microcavities. Because microcavities need the epitaxial growth of many layers, accumulated strain energy is a key factor to take in consideration, as it can generate dislocations that strongly modify the potential landscape. In addition, for waveguides, the photonic mode will be in resonance with the exciton at some wavenumber independently of the epitaxial growth, while for microcavities this is fixed by the structure. Finally, to control the photonic mode, in microcavities the fabrication of structures like microwires (2.5.4) require etching through, at least, the top DBR which is some micrometers thick, while in waveguides it is enough to etch a few nanometers into the core and cladding.

2.5 Strong Coupling

If we consider a quantum well embedded in a waveguide or in a microcavity, a photon moving inside the system close to resonance to the exciton transition could be absorbed to form an exciton and then re-emitted with the same momentum. If the coupling between the photon and the exciton is strong enough, the system gets new eigenmodes called polaritons.

Polaritons are the real propagation modes of the electromagnetic field inside a dielectric crystal or a semiconductor. However, one of the reasons why they are so difficult to detect in bulk semiconductors, is that in order for polaritons to be detected from outside, photons that are coupled to free space excitons need to reach the surface of the crystal (to be de-coupled and emitted), and since they are subject to scattering by defects, impurities and other excitons, the radiative rate becomes small [47]. In addition, the lower polariton branch (LPB) does not directly couple to light (because it is outside the optical cone) and phonon scattering is usually required [30]. To enhance the radiative recombination rate, the symmetry of the system needs to be broken, for example in the 2D confinement of a QW, the momentum conservation only apply in the QW plane and excitons can couple to a continuum of states. If the quantum well is embedded in a microcavity or a waveguide, and the photon and exciton are in resonance, strong coupling may be observed.

The coupling between the photon and the exciton modes can be understood in analogy to two coupled springs, each mode corresponds to a spring with an independent frequency w_1 and w_2, when the coupling is strong enough both oscillate at a modified frequency w_3. A polariton system can then be described as two damped coupled oscillators with the Hamiltonian:

$$\begin{bmatrix} E_x(k) + i\gamma_x & g \\ g & E_{ph}(k) + i\gamma_{ph} \end{bmatrix} \tag{2.17}$$

Where instead of using w_1 and w_2 as it would be in the springs system, E_x and E_{ph} are used to describe the energies of the uncoupled excitonic and photonic mode, γ_x and γ_{ph} are their linewidths and g is the coupling strength [48]. The polariton dispersion relations are given by the eigenvalues of Eq. 2.17 known as the Lower Polariton Branch (LPB) and the Upper Polariton Branch (UPB).

$$(E_{LPB,UPB}(k) - E_x(k) + i\gamma_x)(E_{LPB,UPB}(k) - E_{ph}(k) + i\gamma_{ph}) = g^2 \tag{2.18}$$

$$E_{LPB,UPB}(k) = \frac{E_x(k) + E_{ph}(k) - \mathrm{i}(\gamma_x + \gamma_{ph})}{2} \pm \frac{\sqrt{(E_x(k) - E_{ph}(k) - \mathrm{i}(\gamma_x - \gamma_{ph}))^2 + 4g^2}}{2} \tag{2.19}$$

An example of polariton dispersion for a microcavity and a waveguide system are shown in Figure 2.6. Note that the change in the shape of the dispersion for each system comes directly from the different photonic dispersion, which is parabolic for a microcavity and linear for a waveguide (see section 2.3.1 and 2.4.2 for details).

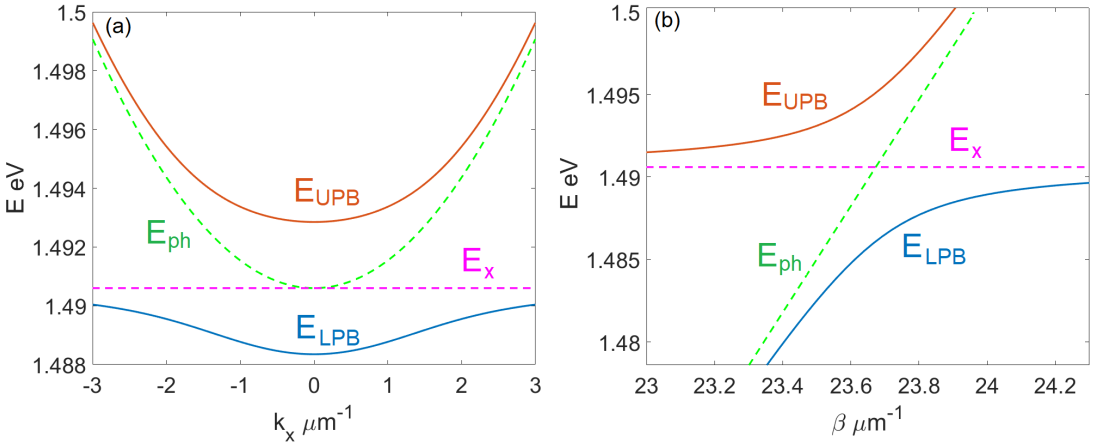

Figure 2.6: (a) Polariton dispersion in a microcavity (b) Polariton dispersion in a waveguide. Uncopled exciton (E_x) and photon (E_{ph}) dispersions are plotted with dashed lines, Lower and Upper polariton branches (E_{UPB} and E_{LPB}) are showed with solid lines.

At zero detuning ($E_x = E_{ph} = E$) we get:

$$E_{LPB} = E - \mathrm{i}\frac{(\gamma_x + \gamma_{ph})}{2} - \frac{\sqrt{4g^2 - (\gamma_x - \gamma_{ph})^2}}{2} \tag{2.20}$$

$$E_{UPB} = E - \mathrm{i}\frac{(\gamma_x + \gamma_{ph})}{2} + \frac{\sqrt{4g^2 - (\gamma_x - \gamma_{ph})^2}}{2} \tag{2.21}$$

The energy difference between the two polariton modes ($E_{UPB} - E_{LPB}$) at resonance is known as the vacuum Rabi splitting:

$$\hbar\Omega = \sqrt{4g^2 - (\gamma_x - \gamma_{ph})^2} \tag{2.22}$$

Which gives the condition for strong coupling: $2g > |\gamma_x - \gamma_{ph}|$, because the Rabi splitting must be real to observe anti-crossing. It means that the exciton and the photon decay rates have to be low enough that the energy can be exchanged between the two modes more than once before decaying. If the Rabi splitting is imaginary (i.e. weak coupling), the coupling modifies the polariton linewidth but there is not an energy splitting and the system is described in terms of weakly interacting photons and excitons.

The Hopfield coefficients [10] describe the contribution of the bare exciton and photon to the new coupled modes and satisfy $|C_x(k)|^2 + |C_{ph}(k)|^2 = 1$:

$$|C_x(k)|^2 = \frac{1}{2}(1 + \frac{\Delta}{\sqrt{\Delta^2 + 4g^2}}) \tag{2.23}$$

$$|C_{ph}(k)|^2 = 1 - |C_x(k)|^2 = \frac{1}{2}(1 - \frac{\Delta}{\sqrt{\Delta^2 + 4g^2}}) \tag{2.24}$$

Polariton characteristics vary depending on the detuning ($\Delta = E_{ph} - E_x$). For negative detuning, $C_{ph} > C_x$, the photonic component of polaritons is bigger and their group velocity too. On the other hand, for positive detuning $C_{ph} < C_x$, polaritons are excitonic-like, meaning smaller velocities but stronger inter-particle interactions.

2.5.1 The spin of polaritons

Polaritons are composed by photons and excitons, both bosons, and as their components, they also have an integer spin. However, excitons are composed by fermions and can be considered composite bosons only in a low-density regime.

At high density, excitons start to behave as fermions because of two effects consequence of the Pauli exclusion principle: the phase space filling effect and exchange effects. The phase space filling refers to the fact that at high density there is a limit where no more excitons can be created because electron and hole states are filled. Energy exchange effects refers to the usual fermion phenomena where carriers with the same spin gain energy by avoiding each other. The limiting density for excitons to be considered bosons is called the saturation density, and is given by: $n_{sat} = \frac{0.117}{\pi a_B^2}$ where a_B is the Bohr radious [49]. Higher exciton densities also mean loss of strong coupling.

Polaritons spin structure is determined by the excitons. The spin of excitons

is the sum of its fermionic components, the hole and the electron. Because the lowest conduction band in a zinc-blende crystal, such as GaAs, is of s-symmetry, the electron has a total angular momentum of $\pm 1/2$. Holes are localized in a p-type valence band and can have a total angular momentum of $\pm 1/2$ or $\pm 3/2$, they are called light and heavy holes respectively. The confinement in a quantum well structure moves the energy levels of the light and heavy holes, making the heavy holes level the closest to the bottom of the well (figure 2.1). Consequently, heavy holes and electrons form the ground state exciton and give it a total spin of 0, ± 1 or ± 2. As mentioned in 2.2, bright excitons have a spin of ± 1, and because they can interact with light, they are the excitonic component of polaritons. As an exciton can only couple with a photon of the same spin, the resulting polariton is a two-level spin system, like the electron but with integer spins, hence the term pseudospin [50]. In the pseudospin formalism, the state $|-1\rangle$ corresponds to spin down $|\downarrow\rangle$ and $|+1\rangle$ to spin up $|\uparrow\rangle$.

As mentioned before, only photons and excitons with the same spin can couple, because of angular momentum conservation. In microcavities, at $k = 0$ the system is symmetric about the growth axis so the photons of an incident circularly polarized beam $\sigma + (\sigma-)$ have an angular momentum of +1(-1). Photons and excitons with the same spin will couple, creating $|\uparrow\rangle$ ($|\downarrow\rangle$) polaritons. When light goes out of the cavity, from the destroyed polariton, the photons preserve its circular polarization. Linear polarized light excites a linear combination of +1 and -1 exciton states, so that the total spin projection in the growth direction is zero in this case. This means that the spin orientation of a polariton population can be controlled by using a polarized optical excitation.

2.5.2 TE-TM Splitting

Microcavity exciton polaritons exhibit a longitudinal-transverse energy splitting (TE-TM splitting), between polaritons with dipole moments perpendicular and parallel to the in-plane wave-vector [51].

Whilst, in waveguides the TM mode can be neglected because only the transversal electric (TE) modes strongly couple to the QWs excitons and the TE-TM detuning is large enough [45]. For microcavities, the TE-TM splitting plays an important role in polaritons spin dynamics(6).

The main spin relaxation mechanism for quantum-well excitons involves the spin-flip exchange interaction of electrons and holes [52]. An energy splitting between excitons with a dipole moment perpendicular (TE) and parallel (TM)

to the wave-vector results from the long-range electron-hole interactions. For polaritons, this mechanism of spin relaxation is intensified by an additional TE-TM splitting coming from the photonic modes in the cavity. The TE-TM splitting, for the bare excitonic and photonic modes in a microcavity, grows quadratically with k and is zero at k=0. The TE-TM splitting in the LPB is showed in figure 2.7.

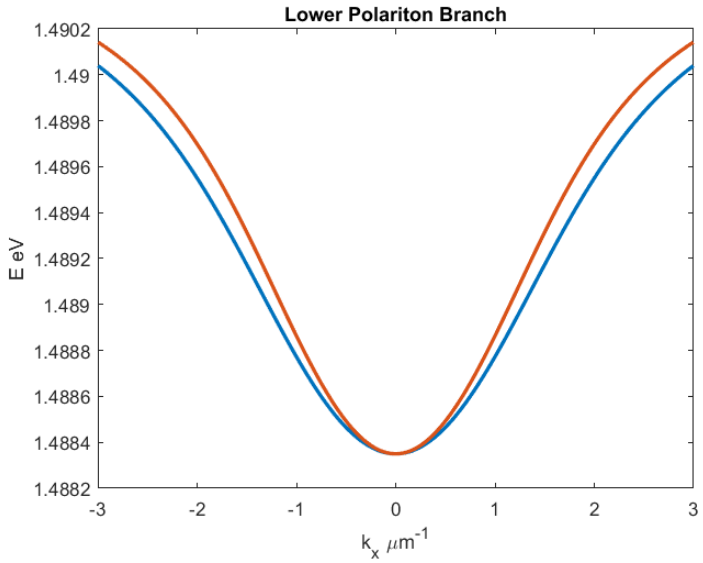

Figure 2.7: Microcavity lower TE branch (blue line) and the lower TM branch (red line).

A fundamental consequence of the TE-TM splitting is the appearance of a momentum dependent effective magnetic field in the plane of the QWs that produces rotation of the polariton polarization. The global expression for the strength of the TE-TM effective magnetic field is given by:

$$H_{TE-TM}(k) = \frac{(E^{TE}_{LPB}(k) - E^{TM}_{LPB}(k))}{\mu_B g_s} \begin{bmatrix} cos(2\phi) \\ sin(2\phi) \end{bmatrix} \tag{2.25}$$

Where ϕ is the polar angle in the reciprocal space (figure 2.8), μ_B is the Bohr magneton and g_s is the effective polariton g factor [17,50]. Spin polarized vortices [53] and solitons [54] are some consequences of this effective magnetic field. The influence of the TE-TM effective magnetic field in the polariton polarization will be discussed in detail in Chapter 6.

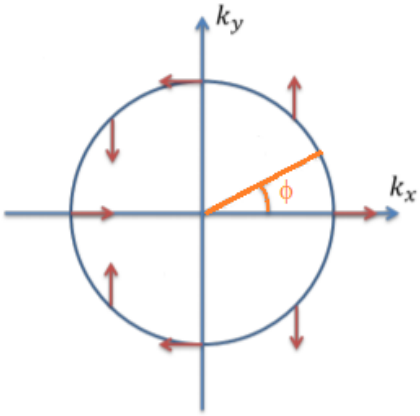

Figure 2.8: The red arrows show the distribution on an elastic circle in k-space of the effective magnetic field induced by TE-TM splitting.

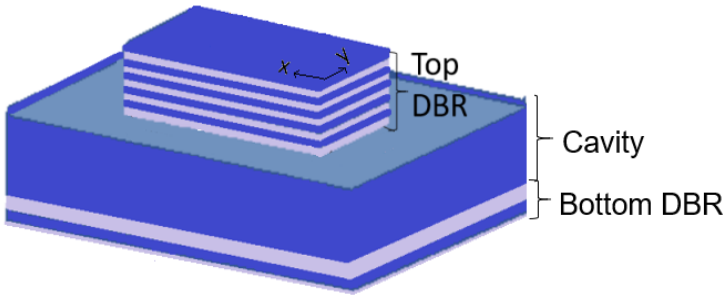

Figure 2.9: Scheme of a microwire showing x and y directions for reference

Microwires polarization splitting

Microcavity wires or microwires (MCW), are the 1D adaptation of a microcavity(2.5.4). To achieve the characteristic vertical confinement of a MCW, first a regular planar microcavity is grown by MBE or MOCVD and then the top DBR is partially etched using electron-beam lithography (fig 2.9).

In microwires, a polarization splitting occurs between the modes polarized along and across the wire. It was observed that this splitting increases as the width of the wire is reduced [55]. The modes can be separated into TE and TM modes. The TE modes have an electric field in the x direction and a magnetic field in the y direction and vice versa for the TM modes (fig 2.9).

Because of the boundary conditions in the microwire, TE modes, whose electric field is perpendicular to the interface, penetrate less into the vacuum region, are less confined than the TM modes. This confinement results in an energy TE-TM splitting, where the TM modes have the higher energy.

2.5.3 Group Velocity Dispersion

The effective mass and propagation velocity of a group of particles can be extracted from the energy-momentum dispersion. For polaritons it will depend on the system used, as the photon dispersion is different in microcavities and waveguides. In general, the velocity is proportional to the first derivative of the dispersion, and is expressed as a function of k_x for the microcavities and of β for waveguides:

$$v(k_x) = \frac{1}{\hbar}\frac{dE}{dk_x} \tag{2.26}$$

$$v_g(\beta) = \frac{1}{\hbar}\frac{dE}{d\beta} \tag{2.27}$$

From equation 2.20 we obtain a velocity for the polaritons in the LPB given by:

$$\frac{|C_{ph}|^2}{\hbar}\frac{dE_{ph}}{dk_x} \tag{2.28}$$

Where k_x is substituted for β in waveguides systems (as defined before in section 2.4.1) and C_{ph} is the photonic Hopfield coefficient. For waveguides the resulting group velocity dispersion (GVD) is obtained by the derivative of equation 2.14:

$$v_g(\beta) = |C_{ph}|^2 v_g^c \tag{2.29}$$

The velocity in microcavities is obtained from equation 2.5:

$$v(k_{||}) = |C_{ph}|^2 \frac{cL_c k_{||}}{2\pi n_{GaAs}} \tag{2.30}$$

As it was shown before in section 2.3.1 and 2.2, for photons and excitons respectively, the effective mass of a particle is given by the curvature of the dispersion by:

$$m^* = \frac{\hbar^2}{\frac{d^2E(k_x)}{dk_x^2}} \tag{2.31}$$

Which is also applicable for polaritons in any structure. Figure 2.10 shows how the sign of the effective mass changes for different wavevectors in microcavities, which is a crucial factor for solitons formation and Cherenkov radiation, as it will be explained in section 2.11 and chapter 5.

In a similar way, the variation of group velocity with frequency is quantified in optical systems, such as waveguides, by the group velocity dispersion (GVD) parameter. For polaritons in the LPB the GVD parameter is:

$$\beta_2 = \frac{d^2\beta}{d\omega^2} = \frac{d}{d\omega}\frac{1}{v_g(\beta)} = -\frac{\hbar^3\Omega^2}{2v_g^c\delta^3} \tag{2.32}$$

Where δ is the difference between the LPB and the exciton energy, $\delta = E_x - E_{LPB}$. The variation of group velocity in waveguides and optical fibers is relevant when considering the output pulse chirp, as spectral components of the transmitted pulse move with different group velocities they will arrive at different times to the output, producing a chirp in the pulse. By convention, regions where the GVD parameter is positive are referred as with normal dispersion, in this regime high frequency components of an optical pulse travel slower than the lower frequency components. The opposite occurs in the anomalous dispersion regions, where the GVD parameter is negative [56].

In microcavities, in accordance with the waveguide nomenclature, normal dispersion corresponds to the regions with a negative effective mass while anomalous dispersion is referred to a positive effective mass. The boundary between the two regions, known as the zero GVD point, corresponds to the inflection point in a microcavity dispersion relation.

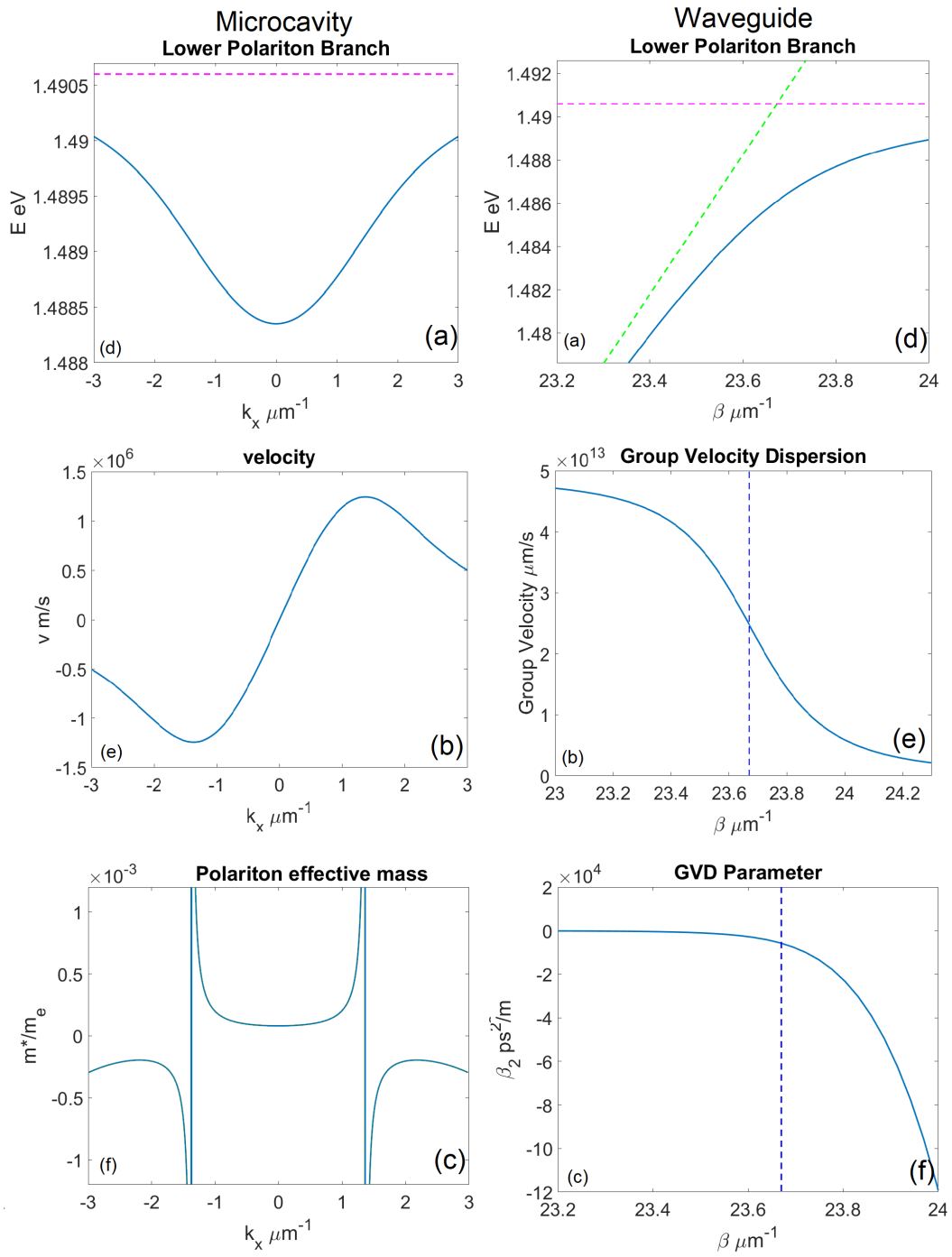

Figure 2.10: Microcavitys (a) LPB dispersion ($E(k_x)$) (b) Polariton velocity ($(1/\hbar)(dE/dk_x)$) and (c) Polariton effective mass ($(1/\hbar^2)(d^2E/dk_x)$). Waveguides (d) LPB dispersion (e) Group velocity dispersion ($(1/\hbar)(dE/d\beta)$) and (f) Group velocity dispersion parameter ($d^2\beta/d\omega^2$).

2.5.4 Multi-mode Microwires

The sample used for the experiments in Chapters 5 and 6 is a microwire, which can be described as a modified microcavity to allow 1D confinement. Polariton confinement can be obtained by etching a 2D planar microcavity. Etching through the quantum wells [55, 57] confines both the photonic and excitonic modes, but it has been proved that for polariton confinement, it is enough to confine the photonic modes by etching the top DBR of the microcavity [58].

Energy dispersion is modified by quantization, resulting in multiple polariton modes as shown in fig 2.11. One of the main consequences of this configuration is the creation of more scattering paths for the optical parametric oscillator, as there are new modes of the lower polariton branch and scattering can happen between those modes (see 2.8).

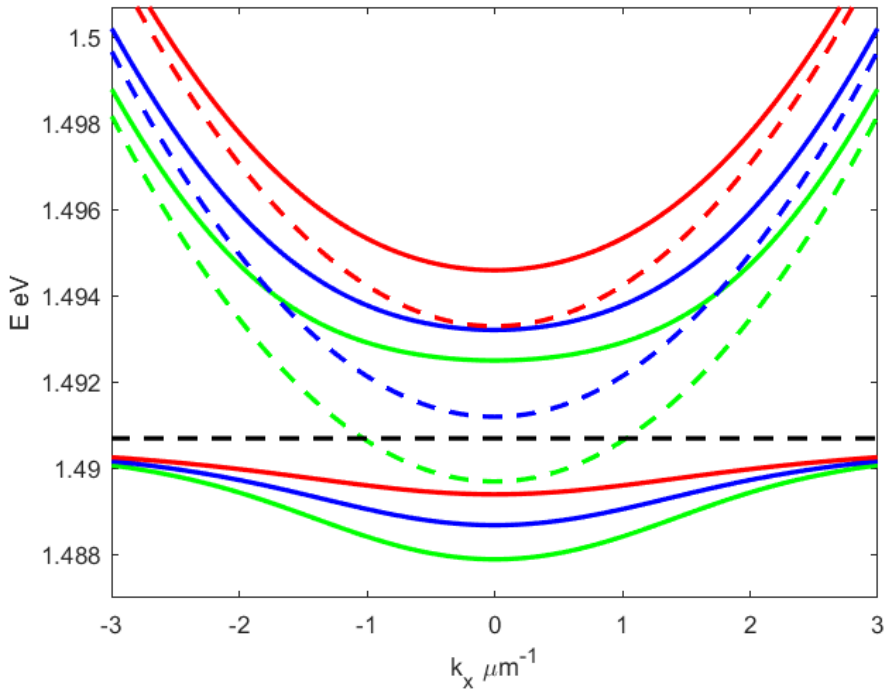

Figure 2.11: Energy-momentum dispersion of a microwire, showing several polariton modes (solid lines) resulting from quantization. The black dashed line shows the uncoupled exciton dispersion. The red, blue and green dashed lines show the uncoupled cavity modes

2.6 Exciton-Polaritons Research Trends

Since the discovery of microcavity exciton-polaritons in 1992 [1], there has been a giant amount of significant research in the field. A quick search with Scopus shows that around 1500 journal articles have been published in the last 26 years and that the top 3 countries where this research has been carried out, are Russia, UK and USA.

Chronologically, the first years after Weisbuch paper were dedicated to the theoretical understanding of microcavity polaritons and their intrinsic properties such as the vacuum-Rabi splitting [59, 60], followed by the realization of the bottleneck effect [61] and in 2000 the observation of polariton parametric amplification [18].

After the realization of polariton parametric scattering, the exciton-polariton research has been focused on non-linear optical phenomena [60]. Because of its relation with the results presented in this thesis, the following sections are dedicated to review many of these non-linear phenomena, including superfluidity (2.10), condensation (2.9) and soliton formation (2.11).

2.7 Polariton-Polariton interaction

One of the most important characteristics of polaritons is their strong interaction. Interaction between particles results in non linear behaviour. In the case of polaritons, its nonlinear properties come from its excitonic component, as photons do not interact.

Exciton-exciton scattering occurs due to Coulomb interactions. Excitons with the same spin repel each other, while interaction of opposite spins is considered to be much smaller, making the dominant exciton interaction repulsive [62]. Polaritonic interactions behave in a similar way. Polaritons with the same spin strongly repel and polaritons with opposite spin can weakly attract each other [63, 64], meaning a dominant repulsive inter-particle interaction.

Nonlinear effects arising from the excitonic Coulomb interactions in polariton systems include: parametric luminescence [65], parametric oscilations (2.8), a broadening of the excitons linewidth and of the polaritons linewidth, and a blueshift of the excitons resonance yielding to a polaritons resonance blueshift [65, 66].

Additionally, because of their bosonic nature (2.5.1), polaritons can experience bosonic stimulation, which means that the transition to a final state is stimulated if it is already occupied by other bosons [67,68]. Bosonic stimulation, is the underlying process of gain in lasers, where the macroscopic occupation of photons in the lasing mode stimulates the emission of more photons into it. The first experimental demonstration of bosonic stimulation with polaritons was the optical parametric amplifier discussed in the following section 2.8.

Apart from the polariton-polariton interactions, polaritons can also interact with the excitonic reservoir [64, 69]. Condensation through relaxation from the excitonic reservoir to the polariton ground state through phonon emission has been achieved in CdTe, GaAs, ZnO and GaN microcavities [67, 70–72]. Other indirect polariton interactions are: the Van-der Waals interaction, interaction via dark excitons and via biexciton state. The main consequence of the indirect interactions, as in any second order perturbation process, is the redshift of the polariton ground state [63, 64].

2.8 Polariton Parametric Scattering

A parametric process is defined as one where there is not transfer of energy and momentum between light and matter, so that the final and initial quantum states of the matter are identical, meaning that there is a conservation of energy and momentum inside the physical system [73].

Polarization as a response of an applied electric field E can be described by a Taylor series expansion as:

$$P(E) = \epsilon_0(\chi^{(1)}E + \chi^{(2)}E^2 + \chi^{(3)}E^3 +) \tag{2.33}$$

where

$$E = E_1 e^{-i\omega_1 t} + E_2 e^{-i\omega_2 t} + E_3 e^{-i\omega_3 t} + \cdots \tag{2.34}$$

And $\chi^{(n)}$ is the nth order susceptibility, ϵ_0 is the permittivity of free-space. The term nonlinear optics comes from this nonlinear response of the polarization of certain media to the electric field of light. Polariton parametric scattering is a four-photon process, described in the lowest order by $\chi^{(3)}$. When two pump photons convert into a signal and an idler with conservation of momentum and energy through $2k_p \rightarrow k_s + k_i$ and $2E_p \rightarrow E_s + E_i$, parametric scattering occurs.

The discovery of microcavity polaritons parametric scattering was a major

advance in polariton physics [68,74], because of its relation with several nonlinear phenomena such as condensation [4, 75], solitons formation [19, 76] and coherent control of polaritons [77].

A polariton optical parametric oscillator (OPO) is possible, thanks to the shape of the LPB in a microcavity, when exciting resonantly with a CW laser at momentum k_p [78]. If the pump intensity is high enough, polaritons strongly interact with each other, and the repulsive interactions make polaritons scatter. In this process two identical pump polaritons will scatter into the idler and the signal. The signal state will correspond to the bottom of the LPB ($k_s = 0$), then the idler will have twice the momentum of the pump ($2k_p = k_I$) (see Fig 2.12). Contrary to what we may expect, stimulation occurs at a wide range of pump angles from 10°to 24°. As shown in [79], the occurrence of $k_s = 0$ for different excitation energies and angles can be explained by a nonlinear treatment of the system, and energy-momentum conservation is observed when the signal and idler are renormalized with respect to the LPB.

OPO in microcavity systems was experimentally demonstrated by Stevenson et al [74], Tartakovskii et al [80] and Baumberg et al [81]. In addition, a second laser (the probe) can be used to stimulate the population of a selected signal state, in a configuration known as optical parametric amplification (OPA), which was experimentally achieved in 2000 by Savvidis et al. [18].

The work of Savvidis was the first experimental demonstration of the bosonic nature of polaritons interactions. It uses the effect of bosonic stimulation to show significant gain in a parametric scattering process. In the experiment, a probe laser at k=0 triggers scattering processes of the pump polaritons to the bottom of the LPB, with a gain of two orders of magnitude in the emission of the $k = 0$ state. Savvidis experimental results were theoretically modelled shortly after, using a quantum treatment of polariton-polariton interaction [82].

Additionally, the OPA experiment showed that a relatively large number of polaritons can be present at the bottom of the polariton LPB despite their short lifetime, giving a possibility for polariton condensates.

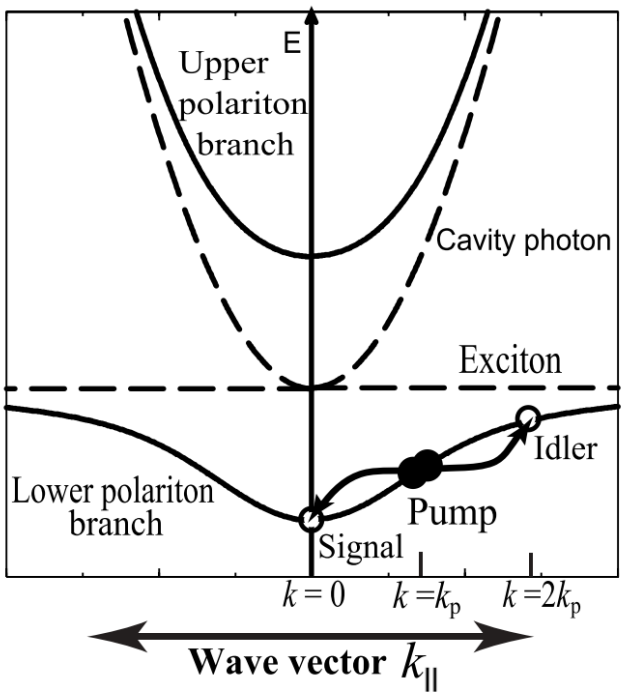

Figure 2.12: Schematic diagram of a microcavity OPO. The LPB is excited resonantly with a pump beam at (k_p) producing a high density of polariton population, polaritons then scatter off each other to the idler ($k_i = 2k_p$) and the signal ($k_s = 0$) states. OPA configuration is the same as in the picture but with a second laser (probe) at the same place as the signal, stimulating the population at the bottom of the LPB. Source: [83]

2.9 Polariton Condensate

The idea of achieving a Bose-Einstein condensate (BEC) made of exciton-polaritons appeared very attractive to the scientific community after 1996 when the first proposal of BECs made of exciton polaritons at high temperatures was published [84] and the applications related to polariton lasers were pointed out.

The Bose-Einstein condensation is the phase transition where excited states are saturated and the ground state becomes macroscopically occupied [85]. An

ideal Bose gas will obey a Bose-Einstein distribution:

$$n_i = \frac{1}{exp(\frac{E_i - \mu}{k_B T}) - 1} \tag{2.35}$$

Where μ is the chemical potential, T is the temperature, and $N = \sum_i n_i$ is the total number of particles. When $\mu \to 0$, the ground state occupancy becomes large without limit, so if N is bigger than N_{cr} defined as the total number of particles in the excited states; $N_{cr} = N_E(T, \mu = 0)$, then the additional bosons will massively occupy the ground state, as proposed by Einstein [86]. Additionally, as it was shown in 1995, it is necessary to take into account interactions between particles and the energy cost of exchange terms to demonstrate that condensation will occur in only one single ground state [87].

The modern definition of BEC was given at the beginning of this millennium [88, 89] and it is related to the appearance of long-range phase coherence in the condensate [90]. That means that there would be a phase relation at points separated by distances much larger than the thermal de Broglie wavelength $\lambda_B = \sqrt{\frac{2\pi\hbar^2}{mk_BT}}$. Experimentally, macroscopic length coherence means a high spatial correlation over distances longer than de Broglie wavelength and comparable to the sample size.

Furthermore, Bose-Einstein distribution can only be used when the distance between particles is $\approx \lambda_B$ so the gas becomes degenerate and this would happen easier for lower mass and temperature.

The first unambiguous proof of a BEC was made with an atomic vapour of rubidium in 1995 [91], a year and a half later the long range coherence of this system was demonstrated [92]. At first sight, atomic condensation may look like a simple task: reduce the temperature of an atomic cloud until reaching the degeneracy condition. However, the main problem is that a transition into a solid state could occur before BEC. This is the main reason why Rubidium, an alkali atom was used: it would allow an evaporative cooling [93].

Proposals of BEC in solid state systems [94, 95] were made long before the atomic BEC in 1995. The idea of condensation in a solid can be explained through the Bloch theory [96], that says that a free carrier moving through a crystal lattice can be considered as a plane wave modulated by a periodic function whose period is given by the lattice. The fact that the wavevector is preserved over time means that carriers move in the medium without scattering, forming a quantum gas. Nonetheless, this picture is destroyed by any perturbation in the periodicity as it can make carriers to scatter. The periodicity of the crystals is what leads

to the band structures previously introduced in section 2.2. Some attempts of producing a Bose-Einstein condensate in solids using excitons were made at the end of the 60s [97]. However, reaching BEC with excitons has 2 main difficulties: the saturation density which sets a limit for excitons population to be considered bosons (section 2.5.1) and exciton-exciton interactions (section 2.7), which are not allowed in an ideal Bose gas. After years of research without reaching an excitonic BEC fully accepted, it resulted easier to change into the search of an exciton-polariton Bose Einstein Condensate.

Because of the bosonic nature of polaritons (2.5.1), in principle they are a good candidate for BEC. The key parameter compared with excitons is their low mass (4 or 5 orders of magnitude smaller) which is a big advantage for BECs, and makes possible to have a condensate at higher temperatures than for atomic systems. On the other hand, their main disadvantage is their very short lifetime (several picoseconds), fortunately, as showed in the previous section (2.8), polariton scattering rates can be fast enough to bring polaritons into their ground state.

Polariton condensation in microcavities can be achieved in the two following ways: by non-resonant pumping at the reflection minimum of the stop band at k=0 [4, 98] or by quasi-resonant excitation at a large angle [75, 99] (Fig 2.13 a). Both methods will introduce a polariton population losing the original coherence of the laser, as the objective is to measure the spontaneous coherence of polaritons [100].

The first Bose-Einstein condensate in a semiconductor system fully evidenced (with spontaneous symmetry breaking and long-range order) was done in 2006, within a microcavity of CdTe/CdMgTe. Here the control parameter used was the excitation power and thus the injected polariton density. Direct measurements of the occupancy of polaritons according to their energy were made, showing that at very low excitation power, occupancy is not thermalized. Near threshold, the occupancy shows a Maxwell-Boltzmann distribution indicating a polariton gas and above threshold, saturation of the excited states and condensation into the ground state is observed. Moreover, the most important feature for a BEC demonstration was provided: direct evidence of coherence across the entire condensate [4].

It is important to remark that polariton condensates are 2 dimensional. In a 2D system BEC is not possible because conventional long range order can not be established unless there is weak spatial confinement. In an ideal 2D system only Berezinskii-Kosterlitz- Thouless (BKT) phase transition with finite coherence length can be obtained (see [101] and [100] for a detailed explanation about these possibilities and its relation with polariton systems).

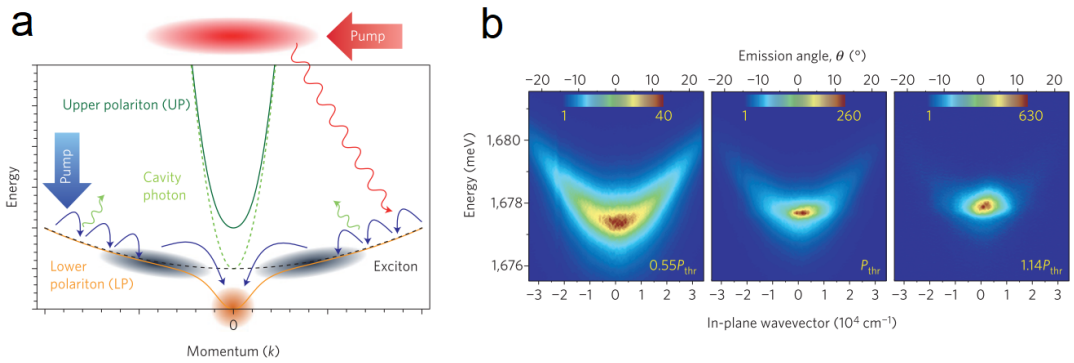

Figure 2.13: Exciton-polariton condensation. (a) Schematic diagram of the polariton dispersion and the condensation process. The resonant pumping scheme (large blue arrow) and the non-resonant pumping scheme (large red arrow, pumped at a higher energy) are shown. The pump laser initially excites high-energy excitons, which then cool via phonon emission towards the bottleneck region (black clouds). Excitons in the bottleneck region then scatter into the condensate (orange cloud) via stimulated cooling (Source: [100]). (b) Experimental dispersion images of polariton condensate formation. Below the threshold, polaritons are broadly distributed in momentum and energy. Above threshold, the polaritons condense in the k=0 lowest energy state. [4]

Despite the fact that polariton condensates can achieve long range spatial coherence (off-diagonal long-range order), the non-equilibrium nature of the system has raised the discussion of whether it should be called Bose-Einstein condensation at all. The non-equilibrium character of polariton BECs is manifested by the observation of multimode emission from polariton condensates in the case of single mode laser pumping, meaning that condensation occurs into several polariton levels. The losses are balanced by the gain for many modes with different energies, which results in simultaneous condensation [102].

Although, the system presents narrowing of the linewidth, threshold behaviour and macroscopic occupancy of the ground state, these characteristics are shared with a polariton laser. The polariton laser is a type of laser where population inversion is not necessary to form a coherent polariton population [84, 103]. The difference between a Bose-Einstein condensate and a polariton laser would be that in the laser the polariton population is not thermalized. A new term: Polariton Condensate is used to encompass both, the polariton laser and the BEC [100].

2.10 Superfluidity

One of the most significant phenomena linked to Bose-Einstein condensation is superfluidity. The first observation of superfluidity was made in liquid He-4 in 1938 by Kapitza in Moscow and Allen and Misener in Cambridge [104, 105]. They observed how the liquid Helium below 2.17 K can flow without apparent friction, one of the most distinguished manifestations of superfluidity. As pointed out by Fritz London [106], this phenomenon is deeply related to Bose-Einstein condensation. London noted that a non-interacting gas with the mass and density of He-4 should experience Bose-Einstein condensation at 3.3 K and suggested that this was what was observed in He-4 at 2.17 K. Based on London idea, Laszlo Tisza suggested that Helium superfluidity could be understood in terms of a two fluid model [107] in which one fluid is the condensate (those atoms that occupy the same one-particle state) that flows without friction and the other is the normal liquid [108].

In 1941 Lev Landau published the quantitative description of superfluidity. In his work, Landau introduced for the first time, the concept of quasiparticle as an excitation of the system from the ground state with an energy and momentum such that (at least at low temperature) the total energy, momentum, etc., of the system can be regarded as the sum of that carried by the quasi-particles. Landau identified 2 types of quasiparticles of a Bose fluid: phonons and rotons, the first ones have an energy of $\epsilon = cp$ where p is the momentum and c the speed of sound, and the second ones correspond to quantized rotational motion with an energy spectrum of $\epsilon(p) = \frac{(p-p_0)^2}{2m}$(this second energy was given by Feyman and Cohen in 1956 [109], and it is slightly different from original Landau's equation [110]).

Nowadays, superfluidity is understood in terms of macroscopic occupancy of a single-particle state, or a generalized BEC, which means that a superfluid phase is achieved when from a complete orthonormal basis of single-particle states, one and only one of these states is macroscopically occupied, while the other states can only have 1 or less particles. Then, if the macroscopically occupied state is defined as $\chi_0(r,t) = |\chi_0(r,t)|e^{i\phi(r,t)}$, the superfluid velocity is given by: $\frac{\hbar}{m} \bigtriangledown \phi(r,t)$. From this velocity expression it is easy to note two of the main characteristics of the superfluid component of a Bose liquid: it has zero entropy and flows irrotationally.

After the observation of Bose-Einstein condensation in polariton systems, it was natural to expect superfluid behaviour and Amo et al. observed it experimentally in 2009 [3]. The experiment (previously proposed by Carusotto and Ciuti [111]) was focused on observing how when superfluidity is achieved the

fluid flows without friction so that the usual scattering on defects disappears.

As showed in figure 2.14 a laser with a well-defined energy and momentum excites polaritons in a point of the dispersion curve (near the bottom of the LPB). Then the dispersion blue shifts because of polariton-polariton repulsive interactions (see Section 2.7). Polaritons injected can elastically scatter to states with the same energy, but when the superfluid is achieved there are not any other states of the same energy available for scattering (Fig. 2.14) and the fluid is able to flow unperturbed [3,16,111]. In other words, the key condition for superfluidity to appear is that the dispersion of the excitation becomes linear in some k vector range (fig 2.14), meaning that a sound velocity can be calculated for the polariton fluid:

$$c_s = \sqrt{\frac{\hbar g|\psi|^2}{m}} \tag{2.36}$$

Where $|\psi|^2$ is the polariton density and m is the polariton effective mass. If this sound velocity is greater than the flow velocity of the polariton fluid the Landau criterion for superfluidity is satisfied [2].

Further observations were made in a later paper [112], where condensate wavepackets moving at high velocities ($\sim 106m/s$) collided with a variety of defects. Polaritons were injected by a continuous wave pump at $k \sim 1\mu m^{-1}$ while parametric scattering was stimulated by a pulsed laser at a higher k vector. The main results of this configuration combined with nonlinear interactions are a linear polariton dispersion accompanied by diffusionless motion and splitting into two fluids when the obstacle is comparable to the size of the wavepacket.

As mentioned before, a superfluid is irrotational, so if a portion of a superfluid is given some angular momentum, this cannot be sustained over the whole superfluid region and instead remains localised as a singularity. In a 3D geometry these singularities can form lines, if they terminate at the boundaries of the liquid they are called vortex lines if they close upon themselves then they are vortex rings. A vortex only disappears by reaching the boundary or by annihilating with an antivortex of opposite circulation [113]. Quantized vortices in polariton condensates were observed in 2008 by Laugoudakis et al [114], the polariton condensate was pumped non-resonantly with a CW laser and cross-correlation techniques [4,115] were used to probe the presence of vortices and the characteristic 2π phase rotation. Three years later, Roumpos et al. showed experimentally that pairs of vortices and anti-vortices can be created in an exciton polariton condensate by generating a minimum density at the centre of a pumping spot [21].

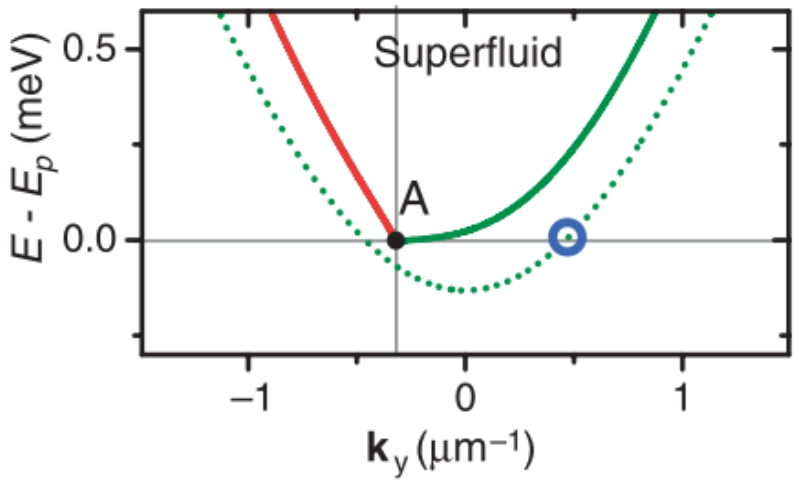

Figure 2.14: Theoretical polariton dispersion curve when superfluidity regime is achieved. Green dotted line: spectrum of excitations under low power non resonant pumping for $k_p = 0.3\mu m^{-1}$ (point A). E_p is the energy of the pump beam. Solid line: spectrum of excitations under strong pumping for the same k_p, superfluidity is achieved as now there is not any state with the same energy as the pump for scattering, and the dispersion becomes linear (red line) for a range of k vectors. Source [16]

2.11 Solitons

Solitons are localised temporal or spatial wavepackets that maintain their shape over propagation, usually stabilised by a non-linear process. Opposite to Bose-Einstein condensates (discussed in section 2.9), soliton's profiles are localised in real space and broad in k-space.

The study of solitons started in 1844 with the work of John Scott Russell [116]. He described the observation of water waves produced by a ship in the Union Canal in Scotland. Scott Russell noted the formation of a well-defined heap of water that he described as a solitary elevation that travelled with constant velocity along the channel for 2-3 km preserving its shape. Since his discovery, solitons have been observed in many different systems such as proteins [117, 118], DNA [119], oceanic rogue waves [120], interstellar molecular clouds [121]and even some clouds that are formed in Northern Australia (fig 2.15). All of them fulfilling the 3 characteristics of a soliton defined by Drazin and Johnson in 1989 [122]: shape-maintaining, self-localization and that when colliding with other solitons the only change they suffer is a phase shift.

In optics, the development of lasers made possible to study solitons in different systems such as waveguides [123,124] and optical fibres [125–127] . The creation of a soliton laser was achieved in 1984 by Mollenauer et al. [128] and more recently, in 2006, the observation of the supercontinuum spectra in photonic crystal fiber [129] was directly linked to solitons formation [130].

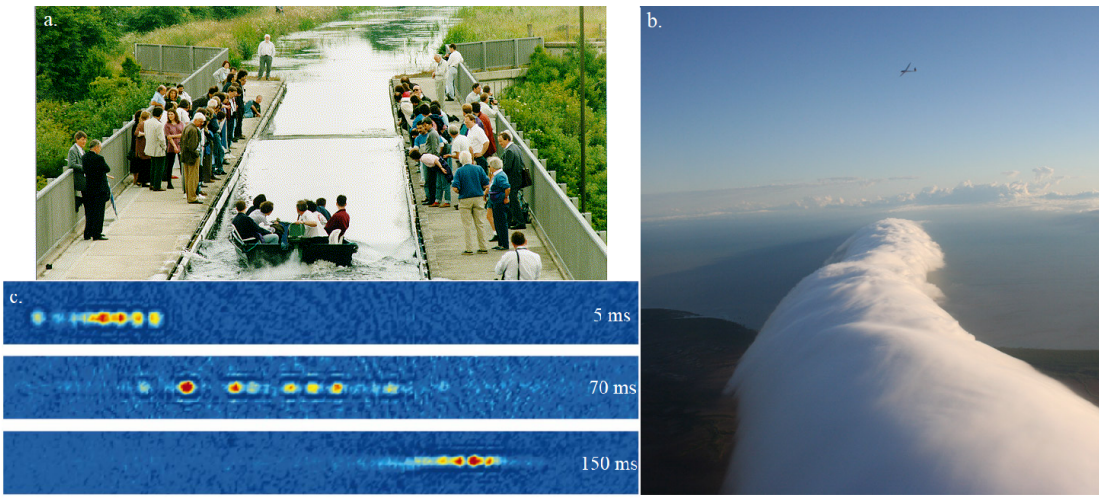

Figure 2.15: Different examples of solitons. a) Recreation of Russells first observation of solitons made for the ceremony of naming the Russell Scott Aqueduct in 1995 [131]. b) Photograph of a Morning Glory Cloud formed in Australia, the cloud can by described as a soliton [132]. c) Bright Soliton observed in a BEC [133].

In general, solitons can be classified into two categories: temporal solitons and spatial solitons. Temporal solitons occur when the electromagnetic field is already confined and pulses preserve their shape because nonlinear effects balance the dispersive spreading. For spatial solitons, self-focusing due to a nonlinear refractive index compensates diffraction [134, 135].

There has been a growing interest in the study of optical solitons because of their vast possible applications. In optical fibres, they have been used to transmit data over long distances without degradation [126, 136]. They have also been proposed for on-chip applications in the micro and nanoscale [124,137]. This requires the competing nonlinearities and the dispersive or diffractive effects to be short in time and length, which happens in polariton systems.

As an introduction for polariton solitons, the following sections describe the major observations of optical solitons in nonlinear media, semiconductor waveguides, optical fibres and BECs.

Table 2.1: Table of key conditions for soliton formation in different systems. For soliton formation in polariton waveguides conditions are the same as for nonlinear media.

	Bright Solitons	Dark Solitons
Nonlinear media self (de)focussing media balances dispersion	$n_2 < 0$: self defocussing media (e.g. liquid crystals) $\beta_2 > 0$: normal dispersion	$n_2 < 0$ $\beta_2 < 0$
	$n_2 > 0$: self focussing media (e.g. glass waveguides) $\beta_2 < 0$: anomalous dispersion	$n_2 > 0$ $\beta_2 > 0$
Fiber Optics SPM balances dispersion	$\gamma > 0$: positive nonlinearity for SPM $\beta_2 < 0$: anomalous dispersion	$\gamma > 0$ $\beta > 0$
Bose Einstein Condensates Particle interactions balance dispersion	$m^* > 0$: positive effective mass (e.g. atoms) $g < 0$: attractive interactions	$m^* > 0$ $g > 0$
	$m^* < 0$: negative effective mass (e.g. BECs in optical lattices) $g > 0$: repulsive interactions	$m^* < 0$ $g < 0$
Polariton system Repulsive polariton-polariton interaction balances dispersion	$m^* < 0$: negative effective mass $g > 0$: repulsive interactions	$m^* > 0$ $g > 0$

Depending on whether the soliton consists of a local maximum over a homogeneous background or the opposite, they are classified as bright or dark respectively. A brief summary of the main conditions for soliton formation, depending on the nonlinearity sign and system is given in table 2.11 and each case will be discussed in detail in the rest of this chapter. The parameters showed in the table are: nonlinear refractive index (n_2), GVD parameter (β_2), nonlinear parameter (γ), coupling constant (g) and effective mass (m^*).

2.11.1 Optical Solitons

In optics, solitons are formed when a balance between the dispersion or difraction and nonlinear effects is reached. Mathematically, the term soliton refers to solutions of nonlinear partial differential equations, Maxwells equations in the case of light, which show the 3 properties described before: shape maintaining, self-localization and only a change of phase after collisions.

Wavepackets travelling along the z-direction, with an electric field defined by the mode in the x-direction can be described by the following Nonlinear Schrödinger Equation (NLSE) [45]:

$$i\frac{\partial U}{\partial Z} + \frac{1}{2}\frac{\partial^2 U}{\partial X^2} \pm |U|^2 U = 0 \tag{2.37}$$

Where the following substitutions where made in order to get a dimensionless equation,

$$X = x/\omega_0, Z = z/L_{DF}, U = A\sqrt{k|n_2|L_{DF}} \tag{2.38}$$

where A(x,z) describes the envelope of the beam (meaning that the optical intensity that can be recorded experimentally is proportional to $|A|^2$), ω_0 is related to the beam waist of the input beam and L_{DF} is the diffraction length, or Rayleigh length, defined as the distance along the propagation direction from the waist of the beam to the place where its cross section doubles. Equation 2.37 has dark and bright solitonic solutions, depending of the nonlinearity sign, and it can be rewritten to describe temporal solitons (2.11.3).

2.11.2 Spatial Optical Solitons in Nonlinear Media

Nonlinear media, also known as Kerr media, is characterized for having a non-negligible $\chi^{(3)}$ (2.33), which means a dependence of their refractive index on the light intensity ($n = n^{(0)} + n^{(2)}|E(t)|^2$).

The NLSE can be integrated for a Kerr medium generating a bright soliton solution of the form [138]:

$$U(X, Z) = U_0 sech(U_0 X) e^{iU_0^2 z/2} \tag{2.39}$$

Where U_0 is the peak amplitude of the soliton in dimensionless units. This solution refers to a bright soliton because it consists of a local maximum over the homogenous dark background. The size of the soliton depends on the amplitude of the optical intensity, the nonlinearity strength and the dispersion length, defined as the distance after which the pulse broadens by a factor of $\sqrt{2}$.

Spatial solitons due to the Kerr nonlinearity have been observed in a planar

glass waveguide [123]. In this case, solitons exist due to the balance between self-focusing and diffraction.

Self-focusing is a process that happens in nonlinear media whose diffractive index increases with the electric field intensity. Media with a positive $n^{(2)}$ acts as a focusing lens for a Gaussian beam while media with a negative index broads the beam in a process known as self-defocussing. Bright spatial solitons arising from a saturable self-focussing linear medium have also been studied [139].

Solitons can be present in self-defocussing media too, but there they consist on a dip in intensity compared to the homogenous bright background, which is why they are referred as Dark Solitons. This solitonic solution is given by [138]:

$$U(X,Z) = U_0(\cos\phi \tanh(U_0 cos\phi(X - vZ)) + isin\phi)e^{iU_0^2 z} \tag{2.40}$$

Where v is the transverse velocity and U_0 is the peak amplitude of the soliton, both in normalized units [140], and $\pi - 2\phi$ is the total phase shift across the dark notch. An ideal dark soliton will have a total phase-shift of π, if it is less than ϕ then the minimum intensity of the notch is bigger than zero and it is known as a grey soliton.

The first observation of dark solitons was done in bulk nonlinear media [141, 142], followed by many different systems [143–145] including polaritons as it will be discussed in section 2.12.

2.11.3 Temporal Solitons in Optical Fibers

The NLSE described in the previous section (Eq 2.37) can be rewritten for temporal coordinates, becoming:

$$i\frac{\partial U}{\partial Z} + \frac{1}{2}\frac{\partial^2 U}{\partial \tau^2} \pm |U|^2 U = 0 \tag{2.41}$$

Here (in a way similar to 2.37) the following substitutions have been made for the resulting dimensionless NLSE:

$$Z = \frac{z}{L_D}, \tau = t - \frac{Z}{v_g}, U = A\sqrt{L_D|\gamma|} \tag{2.42}$$

Where L_D is the dispersion length defined as the propagation distance for a pulse before broadening in duration by a factor of $\sqrt{2}$ due to the group velocity dispersion (see 2.5.3). In terms of the GVD parameter β_2, the dispersion length is given by: $L_D = T_0^2/|\beta_2|$, where T_0 is the input pulse width.

The temporal-NLSE (Eq 2.41) has a solitonic solution given by:

$$U(0, \tau) = Nsech(\tau) \tag{2.43}$$

Which is a bright temporal soliton travelling in the z-direction. N gives the solitons order, and when N=1 it is referred as a fundamental soliton, where a pulse with an envelope $sech^2$ propagates preserving its shape.

Temporal solitons are the result of a balance between the dispersion and some nonlinearities. In the case of N=1, the dispersion length equals the nonlinear length, which is the distance needed to get a phase change of 2π.

Temporal solitons can also be understood as the result of the effects of self-phase modulation (SPM) due to the nonlinearity being cancelled out by a negative group velocity dispersion (GVD) (see section 2.5.3). SPM is produced in a medium where the refractive index varies with the intensity, giving a nonlinear component to the phase of a photonic wave propagating in it: $\phi_{NL}(t)\alpha n^{(2)}|E(t)|^2$, meaning that the phase varies over the duration of the pulse. At a point in time t, the change in the nonlinear phase determines the change in frequency in the pulse profile. This will lower the frequencies at the leading half of the pulse and raise them at the end.

As explained by Mollenauer et al. [125], the interplay between a negative GVD and SPM is required to observe temporal solitons in an optical fibre. In an optical fibre with anomalous dispersion, the GVD increases with frequency so that light at the trailing half of the pulse that has been blueshifted by the SPM starts to catch up with the redshifted light from the beginning of the pulse. As blue light starts to approach the leading half, it is slowed down by the group velocity dispersion and redshifted by the SPM. In other words, high frequencies will be faster than low frequencies, so that SPM results in pulse compression reducing the broadening effect of the GVD [127]. In contrast, for a medium with a positive GVD high frequencies are slower than low frequencies, meaning that SPM would only increase the GVD broadening effect.

The main application of temporal bright solitons has been telecommunications, as they can travel long distances maintaining their shape and amplitude [126]. Other applications include a soliton laser [128] and supercontinuum generation [146, 147].

Equation 2.41 also admits dark soliton solutions of the form: $U(0,\tau) = Ntanh(\tau)$. They can be created in a regime with a positive GVD and positive nonlinearity (determined by the nonlinear parameter γ which is proportional to $n^{(2)}$, positive, and responsible for the SPM [148]). Dark solitons were observed in optical fibers a few years after bright solitons [149,150]. Even though the use of bright solitons for communications is more extended, dark temporal solitons have been used for communication security [151] and for the creation of dark soliton lasers [152].

2.11.4 Matter-Wave Solitons in atomic BECs

Condensates used as a macroscopic matter-wave can also form stable solitons; in this case, the wavepacket dispersion is compensated with the nonlinearity due to atomic interactions. The behaviour of a Bose-Einstein condensate (BEC) can be described by the Gross-Pitaevskii equation:

$$(-\frac{\hbar^2 \bigtriangledown^2}{2m} + V_{ext} + g|\psi|^2)\psi = E\psi \tag{2.44}$$

Where m is the (positive) mass of the atomic boson, V_{ext} is the external potential, g is the coupling constant describing the strength of the particle interactions and ψ is the wavefunction describing the condensate.

The Gross-Pitaevskii equation (GPE) is similar to the NLSE (Eq. 2.37), with the difference that the origin of the nonlinearity in the GPE is the interaction between particles. In the same way, the GPE has solitonic solutions depending of the interactions sign; if the interactions are attractive, $g < 0$ and bright solitons arise:

$$\psi(x) = \psi_0 \frac{1}{cosh(x/\xi\sqrt{2})} \tag{2.45}$$

Where $\xi = \hbar/\sqrt{2mg|\psi_0|^2}$ is the healing length of the fluid and determines the size of the solitons.

Bright matter-wave solitons were first observed in an ultracold lithium-7 gas by Khaykovich et al. [133,153]. As the natural inter-atom interactions are repulsive, to get bright solitons, interactions are continuously tuned to attractive to balance the dispersive spreading due to kinetic energy. In Khaykovich experiment,

BEC atomic interactions were tuned into attractive and then the condensate was released in a one-dimensional waveguide, obtaining a soliton that propagates without dispersion over a 1.1 mm distance [153]. Solitons trains were also observed with this configuration, showing repulsive interactions between them (Fig 2.15 c.).

Another solitonic solution of the Gross-Pitaevskii equation corresponds to the formation of Dark Solitons obtained when considering repulsive interactions $g > 0$ [45]:

$$\psi(x,t) = \psi_0(cos\phi tanh(cos\phi\frac{x-vt}{\xi\sqrt{2}}) + isin\phi) \tag{2.46}$$

Because the natural inter-atom interaction in a condensate is repulsive, dark solitons were observed before bright solitons. Although both kinds of polaritons are unstable, dark solitons were stabilised by the application of an external potential, elongating the condensate for a quasi-1D situation [154] or by imprinting a phase step in the BEC wavefunction [155].

Notice that we have discussed the formation of solitons for an atomic system with a positive effective mass. However, for the case of BECs loaded into optical lattices, the effective mass can also be negative [156]. Solitons have been observed in BECs in a periodic potential [157], where conditions for soliton formation change as showed in 2.11, according to the sign of the effective mass and the inter-atomic interactions.

2.11.5 Vector Solitons

A vector soliton is a solitary wave that propagates maintaining its shape just like a scalar soliton. The difference between a vector and a scalar soliton is that the first one has multiple polarization components while the scalar has effectively only one.

In the same way than scalar optical solitons, vector solitons are called temporal or spatial depending on whether they are localized in the time or spatial domain. Vector solitons are formed by two orthogonally polarized components of a single optical field or two fields of different frequencies but the same polarization. There are vector bright, dark and dark-bright solitons. Vector bright and dark solitons are characterized by a peak or depletion, respectively in both polarization components, whilst vector dark-bright solitons are formed by a dark soliton in one component and a bright soliton in the other.

Vector solitons were first theoretically predicted in 1988 for a birefringent dispersive medium [158]. Since then, vector solitons have been observed in multiple systems such as photorefractive media [159], VCSELs [160] and optical fibres [161],. The spatio-temporal polarization of conservative solitons in polariton microwires will be extensively discussed in Chapter 6.

2.11.6 Dissipative Solitons

The solitons discussed in the previous sections are called Conservative solitons, because they are formed in low losses systems (BECs, optical fibres, waveguides), meaning that the number of particles in the wavepacket remains constant. Conservative solitons have a well-defined width because it depends on the amount of particles in the wavepacket.

Contrary to conservative solitons, dissipative solitons appear in systems with high losses. In these systems the number of particles decrease so quickly that the only way of observing solitons is by using an external pump to replenish the particles population, compensating the losses.

Dissipative spatial solitons were observed in weak coupled microcavities and are often referred to as cavity solitons. In microcavities, the refractive index increases with light intensity, which means that depending on the optical excitation power the system can be turned into resonance with the cavity photon resulting in a bistable system. Bistability can be observed in weak and strong-coupled cavities [162]. In the strong coupling regime an s-shape curve is obtained when plotting the polariton population against the excitation power (figure 2.16).

Bistability allows the formation of solitons in the following way. Initially a large area is pumped in a low density state, then utilising a writing pulse, it is excited into a high density state. Once the writing pulse is switched off the region remains in the high density state maintaining the soliton size over time. Dissipative solitons were observed in semiconductor resonators in 2001 [163], and 10 years later in polariton systems [19]. Polariton solitons, including dissipative bright solitons are discussed in detail in the following section.

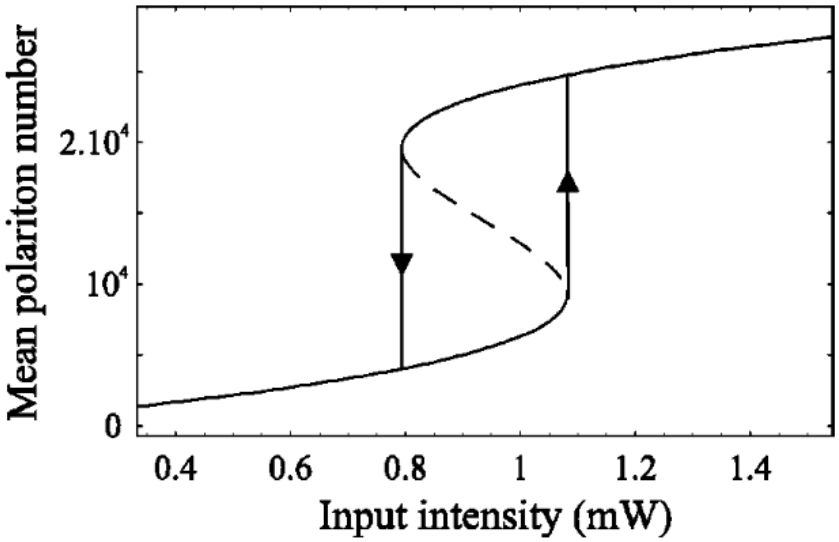

Figure 2.16: Example of the bistability curve in a polariton system. Intensity of the polariton field (the mean number of polaritons) vs the input power is plotted. The dotted line is the unstable branch in the bistable regime. The arrows indicate the hysteresis cycle obtained by scanning the input power in both directions. Source: [162]

2.12 Solitons in polariton systems

As showed in the previous section 2.11 there is a huge range of different kinds of solitons, and many of them have been observed in exciton polariton systems. In a similar way to BECs (2.11.4), polariton de-focussing nonlinearity arise from the repulsive polariton-polariton interactions. To form a soliton, this nonlinearity must be compensated by the kinetic energy. In this section, I will review the main realizations of polariton solitons in microcavities and waveguides related to the work presented in this thesis.

Before proceeding into the particular observations of polariton solitons, it is worthwhile to mention that the polariton nonlinearity is much higher than the ones measured for the different systems mentioned in the previous sections. The polariton Kerr nonlinearity is 3-4 orders of magnitude larger than that in weakly coupled photonic systems. The nonlinear refractive index measured for polariton waveguides in [164] is $-1.6x10^{-14}m^2/W$, which corresponds to a nonlinear parameter $\gamma = -18000W^{-1}m^{-1}$, for comparison, in optical fibers $\gamma = 0.0011W^{-1}m^{-1}$ and in GaInP photonic crystal waveguides $\gamma = 920W^{-1}m^{-1}$ [45]. This extremely

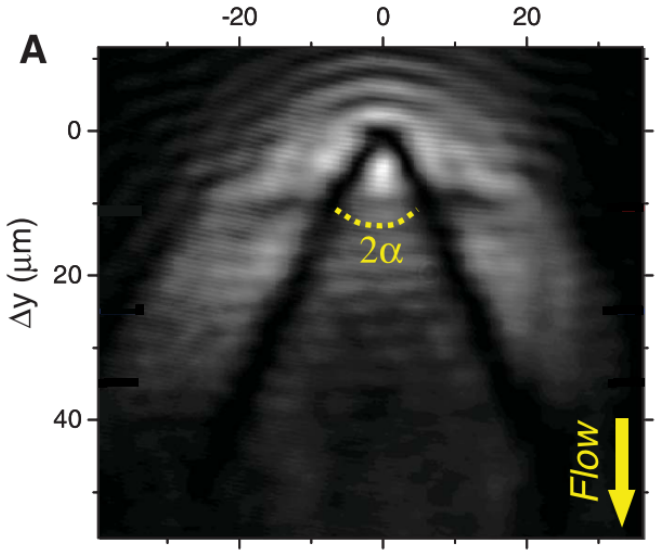

Figure 2.17: Real-space emission showing a dark soliton doublet nucleated in the wake of a photonic defect. Source: [165]

high nonlinearity allows the formation of solitons at lower excitation energies, for instance $1.3 - 1.4$ orders of magnitude less than the 12pJ pulse energy at which solitons are formed in InGaP [124].

2.12.1 Oblique dark solitons in polariton superfluids

The first observation of dark solitons in a polariton fluid was made in 2011 by Amo et. al. [165]. These solitons appear by putting a defect in a superfluid. As explained in 2.10 superfluidity is characterized by a flux without friction, therefore when the fluid hits a static object at speed below some critical velocity it passes unperturbed. For faster velocities, small objects induce dissipation via the emission of sound waves [166]. Objects bigger than the healing length (the distance induced by particle interactions for changes in the condensates density) produce density modulations that can create topological excitations such as solitons [165, 167].

Amo's group experimentally observed the formation of pairs of highly stable oblique dark solitons [165]. Following the theoretical proposition published one year before [167], they introduced a defect in the polariton fluid and increased the flow velocity until soliton nucleation was achieved. Polariton feeding was done by pumping the system quasi-resonantly with a continuous-wave laser creating a

polariton fluid with a well-defined in-plane wave vector [3]. Polaritons then propagate, past the defect (which is a natural photonic defect in the microcavity) and extend downstream of it. The solitons appear due to the gradient of low speeds occurring around the defect, which results in density variations. The repulsive polariton-polariton interactions stabilize the solitons shape as it propagates. Additionally, they measured the characteristic phase jump of up to π across the soliton.

Because dark solitons develop in the unpumped region where polaritons propagate out of the excitation spot, the condensate phase is left free to evolve and the system can be described by the Gross-Pitaevskii equation with losses but without gain [167], making them Conservative dark solitons.

Amo's observation of polariton dark solitons is considered controversial, because, as discussed in [168], some of the signatures used to claim dark soliton formation such as the abrupt jump in the phase across the soliton, can also occur in the linear regime. A more recent observation of polariton dark solitons was done by Paul Walker et al. in a polariton waveguide (see 2.12.4), where a successful measurement of the soliton width and its dependence with density shows an irrefutable proof of dark solitons formation [169].

2.12.2 Dissipative bright solitons in microcavities

Dissipative solitons were the first type of bright solitons observed in planar microcavities. As mentioned in section 2.11.6 they can be generated in strong coupled microcavities in a similar way to VCSELs, using a continuous external pump to compensate the losses associated with the short polariton lifetime, which is usually on the order of 10 ps [19,100] and around 100 ps in high Q microcavities [170].

Solitons are formed from the balance between the dispersion due to polariton-polariton interactions and the kinetic energy. Repulsive polariton-polariton interactions (2.7) produce a potential with energy U=Ng, where N is the number of particles and g is the polariton-polariton interaction coefficient, promoting the broadening of the wavepacket. This spreading must be compensated by a negative kinetic energy, in order to create a soliton. The kinetic energy is given by $K = \frac{\hbar^2}{2m\xi^2}$ where ξ is the healing length of the polariton fluid, and half of the width of the propagating wavepacket. As the LPB of the microcavity dispersion has a region where the effective mass becomes negative (above the inflection point, Fig. 2.10), it means that the kinetic energy is also negative for this area.

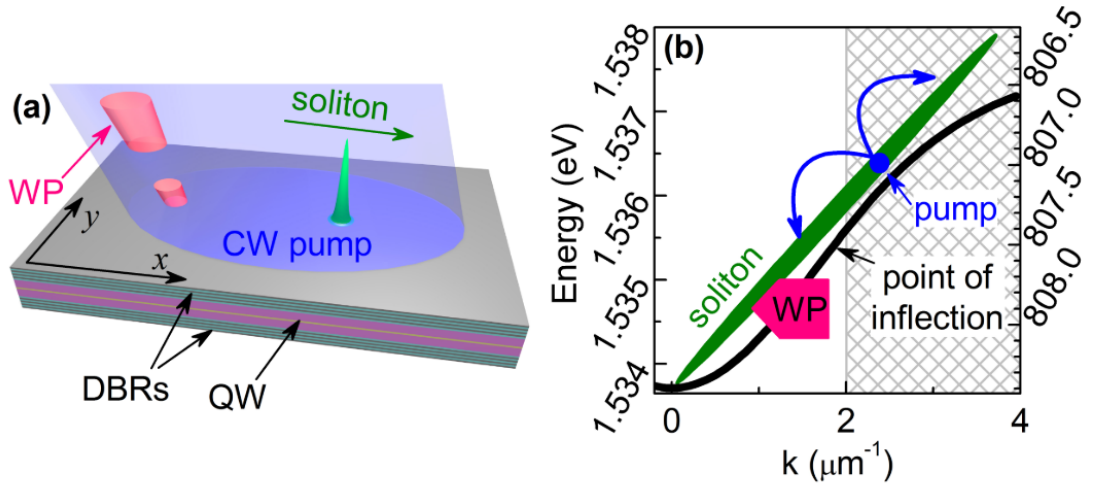

Figure 2.18: (a) Schematic diagram of the experiment carried out by Sich et al. [19] The CW pump is focused quasi-resonantly into a big spot in the sample. A picosecond writing beam is focused into a smaller spot and triggers soliton formation. (b) Dispersion diagram of the lower polariton branch. The location of the pump and writing beam (WP) in energy-momentum space are shown. Taken from: [173]

Polariton dissipative bright solitons were theoretically predicted by Egorov et al. in 2009 [171] and experimentally observed 3 years later by Sich et al [19]. A linearly polarized CW laser was used to pump polaritons in the inflection point of the LPB, to ensure the negative effective mass. In addition, the pump laser was also in the bistable regime (just before the threshold) 2.11.6, then with a second (pulsed) laser, a high density wavepacket was triggered, using the associated parametric instability of the bistable regime to enable scattering from the pump to the continuum of momenta forming the soliton (Fig. 2.18).

It is worthwhile to remark that the inflection of the dispersion curve provides only localization in one dimension, as the effective mass in the direction perpendicular to the propagation is always positive ($k_y = 0$). Perpendicular localization is achieved thanks to the pump beam, which can act as a barrier for soliton spreading. Localization can be explained by a mechanism involving parametric scattering from the pump ($k_x = k_p, k_y = 0$) to a signal ($k_x = 0, k_y = 0$) and an idler ($k_x = 2k_p, k_y = 0$) states (see 2.8). Above some threshold the scattering is triggered, depleting the pump population. The reduction of the pump population changes the effective potential of the system limiting the spread of the wavepacket [76, 172].

2.12.3 Solitons in microwires

The practicality of using microwires for circuit applications [6, 174] has encouraged the research of microcavity polariton systems in one dimension. Additionally, optical solitons have been used for communications since the last century [125] because of their property of preserving shape over propagation. Soliton propagation in polariton microwires seems like the ideal combination for an optical signal processing device [7].

Tanese et al. made the first observation of solitons in a polaritonic wire system in 2013 [175]. Tanese's group fabricated wires with a periodically modulated width by etching a high-Q planar microcavity. The modulated width creates a periodic potential, which results in the creation of polariton mini-bands separated by mini-gaps in the dispersion. They observed the formation of gap solitons. They are a special kind of soliton where the group velocity dispersion (which is balanced by the nonlinear polariton interactions) results from the periodic variation in the energy potential. The wavefunction of the soliton has maxima at the edges of the mini-Brillouin zones where the effective mass is negative, and extends over many periods of the real space lattice.

Fabrication of microwires used in chapters 5 and 6 is simpler than for the ones used by Tanese's group, as we used rectangular wires (3.1.2). The modulated width is not needed because the solitons that we will study arise from the same mechanism that for dissipative solitons (2.12.2): the balance between the negative polariton mass and the nonlinear interactions. Localization in the direction perpendicular to the pulse propagation arises from the vertical confinement of the structure, meaning that the CW pump laser used in the dissipative configuration 2.12.2 is unnecessary. Wavepackets propagation in polariton microwires and their behaviour was initially discussed in Chana doctoral thesis [176]. She excited the polariton microwires with a writing beam (and without the pump beam used in the 2D microcavity case [19]) and observed a solitonic-like self-focussing. She excited the three modes of the LPB at the same time allowing intermodal polariton-polariton scattering and observed the emergence of a single dominant mode, where it is not possible to resolve the individual energy modes in momentum space. The presence of this dominant mode coincides with a narrowing of the pulse and the appearance of the soliton [177].

In the work presented in this thesis, we excited the ground mode of the LPB and observed the formation of Bright Conservative Solitons in microwires. The formation of these solitons and of the accompanying Cherenkov radiation will be discussed in detail in chapter 5, whilst polarization properties of the solitons are presented in 6.

2.12.4 Solitons in polariton waveguides

As discussed in section 2.4 polariton effective mass on the LPB is negative at any momentum in waveguides (Fig 2.10), so soliton formation is expected from the balance between the kinetic energy and the repulsive polariton interactions.

Conservative dark and bright solitons have been observed in polariton waveguides [164, 169]. Walker et al. reported temporal bright solitons formation in 2015 [164]. Temporal bright solitons result from the compensation of self-phase modulation (SPM) due to the nonlinearity by a negative group velocity dispersion (section 2.11.3). As discussed in 2.5.3, polariton waveguides have a range of negative GVD, and with their fast polariton velocity ($30 - 50\mu m/ps$) and giant nonlinearity, they are a particularly convenient system for soliton formation.

Walker et al. [164] used the same sample described in (3.1.1), which is a planar AlGaAs/GaAs waveguide. The sample was excited resonantly with a subpicosecond pulse at different powers and the output was detected after the pulse propagated 600 μm. At low power, significant temporal spreading was observed. As the pulse energy was increased above threshold, the pulse became shorter, when the energy was about 0.5 pJ the duration of the pulse narrowed below the 2 ps resolution. Such temporal compression occurring at a critical energy is characteristic of the soliton formation. In addition, Walker et al. showed that all the spectral components of the soliton travel at the same velocity.

Also in [164], Walker et al. reported the observation of 2D dark-bright spatiotemporal solitons. These wavepackets simultaneously show bright soliton behaviour in the temporal dimension and dark soliton behaviour in the transverse spatial dimension. For this observation, Walker et al. sent a wavepacket into the input grating with an intensity distribution along x of two lobes (each one ~ 10 μm long) separated by a dark notch at x=0, where the field undergoes the characteristic π phase jump of dark solitons. The phase shift is achieved by passing the laser beam through a phase plate consisting in a thin glass microscopy cover-slip They observed, as in the bright temporal case, that at low power, the bright polariton field spreads in time and at high power the spread is cancelled and the dark notch is narrowed. At the same time, the temporal duration of the pulse decreases from 4.7 ps to 3.6 ps.

The observation of dark solitons in a waveguide polariton fluid was reported last year [169]. For these experiments, Walker et al. used the same planar waveguide (3.1.1) to study dark soliton formation in the high-momentum regime. As in the oblique dark solitons experiments previously described (2.12.1), dark solitons form from the balance of the kinetic energy related to the size of a defect in

the fluid, and the nonlinear potential energy, which depends on the density of the background. To prove the formation of solitons, Walker et al. measured the width of the wavepacket and demonstrated that it depends on the density. They sent an input profile with either a 2π phase jump or an intensity dip near the centre and observed the evolution of the polariton fluid over a 600 μm propagation. When the initial condition was a phase jump, they observed the formation of a single dark soliton, and when the condition was the intensity dip, dark soliton pairs formed. In both cases, the dark notches widths decreased with increasing density, satisfying the width-density criterion for dark solitons.

As mentioned in 2.12.1, the main difference between Amo's observation of oblique dark solitons [165] and Walker's [169], is that the second successfully shows the relation between the soliton's width and the fluid density, which is possible thanks to the use of waveguides. The fluid velocity in the waveguide used by Walker is 24 $\mu m/ps$, ten times larger than in microcavities, which allows them to work in the supersonic regime where dark solitons widths can be measured over a wide range of background densities (by varying the excitation power). On the other hand, microcavities as the one used by Amo et al. do not allow such a wide range of densities to study the solitons because when increasing the fluid density there is a transition from supersonic to subsonic regime (due to the shape of the LPB), preventing the nucleation of solitons before a strong change of the soliton width could appear.

Chapter 3

Experimental Methods

In this chapter I describe the samples and experimental methods used for the work presented in chapters 4, 5 and 6. Both samples used for this thesis are GaAs-based, thereby they have to be kept at low temperature (4 to 12 K) during the experiments. Samples are described in section 3.1, the cooling method is briefly described in section 3.2 with the optical setups used for reflection and transmission measurements and the different configurations for pulsed and continuous excitation. Finally, details about the use of the streak camera for time resolved measurements are included in section 3.3.

3.1 Samples

The description of the 2 samples used for experiments is presented in this section. Both samples used were grown by Molecular Beam Epitaxy (MBE) and etched by Electron Beam Lithography (EBL) after. The waveguide sample was grown at the University of Cambridge and the gratings were etched at Sheffield, the microwire was both grown and etched at the University of Sheffield.

3.1.1 Polariton Waveguide

The polariton waveguide used for optical amplification experiments (Chapter 4) was grown over a GaAs substrate and it consists of a cladding layer of $Al_{0.9}Ga_{0.1}As$ followed by a 45 nm GaAs layer, 3 $In_{0.04}Ga_{0.96}As$ QWs (10 nm each

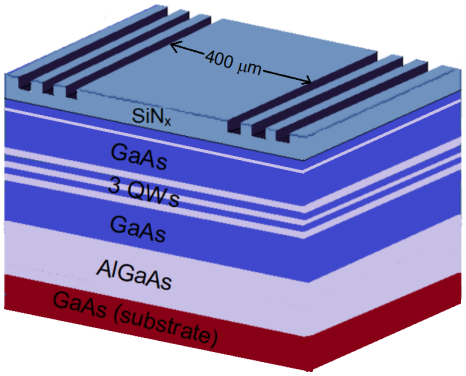

Figure 3.1: Waveguide sample: A GaAs waveguide with 3 InGaAs quantum wells embedded in the core.

one, separated by 10 nm GaAs barriers) and 57 nm of GaAs. Finally a 3 nm $Al_{0.9}Ga_{0.1}As$ etch stop layer and 20 nm of GaAs were grown (Fig. 3.1). After the growth, to couple light in and out of the sample (see 2.4.4), 100x100 μm^2 grating couplers (250 nm grating period), were etched on a SiN_x layer by EBL and reactive ion etching [45].

This sample was previously characterized by L. Tinkler and P. Walker [15, 45, 164]. They reported a 9 meV Rabi splitting and a polariton life time of ∼10 ps.

3.1.2 Polariton Microwire

All the experiments that show bright conservative soliton propagation and its accompanying effects such as Cherenkov radiation and polarization domains (Chapters 5 and 6) were performed on the microwire described in this section. The necessity of using a polariton microcavity wire instead of a waveguide for those studies arises from the different polariton energy-momentum dispersions of each system (see 2.5.3) . As it will be fully explained in the following chapters, these effects are possible thanks to the particular shape of the microwire lower polariton branch (LPB), where the polariton effective mass changes its sign depending on the energy and k-vector, allowing the formation of bright solitons when exciting in the negative effective mass regime.

The microcavity consists in a $3\lambda/2$ cavity with 3 $In_{0.04}Ga_{0.96}As$ QWs. The top and bottom DBRs are formed by 23 and 26 repeats of $Al_{0.85}Ga_{0.15}As/GaAs$ respectively. The microcavity was grown by MBE on a GaAs(100) substrate, maintaining the growth temperature at 590 °C for the DBRs and 500 °C for the

3 QWs and the subsequent GaAs layers, achieving a Q-factor of over 15000 [178].

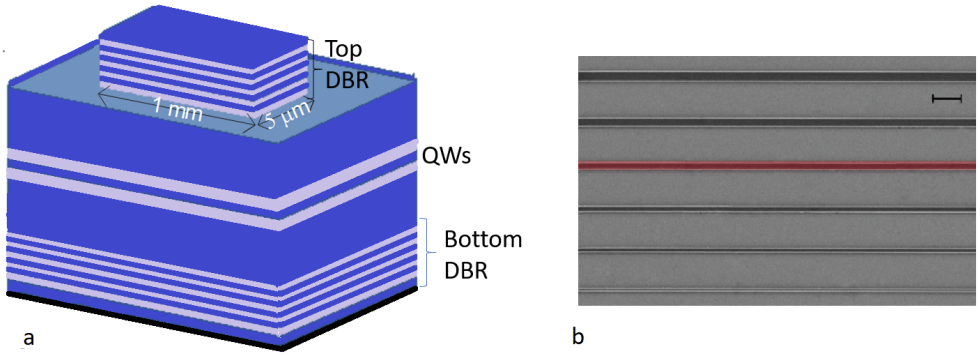

Figure 3.2: (a) Scheme of the microcavity wire: The top DBR of a microcavity is partially etched forming a mesa that confines the photonic mode and therefore the excited polaritons.(b) SEM image of the sample showing some wires with different widths, the wire used for all the experiments is highlithed. The scale bar is 20 μm.

To fabricate the microwire, the top DBR was partially etched by reactive ion etching, allowing confinement of the photonic mode without damaging the quantum wells. The microwire used was 5 μm wide and 1 mm long (Fig. 3.2). As mentioned before (2.5.4), wires are 1D multi-mode structures. The width of the wire determines the mode spacing. To increase the spacing between the modes and therefore reduce the amount of occupied modes, the width of the wire could be decreased. However, with narrower wires the surface roughness would be more significant, increasing the losses from the side walls making the polariton lifetime to drop and the emission dim [176]. The chosen width was small enough to observe well defined modes (see section 5.2) and a polariton lifetime of ∼30 ps. The polariton Rabi splitting for this sample is ∼4.5 meV.

3.2 Experimental Setups

The optical setups used in this thesis are described in this section. For all the experiments, the sample was kept at temperatures between 4 and 12 K inside a continuous flow helium cryostat. This cooling system works by a continuous pumping of liquid helium, which vaporises in the cryostat, cooling the finger and the sample. The cryostat has windows large enough to allow optical access to the sample from the back and the front. Transmission and reflection configurations used to excite each sample are described below, along with the different setups used for imaging and polarization measurements.

3.2.1 Real space and k space imaging setup

Real space (near-field) and k space (far-field) images were collected by a streak camera or by a CCD, for time resolved or time integrated measurements respectively (3.3).

Near field imaging can be used to record spectra as shown in chapter 4 or as a microscope when the grating inside the spectrometer is set to zero order and the entrance slit is fully opened (up to 7 mm). For time resolved measurements, near field imaging was used to observe the surface of the sample and the propagation of the solitons and Cherenkov radiation in Chapters 5 and 6, for those measurements the image was recorded by the streak camera (see 3.3).

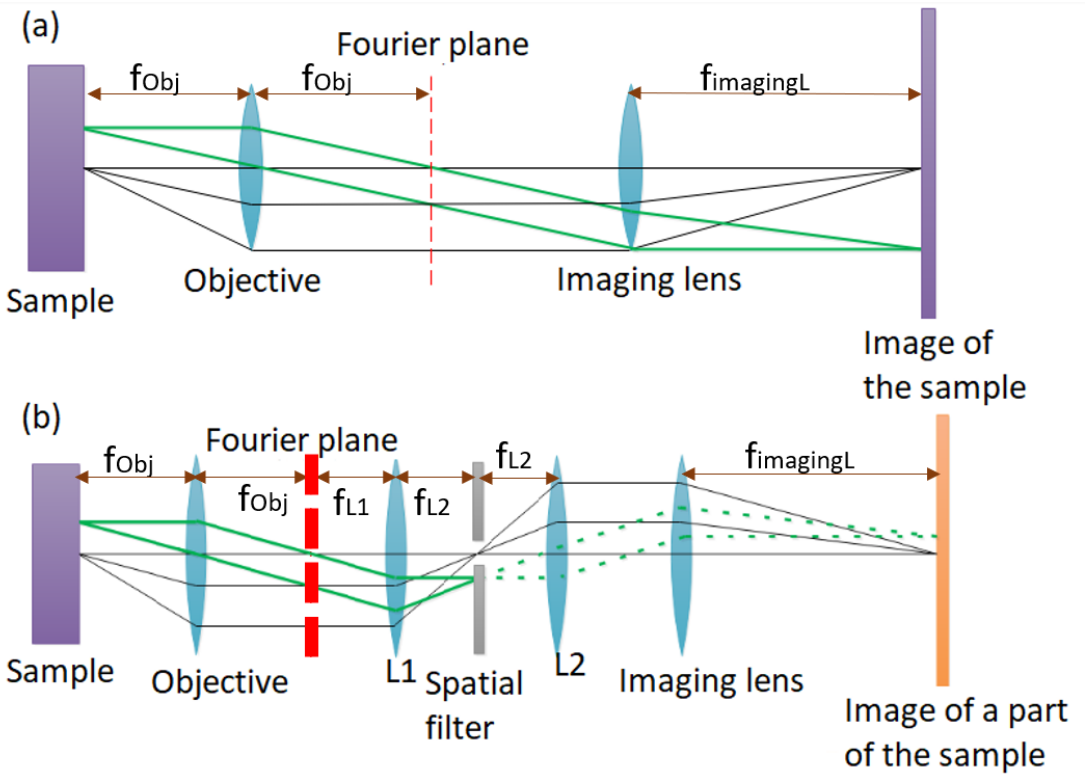

Figure 3.3: (a) Basic setup for near field imaging (b) Setup used for spatial filtered near field imaging

The near field image of the sample can be obtained by using the setup in figure 3.3. An objective is used to collect the PL emission from the sample and then a second lens is used to focus it on the entrance of the spectrometer. The final zoom of the image is given by the ratio of the focal length of the imaging lens over the one of the objective. To calculate the scale on the real space images

we simply take into account the zoom and the size of a pixel on the CCD, which is 13 μm.

To collect the light coming just from one part on the sample (as the images of light coming from the output grating in Chapter 4) an additional telescope is added to the setup as showed in Fig. 3.3 b), the slit put in between the lenses can be partially closed and moved to select a part of the image to be projected on the spectrometer. The new zoom of the image focused on the CCD is given by $\frac{f_{ImagingL} f_{L1}}{f_{Objective} f_{L2}}$.

Far field imaging is used for angle-resolved (k-space) measurements (Chapters 5 and 6). Spectrally resolved measurements were taken with the setup showed in Fig. 3.4. It projects the Fourier transform of the sample emission on the spectrometer entrance slit, which means that rays emitted by the sample at the same angle are focused at one point in the spectrometer. This image is then diffracted by the grating inside the spectrometer and directed towards the CCD (or the streak camera) to record dispersion curves: emission as a function of energy and momentum.

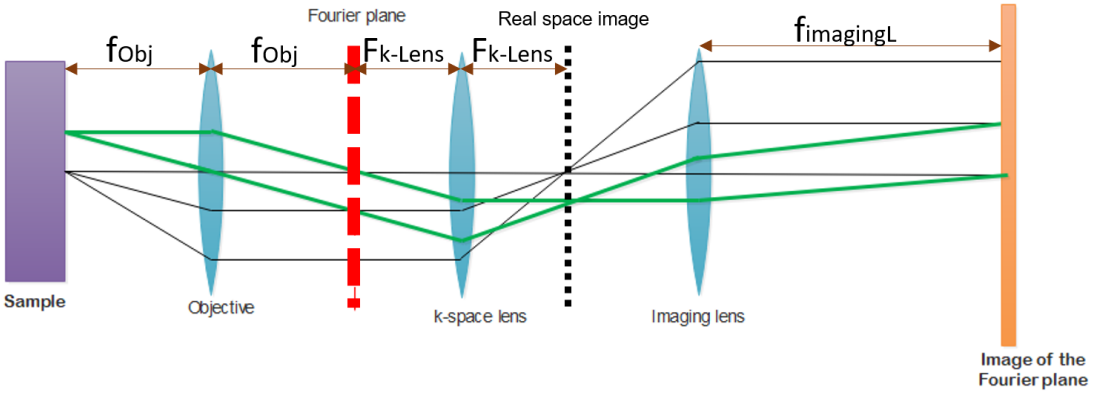

Figure 3.4: Setup for far field imaging

3.2.2 Optical Setup for characterization

Dispersion curves of the microwire sample (3.1.2) were taken for characterization. To measure the energy-momentum curves showed in chapter 5 the sample was excited off-resonantly (at 633 nm) with a HeNe laser using the reflection configuration of Fig 3.5. The laser reflection is filtered out with a long-pass filter placed before the imaging lens.

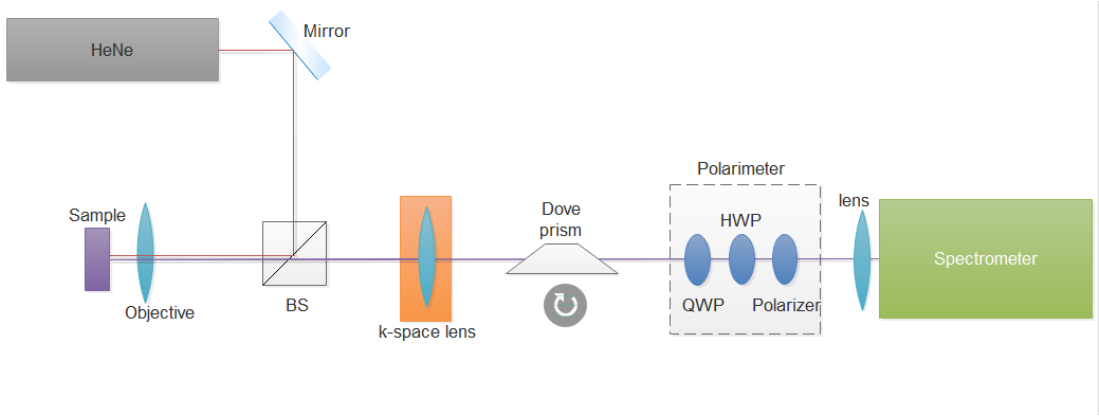

Figure 3.5: Setup used for sample characterisation. K-space lens is put in a flip mount to change between real and k space imaging.

To measure dispersion along and across the wire, a dove prism in a rotational mount is used. It can be rotated 90° to align the wire parallel or perpendicular to the entrance slit of the spectrometer.

A polarimeter formed by one $\lambda/4$ waveplate, one $\lambda/2$ waveplate and a linear polarizer was used to measure the TE-TM splitting of the microwire (5). The quarter waveplate and the half waveplate are mounted in rotational stages to allow the selection of the polarization to measure, and then a vertical polarizer filters the light send to the spectrometer. For linear polarization (V, H, D and A), the QWP fast axes is parallel to the polarization that we want to measure and then the HWP is rotated to change the polarization to vertical so that it will pass the polarizer. For circular polarization, it is transformed to vertical by the rotation of the QWP to 45 °(σ^+) or -45 °(σ^-).

3.2.3 Pulsed excitation

A Ti:Sapphire tuneable laser (Tsunami Spectra Physics) was used for the amplification experiments in the polariton waveguide (Chapter 4) and to trigger the formation of solitons in Chapters 5 and 6. For all the measurements, the laser was set to emit pulses with duration of $\sim$ 3 ps (the pulse shaper described in the following paragraphs was used to maintain this pulse duration independently of any fluctuation of the laser) or $\sim$ 5 ps, for the experiment described in section 5.4 of Chapter 5.

A process of characterisation of the laser pulses was carried out for all the

experiments. A fraction of the laser emission was sent to a spectrum analyser to verify the central wavelength of the pulse, at the same time, another part was sent to an autocorrelator to measure pulse duration, a third portion was used to trigger the streak camera (used in Chapters 5, 6). The rest of the laser beam was sent through a pulse shaper and then to the sample.

A pulse shaper was used to control the central wavelength and width of the pulses. The pulse shaper is formed by two diffraction gratings, two lenses and one slit arranged as showed in Fig. 3.6.

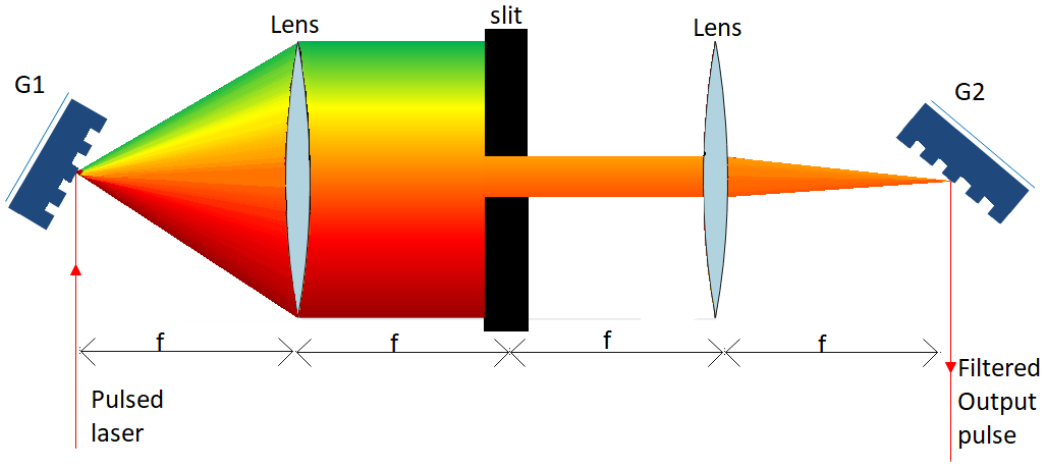

Figure 3.6: Pulse shaper used to control the central wavelength and duration of the pulses coming from the Ti:Sapphire laser. The colours in the image are used to explain the filtering of wavelengths, however, we worked only with infrared light.

The first grating disperses the spectral components of the pulse, which are then focused in the Fourier plane by a lens. Then the second lens and grating recombine all the frequencies into one collimated beam. A slit is collocated on the Fourier plane between the two lenses, if the slit is completely opened the output pulse is identical to the input.

By closing the slit we can select a region of energies out of the laser pulse while moving the slit changes the pulse central wavelength. The duration of the pulse is controlled by the slit aperture. Because time and energy are conjugated variables, a decrease in energy means an increase in the pulse duration. The slit aperture was set to get a final pulse of 3 ps for all the experiments involving pulsed excitation.

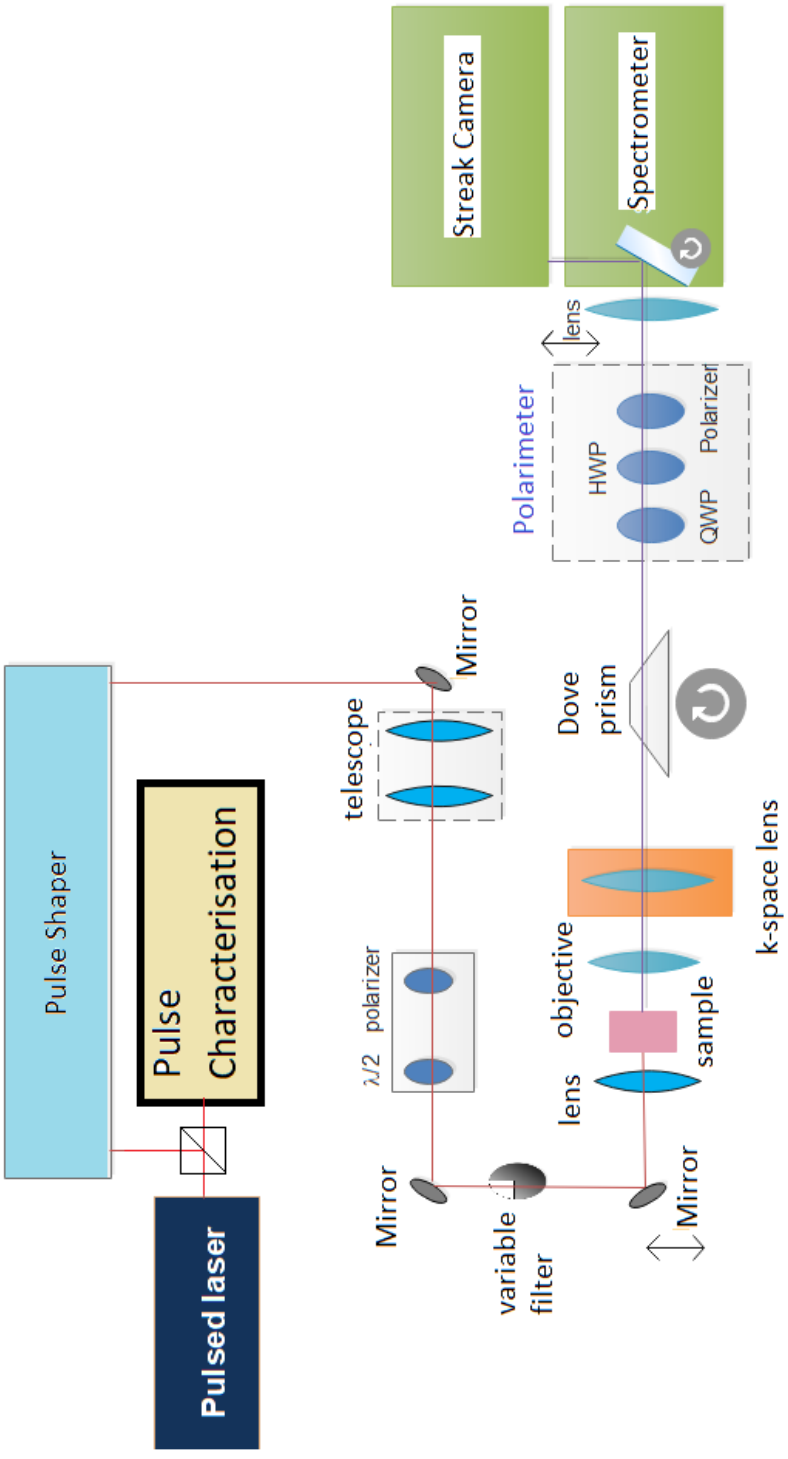

Figure 3.7: Optical setup used for experiments with microwires. The sample is excited from the back and the emission is collected by the front. The double arrow symbol, next to one mirror and next to the imaging lens, means that these two elements were mounted in a translational stage.

3.2.4 Transmission configuration for experiments with microwires

All the experimental results presented in Chapters 5 and 6 used the microwire sample described in 3.1.2. The experiments were carried out using the setup showed in Fig. 3.7. The sample was excited through the substrate and emission coming from the top DBR was collected on the other side. This transmission configuration requires the sample to be polished on the excitation side and the emission (and the excitation) to be at a longer wavelength than the bandgap of the substrate which in our samples is GaAs ($\sim$ 1.52 eV, $\sim$ 818 nm, at 4 K), otherwise the emission would be absorbed by the substrate.

As showed in Fig 3.7 the sample was excited by a Ti:Sapphire pulsed laser (3.2.3), a telescope was used to control the beam spot size, and a combination of linear polarizer and half-waveplate was used to rotate the laser polarization. The excitation angle could be adjusted by a mirror on a stage just before the last lens on the excitation path. On the other side of the sample the collection path is the same as used for sample characterization (Fig. 3.5), a mirror inside the spectrometer can be rotated to send the emission to the streak camera for time resolved measurements or to a CCD for time integrated images.

3.2.5 Reflection configuration for waveguide experiments

For the experiments carried out in the polariton waveguide (Chapter 4), two lasers were focused on the sample, a pulsed laser, which is focused in the input grating of the waveguide, and a continuous-wave (CW) laser, which is focused in between the input and output grating.

The pulse from the Ti:Sapphire tunable laser passes through a pulse shaper and a characterization process, as explained in 3.2.3. Then a telescope is used to control the size of the beam and a beam splitter (BS1 on Fig. 3.8) mounted in a rotational stage allows us to adjust the incidence angle of the pulse.

A second Ti:Sapphire tunable laser (MBR-110 Coherent) operating in continuous wave was used to pump the exciton reservoir . For the CW excitation, a telescope formed by cylindrical lenses modifies the shape of the spot, elongating it horizontally. A mirror was used to adjust the position and angle of the elliptical spot on the sample (Fig. 3.8). The excitation power was controlled by the combination of a half-waveplate and a linear polarizer. The half-waveplate

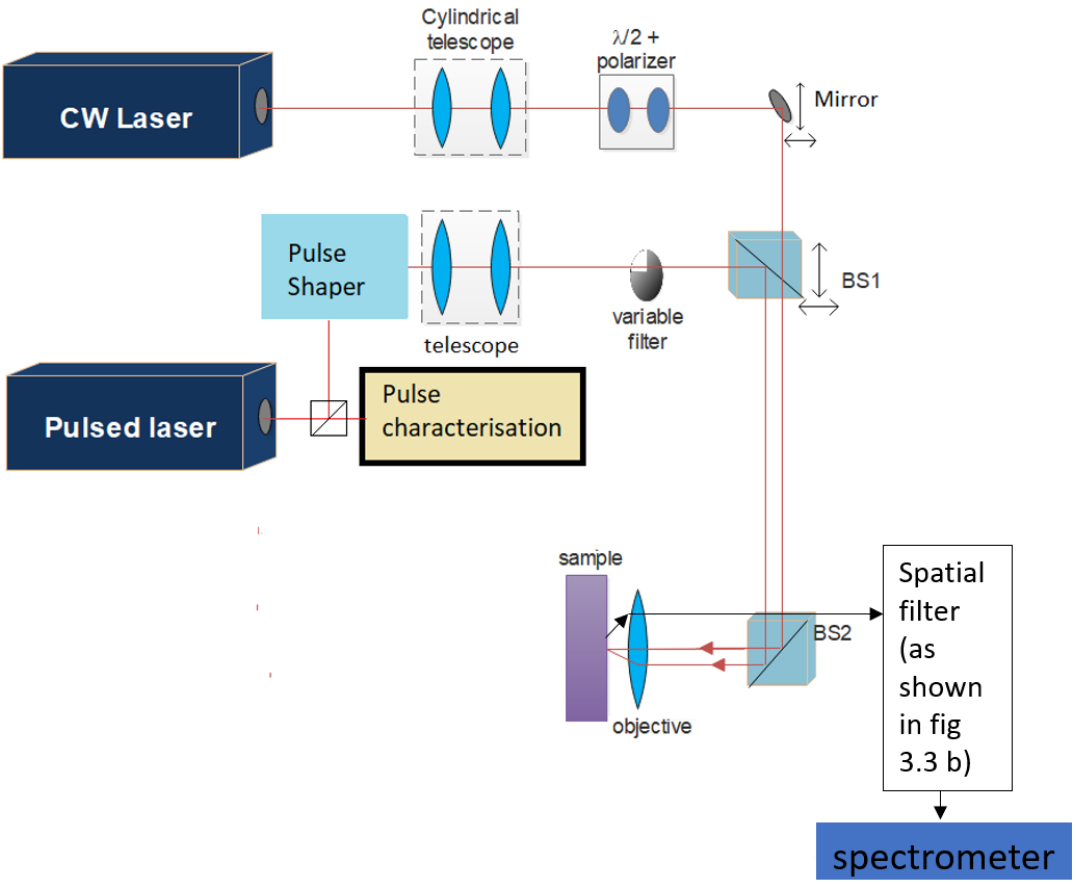

Figure 3.8: Optical setup used for experiments in a polariton waveguide. The sample is excited in a reflection configuration by combining a pulsed laser and a CW laser.

was mounted in a rotational stage wired to a Thorlabs motor, allowing us to automatically take hundreds of measurements by setting the power steps with a Python script on the computer.

3.3 Time resolved measurements

Time resolved measurements in real and k-space were taken to study the propagation of solitons and Cherenkov radiation in chapters 6 and 5.

All the time resolved measurements shown in this thesis were performed with the optical setup of Fig. 3.7 and the detector used was a Hamamatsu streak camera.

3.3.1 Streak camera

A streak camera is a device that uses the photoelectrical effect to measure ultra-fast light phenomena. It records intensity vs time vs position (or energy, depending of the optics used) with a 2 ps resolution for a time window of 120 ps.

Fig. 3.9 illustrates the operation principle of this device. The image shows 4 input pulses going through the entrance slit of the camera. After they have passed the slit, they are imaged on the photocathode, which is formed by a surface layered with different types of metallic film. Each pulse arriving to the photocathode, it is converted into a number of electrons proportional to the intensity of the incoming light. Then the electrons are accelerated and sent through a pair of sweep electrodes. The electrodes are swept by applying a high voltage time-synchronized with the incident light (the Ti:Sapphire pulsed laser), so that electrons that arrive at a different time are deflected in different angles in the vertical direction. Finally, the electrons impact a phosphor screen after they have been multiplied thousands of times by a micro-channel plate (MCP).

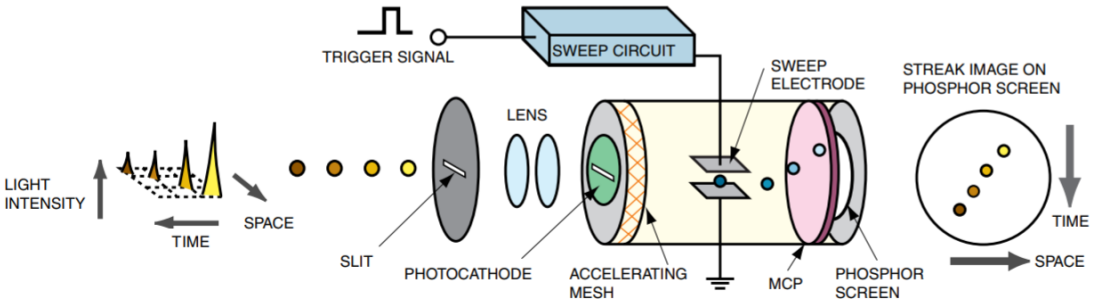

Figure 3.9: Principle of operation of the streak camera. Source: Hamamatsus Guide to Streak Cameras.

The final image on the phosphor screen is recorded with the CCD, its vertical axis corresponds to the time and the horizontal axis shows the horizontal position of the incident light. The brightness of the image is proportional to the intensity of the incident pulse.

The imaging lens in the optical setup (Fig. 3.7) can be used in order to get spatially long pictures, as required for the solitons observed in Chapter 6, which propagate for $\sim$500 μm. Although, an area of only $\sim$60 μm can be imaged by widening the spectrometer slit, the imaging lens, (which is positioned on a translational stage) can be moved sending different portions of the emission to the entrance of the streak camera at a time, so that the whole propagation path

can be reconstructed.

3.3.2 Time resolved k-space and dispersion measurements

The streak camera was also used to measure time resolved k-space and energy-momentum dispersion. As a streak camera picture shows intensity versus time, it was possible to record k-space images as a function of time, just by adding the k-space lens in the setup of Fig. 3.7.

However, plots of dispersion must be reconstructed from the raw, intensity vs time, streak camera pictures. In order to measure energy-momentum dispersion the vertical entrance slit of the spectrometer is set to 0.1 mm wide, so that a small range of k_x is selected. Then the emission is diffracted from the grating resulting in an image whose horizontal axis corresponds to energy and the vertical to k_y. If this is sent to the CCD a time integrated dispersion is recorded. But if it is send to the streak camera for time resolved measurements, then because of the horizontal entrance slit of the camera, only a small range of k_y is selected, resulting in a picture of energy vs time, as shown in Fig. 3.10

The imaging lens was mounted on a translational stage, wired to a Thorlabs motor. The lens could be moved to direct different k_x sections to the streak camera slit. Automatic scans were done by controlling the movement of the lens with a Python program, generating an array of energy vs time images for different k_x. From the array of streak camera pictures, it was possible to reconstruct time resolved energy vs k_x dispersions using Matlab. The k-space lens was set to measure at $k_y = 0$ for all the results showed in this thesis.

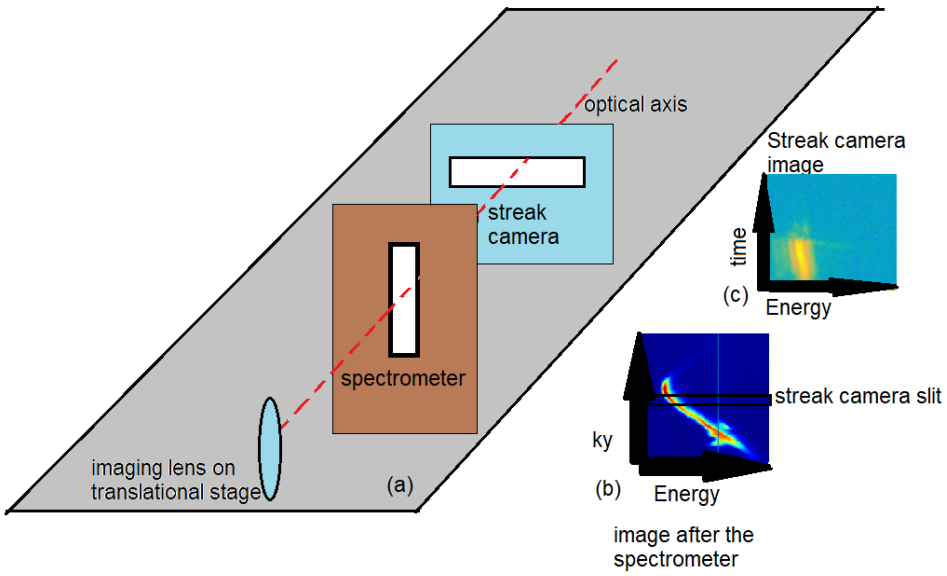

Figure 3.10: (a) Scheme showing the position of the spectrometer vertical entrance slit and the horizontal slit of the streak camera with respect to the optical axis. (b)An image of a dispersion measured after the slit of the spectrometer (k_y vs energy, integrated time). It has a rectangle illustrating the section going to the streak camera slit for time resolved measurements. (c) Measurement taken with the streak camera, showing time vs energy for a given k_x.

Chapter 4

Amplification of Nonlinear Polariton Pulses in Waveguides

In this Chapter I will present our results on the amplification of picosecond pulses propagating in a polariton waveguide. A summary of the results (including figures) presented here was already published in [179]. It is the result of an international collaborative effort. As mentioned in 3.1.1, the sample was grown by D. A Ritchie at the University of Cambridge and the waveguides were etched by B. Royall and I. Farrer from the University of Sheffield. All the experimental measurements and part of the theory presented in this chapter were carried out by me, under the supervision of P.M Walker, D.N. Krizhanovskii and M. S. Skolnick. Theory and simulations were developed by H. Sigurdsson, A. Yulin and I. A. Shelykh from the University of Iceland and ITMO University.

4.1 Introduction

As discussed in 2.8, polaritons have previously been used for optical amplification. Both, polariton lasers and final state stimulation have been demonstrated in microcavity systems [5, 74, 81]. Polariton waveguides have also been proposed for optical amplification [180] and an experimental demonstration using ZnO waveguides in the quasi CW regime was given in [181].

The use of polariton waveguides over microcavities is of particular interest for optical circuits. Several advantages can be pointed out, for instance, fabrication benefits from the fact that waveguide structures are simpler than microcavities,

making them easier to grow (2.4.5) and easier to pattern into photonic circuits. Secondly, waveguides also present some improvements regarding polariton properties, such as higher polariton propagation distances, higher velocities and higher nonlinearity. Additionally, in the context of amplification, an important advantage is that in waveguides direct optical pumping of the exciton states is possible because it is not spectrally blocked by DBRs.

Previously, solitons have been studied in waveguides (see 2.12.4), however measured losses were always high (loss length $\approx 400 - 800\mu m$). The main aim of this chapter is to understand the introduction of gain into the system.

In this chapter, the amplification process in a polariton waveguide is discussed in detail and the first experimental observation of amplification of picosecond pulses in a polariton waveguide is presented.

Optical amplifiers were introduced in the 1990s and quickly attracted the attention of the scientific community because of their possible uses in optical communication systems [182]. Since then, optical amplifiers have been mainly used as optical repeaters in long distance fibre optical systems. They are devices that amplify an optical signal without having to convert it to an electrical signal first. There are many kinds of optical amplifiers, including Raman amplifiers, doped fibre amplifiers and semiconductor optical amplifiers (SOAs). In SOAs a semiconductor provides the gain medium. SOAs use stimulated emission to amplify the light. The working principle is the same as a semiconductor laser but without the feedback. Light travels through the active medium and makes the electrically excited electrons to relax in the form of photons. These stimulated photons have some same properties than the original input light (such as same wavelenght, polarization and k vector), meaning an amplification of the signal.

There are some key advantages of using a polariton system over a regular SOA. When compared with traditional semiconductor optical amplifiers (SOAs), polariton devices may operate at lower electron-hole densities since polaritons only exist at lower densities than the Mott density (see 2.5.1). In contrast, SOAs amplify the light through stimulated emission, meaning that they need a high-density inverted carrier population to provide gain. Self-phase modulation (SPM) has been observed in SOAs, and in [183] it was identified as the main reason of pulse distortion and spectral broadening in semiconductor laser amplifiers. SOAs can provide high gain but the nonlinear response, producing the SPM, is a result of gain saturation [183].

The speed of the nonlinear response is faster for polariton systems. In SOAs the speed is usually more than 10 ps, because it depends of the gain-recovery time (linked to carrier lifetime) [183]. On the other hand, the polariton nonlinearity

operates on a picosecond timescale, an order of magnitude faster [164].

Another reason for the growing interest in the use of polariton waveguides comes from the possibility of applications exploiting non-hermitian (or broken parity-time symmetry) photonics [184,185]. It is believed that the study of Parity-Time (PT) symmetric photonic systems would be of use to develop all-optical devices with increased energy efficiency and speed on an optical chip.

In general, a Hamiltonian is PT symmetric ($PT\hat{H} = \hat{H}PT$) if it has the same eigenfunctions as the PT operator. Opposite to that, in a broken PT symmetry, $\hat{H}$ and PT would have different eigenvectors, even though $PT\hat{H} = \hat{H}PT$ would still be valid [186]. In optics, the propagation of light can be described by an effective Hamiltonian and the variation of the medium refractive index by the potential U(x). When the optical energy is conserved and U(x) is real, the Hamiltonian is Hermitian. In contrast, losses or gain in optical structures correspond to complex U(x) and non-conservative non-Hermitian operators. When this operator possesses PT-symmetry and has a real spectrum, the amplitudes of optical modes are conserved, corresponding to a compensation between gain and loss. This means that in PT systems losses become as important as gain, and when nonlinearity is involved effects such as the nonlinearly-induced PT-symmetry breaking, and all-optical switching are observed [184].

Achieving a balance between gain and losses in polariton waveguides would allow creation of complex spatially modulated gain-loss profiles opening the possibility to study phenomena such as broken Parity-Time symmetry and potentially lead to devices such as low power all-optical switches, unidirectional optical valves, lossless soliton propagation [184] and enhanced sensors [187].

In the following sections, our results of pulse amplification in polariton waveguides are presented. They show how polariton waveguides can provide gain and strong nonlinear response at the same time and at submillimetre length scales, which makes them a convenient system for integration of devices on a chip.

4.2 Description of the experiment

We utilised the GaAs waveguide described in section 3.1.1 and worked with two grating couplers separated by 400 μm. Using the reflection configuration shown in 3.2.5, 2 ps laser pulses (probe pulses), with a repetition rate of 80 MHz, were focused onto the input coupler. Light was collected after it had propagated into the output grating coupler (Figure 4.1).

The size of the pulsed laser spot at the input was 4.3 μm in the x direction. After propagation, the measured width (at the output coupler) increased to 11.2 μm due to diffraction occurring in the waveguide.

A second laser was used to feed polaritons by pumping from the exciton reservoir. Therefore, the pump was a CW laser at the exciton wavelength (837 nm) normally incident on the region of the sample between the two couplers (figure 4.1). The spatial size of the pump laser was 30 μm in the x direction, around 7 times wider than the probe pulse. In the propagation direction the pump spot was elongated to 100 μm and had its peak 120 μm away from the input grating coupler. The CW laser directly pumps only the exciton states close to zero in-plane momentum and not the high momentum polariton modes (fig 4.2) because it is focused on a region of the sample without a grating coupler.

Only the emission from the output grating was collected (with the use of a spatial filter implemented as explained in section 3.2.5). Finally, the light was recorded with a CCD camera in the spectrometer and resolved in real space and wavelength.

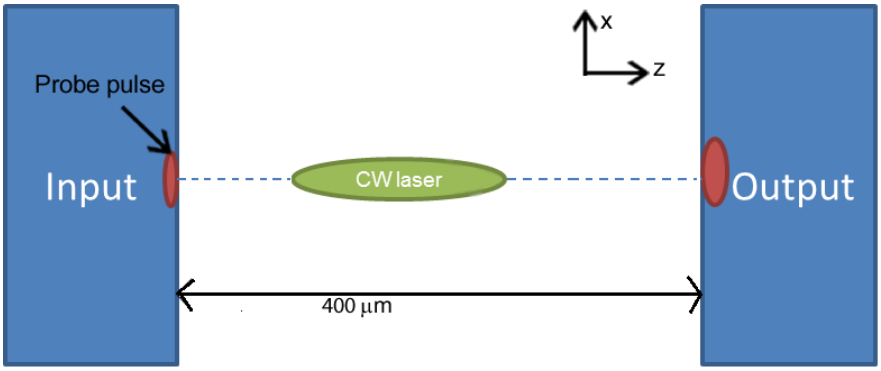

Figure 4.1: Scheme of the amplification experiment. Top-down schematic of the sample surface showing the input and output grating in blue. A pulsed probe laser is focused on the input coupler and propagates 400 μm to the output. Measurements were taken at the output coupler with and without a CW pump laser (with a spot 100 μm long) going in between the gratings.

Measurements were taken for 3 different pulse powers (average pump power incident on the sample): 5.77 $\mu W, 57.7 \mu W$ and 0.577 mW, and 3 detunings from the exciton: -6.3, -5.6 and -4.5 meV for a range of pump powers from 0 to 50 mW. Considering the repetition rate of the pulses (80 MHz), the pulse energies used correspond to: 72 fJ, 720 fJ and 7.2 pJ.

In order to measure the gain (optical amplification) produced by the use of

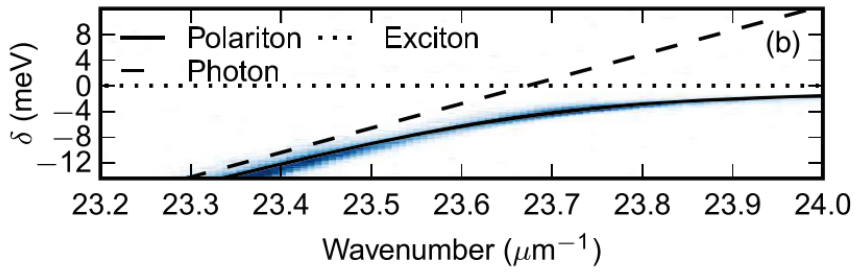

Figure 4.2: Lower polariton dispersion relation measured by Walker et al. on the GaAs planar waveguide, source: [169]

the pump laser, measurements were recorded at the output grating for the case when only the probe pulse is present (figure 4.3a), when the probe pulse is off but the pump laser is on (figure 4.3 b) and when both the probe pulse and the pump are switched on (figure 4.3 c). Spectra were obtained by integrating the recorded CCD images (figure 4.3 d-f).

Even though all the measurements were taken on the output grating coupler and the pump beam is not propagating directly from the input to the output (fig 4.1), we were able to measure spectra for the case when only the pump beam is switched on (S_{CW} spectrum, figure 4.3b,e). S_{CW} is generated in the following way. The pump excites exciton states near zero in-plane momentum. These excitons then relax through multiple scatterings, creating an incoherent reservoir which contains excitons and high momentum polaritons. The generated polaritons propagate in all directions, including z (fig. 4.1). Those that propagate in the z direction travel from the peak of the pump beam to the output grating ($\approx 280\mu m$) where they are diffracted out and collected giving us the measured S_{CW} spectrum (figure 4.3 b, e).

4.3 Results

4.3.1 Experimental Results

Measurements with the aim to investigate the produced gain due to pumping of the exciton reservoir were made. To obtain the spectrum of the amplified pulse (S_A), produced by effects of the pump, we subtract the CW spectrum (S_{CW}) from the one of the transmitted pulses (S_{tot}). The gain is given by the integrated intensity of S_A normalised to that of the unamplified pulse S_p.

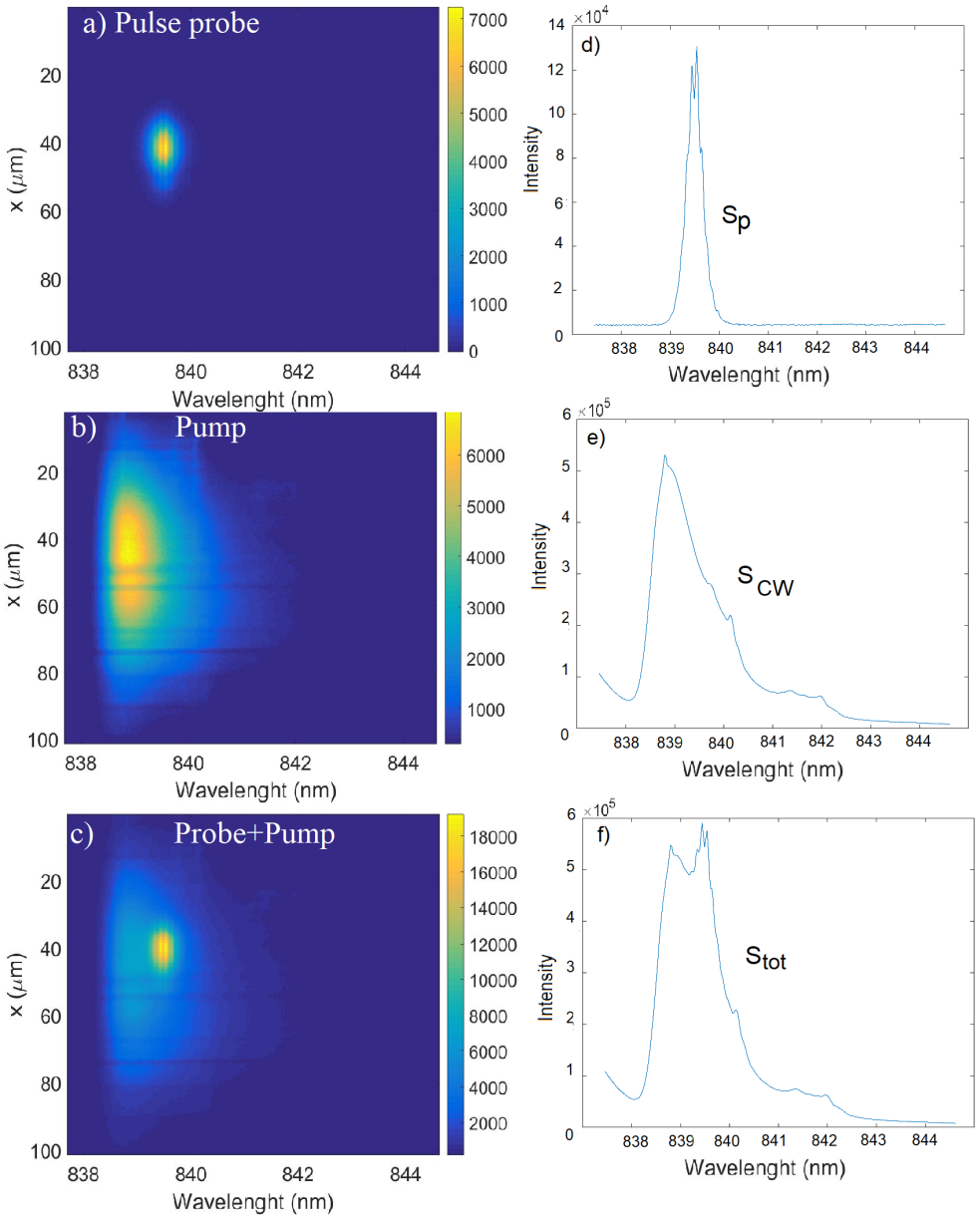

Figure 4.3: Measurement done with average pulse power of 5.77 μW, a probe detuning of -4.5 meV and pump power of 29 mW. Images taken at the output grating coupler (right) with the respective integrated spectra (left). For the following cases: (a,d) with the probe pulse laser switched on and the pump laser off, (b,e) pump laser on and probe pulse off and (c,f) both pump and probe on.

The figure 4.4 shows the case for the maximum CW pump power (50 mW) and minimum probe pulse power (5.77 μW) used for a probe detuning of -4.5 meV, and hence represents the lowest signal to background ratio in our experiments. The

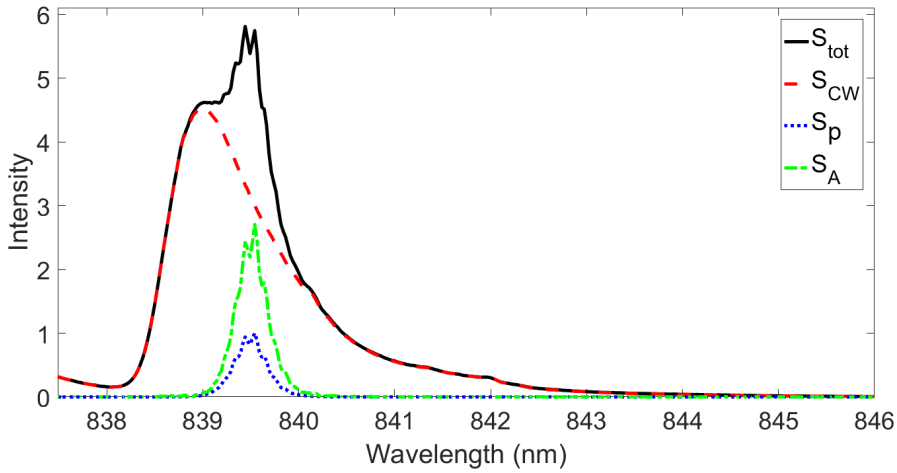

Figure 4.4: Collected spectra the maximum pump (50 mW) and minimum probe (5.77 μW) powers. S_p, S_{CW} and S_{tot} are the spectra obtained when, respectively, the probe pulse is switched on, the CW pump is switched on and when both are switched on. S_A results of the subtraction $S_{tot} - S_{CW}$. Probe detuning of -4.5 meV [179].

fluctuation in the CW signal (the difference between S_{CW} and S_{tot} at wavelengths away from the pulse) is invisible and the pulse is still 33% of the background, meaning that we can count on the accuracy of the subtraction.

The measured gain for the three different pulse energies and detunings is shown in figure 4.5. The error bars were calculated using the measured shot-to-shot fluctuations in the pump (S_{CW}) and the probe pulse (S_p) spectra. The gain expressed in dB showed in the table 4.1 is given by multiplying the logarithm of the intensity of S_A/S_p (fig 4.5) by 10. As shown in the figure, gain increases as the pump power increases and as the probe pulse power decreases. The maximum gain is then obtained for the minimum probe pulse energy (72 fJ) and the maximum pump power (50 mW), see table 4.1. This behaviour is explained by partial depletion of the reservoir, causing saturation of the gain ([18,188]). This was confirmed by the simulations showed in the subsections below, where the reservoir density n is depleted as the probe pulse passes through.

In addition, table 4.1 shows the linear loss corresponding to 100 μm, which is the pump spot length in the propagation direction [169].The highest linear loss corresponds to 0.97 dB for the smallest detuning (-4.5meV), it means that in the zero-pump case the pulses are expected to decay at worst to a level of $1/10^{0.097} = 0.8$ of their initial value over the length of the pump spot. For 72 fJ and 720 fJ probe pulses, the gain is big enough to compensate this loss. For

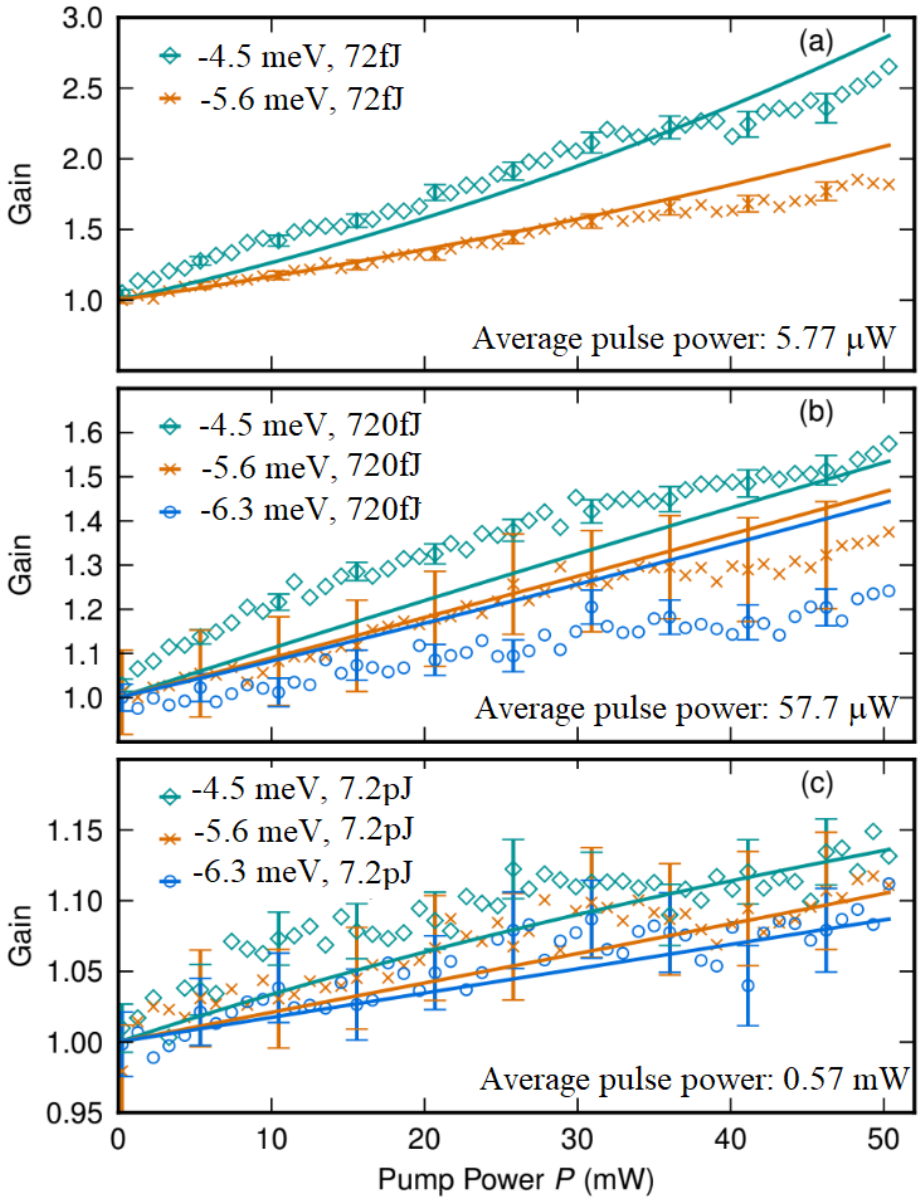

Figure 4.5: The measured gain experienced by the probe pulses with different pulse energies and detunings as a function of the pump power. Experimental data are shown as points and results of numerical simulation are shown as solid lines. For clarity only the error bars for every fifth point are plotted. Panels (a), (b) and (c) show data for probe pulse energies of 72 fJ, 720 fJ and 7.2 pJ respectively [179].

the highest probe pulse energy (7.2 pJ) the gain is still present but is not large enough to compensate all the losses. For this high power an additional nonlinear loss appears, as it will be discussed in 4.3.4, due to nonlinear processes scattering polaritons into a high absorption spectral region close to the exciton line.

Table 4.1: Gain at the maximum pump power for different probe parameters [179].

	Probe detuning		
	-4.5meV	-5.6meV	-6.3meV
Max. Gain (dB) (72 fJ)	4.3	2.7	-
Max. Gain (dB) (720 fJ)	1.96	1.37	0.93
Max. Gain (dB) (7.2 pJ)	0.57	0.45	0.37
Loss over 100 μm (dB)	0.97	0.90	0.86

**Due to some technical difficulties (laser instability) we were not able to obtain measurements with a probe pulse of 72 fJ and a detuning of -6.3 meV.

4.3.2 Theoretical Model

The gain showed in Figure 4.5 and summarized in table 4.1 is provided by stimulated scattering from the reservoir [18,189] where two near-zero momentum excitons scatter into high momentum polaritons; one in the lower and one in the upper polariton branch. Polaritons in the upper branch have very large propagation losses, mainly due to the exciton absorption [15, 45] and so cannot be observed.

The model developed by Helgi Sigurdsson, Alexey V. Yulin and Ivan A. Shelykh to explain this amplification process used a generalised Gross-Pitaevskii (or Nonlinear Schrödinger) equation of motion, describing the coherent field of the lower-branch polaritons (ψ) and a rate equation for the reservoir (n):

$$i\dot{\psi} = [\varepsilon - i\frac{\gamma}{2} + (g + i\frac{R}{2})n + \alpha|\psi|^2]\psi + F \tag{4.1}$$

$$\dot{n} = -(\Gamma + R|\psi|^2)n + P \tag{4.2}$$

Where ε is the dispersion of the LPB, γ and Γ are the polariton and reservoir inverse lifetimes, α is the polariton-polariton interaction strength, R is the reservoir gain, g is the polariton-reservoir interaction strength, F is the coherent probe pulse and P is the non-resonant pump.

The polariton energy-momentum dispersion was calculated from the strongly coupled exciton resonance (ε_X) and the waveguide photon dispersion (ε_P), see 2.5:

$$\hat{\varepsilon} = \frac{\hat{\varepsilon_X} + \hat{\varepsilon_P}}{2} - \frac{\sqrt{(\hat{\varepsilon_P} - \hat{\varepsilon_X})^2 + \Omega^2}}{2} \tag{4.3}$$

Here, the caret ($\hat{}$) is used for reciprocal space operators and Ω is the Rabi frequency. The exciton-photon resonance defines the zero energy and zero wavevector position, and the heavy mass of the excitons allows us to write $\hat{\varepsilon_X} \approx 0$.

Considering the photon field envelope $A = exp^{i(q_p z - \varepsilon_P t)}$ varying slowly compared to the exciton frequency ω_e [169] (here ε_p is the photon frequency and q_p is the photon wavenumber). We applied the slowly-varying-envelope approximation to the waveguide photon mode which results in the following approximation of the wave equation:

$$q_p \frac{\partial A}{\partial z} + \frac{\varepsilon_P}{v_g^2} \frac{\partial A}{\partial t} = 0 \tag{4.4}$$

Giving us the photon dispersion relation: $\varepsilon_P = -iv_g\partial_z$, where v_g is the group velocity of the light. The pulse and the pump are described by:

$$F = F_0 e^{-i(\omega_p t - k_p z) - t^2/2\sigma_t^2 - z^2/2\sigma_z^2} \tag{4.5}$$

$$P = P_0 e^{-(z-z_0)^6/2\sigma_{CW}^6} \tag{4.6}$$

Where $z_0 = 120\mu m$ is the distance from the input grating to the peak intensity of the pump. The 2 ps duration of the pulse determines a $\sigma_t = 0.85ps$ as $FWHM = 2ps = 2\sigma\sqrt{2\ln 2}$. In the same way $\sigma_z = 1.8\mu m$ was calculated from the measured size of the pulse beam which was $4.3 \pm 0.01\mu m$ (measured at the input grating). For the pump $\sigma_{CW} = 47\mu m$ so that the FWHM is the measured $100\mu m$.

Parameters of Eq 4.1 and 4.2 depend on the photon and exciton fraction of the polariton, which is determined by the pulse detuning creating polaritons at a certain energy. The three pulse detunings $\hbar\omega_p = \delta_0 = -4.5, -5.6, -6.3$ meV correspond to $\Delta = E_{ph} - E_x = 0, -1.99, -3.12$ which were used to calculate

the Hopfield coefficients (see section 2.5). Therefore, the Hopfield exciton fraction used was: $|C_x|^2 = 0.500, 0.392, 0.336$ for each detuning, each one having its corresponding photon fraction of $C_{ph} = 1 - |C_x|^2$.

The effective parameter values used [190] were: the effective polariton lifetime defined as $\gamma = \gamma_e|C_x|^2 + \gamma_p|C_p h|^2$ where γ_e and γ_p are the exciton and photon lifetimes respectively; the polariton-polariton interaction strength: $\alpha = \alpha_0|X|^4$; the polariton-reservoir interaction strength: $g = 4\alpha_0|X|^2$ and the reservoir gain: $R = R_0|X|^2$. Fixed parameters of the model were taken from [169]: $\hbar\Omega = 9meV$, $v_g = 58\mu mps^{-1}$, $\gamma_p = 0.1ps^{-1}$, $\gamma_e = 0.04ps^{-1}$ and $\alpha_0 = 3\mu eV\mu m^2$. Values: $\Gamma = 0.1ps^{-1}$, and $R_0 = 8\mu eV\mu m^2$ were chosen to fit the experiment.

We applied damped boundary conditions both in real space and in reciprocal space. In real space we used: $z < -50\mu m$ *and* $z > 400\mu m$ to simulate the polaritons exiting the waveguide after traveling from the input grating. In reciprocal space limits were chosen: $|k| > 1\mu m^{-1}$ to reproduce the higher losses for momenta far from resonance.

The results of numerically integrating equations 4.1 and 4.2 are shown as solid lines in fig. 4.5. The simulations semi-quantitatively reproduce the main features our experimental results, they show a gain that increases close to linearly with pump power and that decreases as the pulse detuning from the exciton, δ_0, increases.

Individual features of the simulated spectra of the coherent polariton field are examined directly in 4.3.4.

4.3.3 Discussion on the integrated gain

As shown in figure 4.5 the gain increases close to linearly with pump power for probe pulses with detuning δ_0 of -5.6 meV and -6.3 meV. One might expect the gain to increase super-linearly with pump since the pulse grows exponentially with the stimulated scattering rate [18, 189]. However, the depletion of the reservoir causes the pulse at the output to grow more slowly with density, explaining the linear growth observed.

Notably, the simulation significantly underestimates the dependence on δ_0 even though all parameters were adjusted to account for the varying Hopfield coefficients. This suggests that there is an additional dependence of the gain on the pulse detuning. In addition, the exciton broadening occurring at high pump power is another factor affecting the considered detuning.

For pulses detuned closer to the exciton at $\delta_0 = -4.5meV$, the effect of the exciton broadening should be more significant. It can be seen that for this detuning, the output vs input is sub-linear. This sub-linearity is more pronounced for the strong pulses of 720 fJ in panel (b) and of 7.2 pJ in panel (c) than for the weaker pulse in panel (a) (figure 4.5). Remarkably, the simulations did not show this sub-linearity. We note that in these samples there is a band of strong linear absorption related to the inhomogeneously broadened exciton line which begins above -3.8 meV [169]. The exciton broadening at high pump powers would increase optical absorption in the pump spatial region. It may also reduce the exciton density available in the spectral region close to the pulse and so enhance the depletion effect. This can explain why the sub-linearity is not present for the pulse detuned further from the exciton and why it is more pronounced for the higher power probe pulse, for which depletion has a bigger effect. The exciton broadening, probably together with some density-dependent or thermal effect produces a similar effect when measuring the spectra of the CW pump alone (S_{CW}), in Fig 4.6, we observe how the overall intensity becomes sublinear at powers ~ 25 mW.

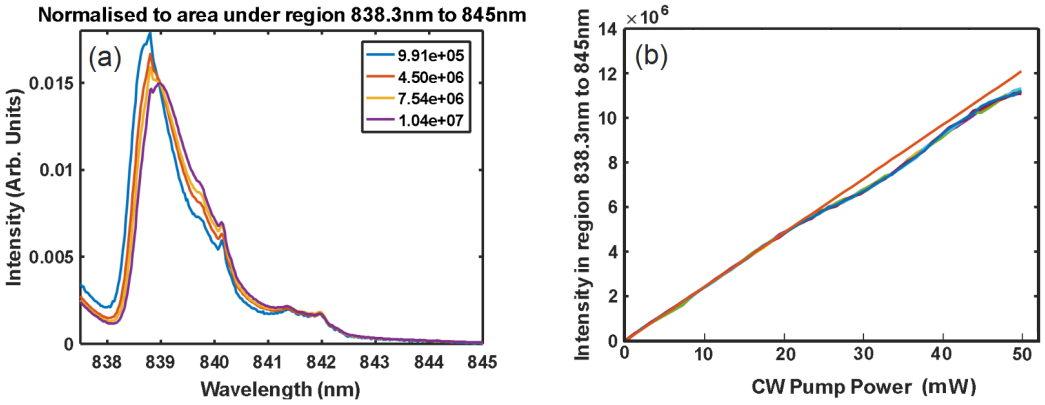

Figure 4.6: (a) CW spectra at different powers (from 0 to 50 mW) and (b) evolution of their peak intensity

4.3.4 Effect of the gain on the nonlinear processes

In this section we will discuss the effect of the gain on the nonlinear processes in the waveguide. The most remarkable nonlinear effect observed happens on the high energy propagated pulses (7.2 pJ) and it is self-phase-modulation (SPM). SPM occurs both in the temporal and the spatial (transversal) coordinates.

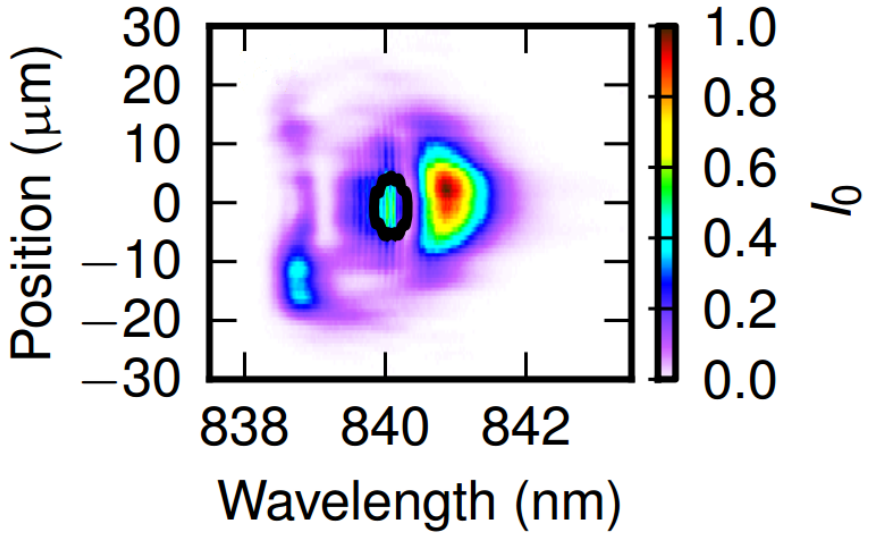

Figure 4.7: Output spectrum I_0 at zero pump for pulse of $\delta_0 = -5.6\ meV$ and incident average beam power of 0.57 mW (energy of 7.2 pJ). The solid black curve indicates the half-maximum contour of the input pulse spectrum (before propagation). [179]

The output spectrum $I_0(x, \lambda)$ of a 7.2 pJ pulse with a detuning of $\delta_0 = -5.6meV$ (and zero pump) is shown in figure 4.7. The black line in the figure indicates the half maximum contour of the pulse at the input, the spectrum at the output (after the propagation inside the waveguide) is shown in colour and is significantly broader. At this power, an intensity-dependent phase is accumulated as the pulse propagates which, through the intensity profile of the pulse, is a function of the transverse spatial coordinate x and of time (see 2.11.3). This varying phase leads to the complicated space-time spectral broadening observed in the figure 4.7.

The effect of the gain in the pulse spectrum is shown in figure 4.8. The figure shows the difference between the spectrum of a 7.2 pJ pulse with the highest amplification (maximum pump power applied: 50 mW) and the spectrum of the pulse without gain (at zero pump). The shape of the spectrum is notably changed by the presence of the gain. Some spectral components are strongly amplified (red) by up to 50% of the peak of I_0 while others are strongly de-amplified (blue) and some points where there is no intensity in the initial spectrum I_0 became populated with polaritons. This transformation of the pulse spectrum results from the combined effects of the gain and the SPM. The gain modifies the intensity profile of the pulse leading to a different nonlinear-optical phase whilst the SPM gives an intensity dependent spectrum.

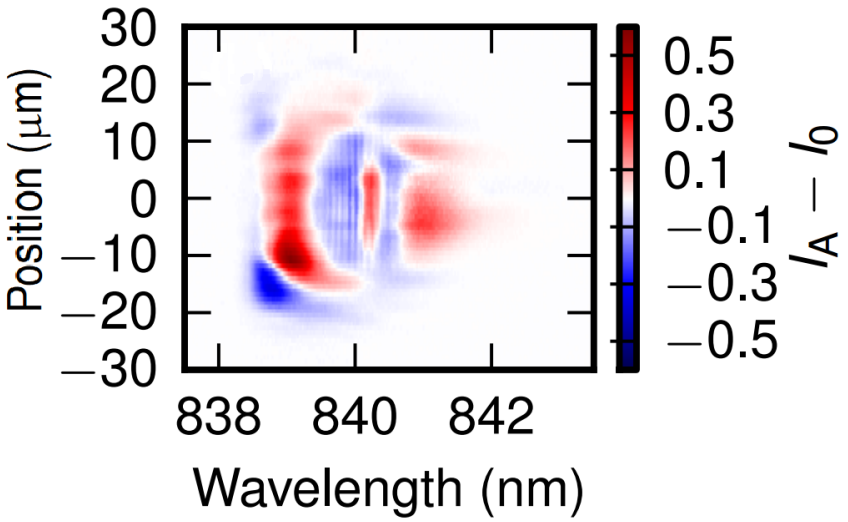

Figure 4.8: Difference between amplified spectrum I_A (with a pump power of 50 mW) and the spectrum with zero gain I_0 of a probe pulse with detuning $\delta_0 = -5.6\ meV$ and average pulse power of 0.57 mW (energy 7.2 pJ) [179].

The spectrum of the amplified pulse for each of the 3 measured detunings and highest pump power is showed in figure 4.9 panels (a), (b) and (c). The results are similar in all the cases, with some spectral components amplified and some de-amplified modifying the final spectrum of the pulse (S_A) when compared with the case of zero gain (S_p).

Even though the effect of the gain on the nonlinear response is most dramatic for the highest energy probe pulses due to the strongest self-phase modulation, it is also present in lower energy pulses.

Figure 4.10 shows the effect of the gain in the pulses with medium energy (720 fJ) and detuning $\delta_0 = -4.5$, -5.6 and -6.3 meV. The combination of gain and nonlinear effects is still observable. In a similar way that in SOAs , where pulses with a pulsewidth shorter than the carrier lifetimes exhibit a redshift [183], here the amplified pulse also undergoes an increase in wavelength. A fitting of the lines with a $sech^2$ lineshape (see 2.11.3) exhibited spectral shifts of: $160 \pm 20\mu eV$ for a detuning $\delta_0 = -4.5meV$, $150 \pm 20\mu eV$ for $\delta_0 = -5.6meV$ and $80 \pm 20\mu eV$ for $\delta_0 = -6.3meV$.

In both figures (4.9 and 4.10) panel (d) shows the simulated spectra corresponding to the experimental case showed in panel (b) with a pulse detuning of -5.6 meV and highest gain. The simulated spectra were obtained by numerically integrating Eq. 4.1 and Eq. 4.2 discussed in 4.3.2.

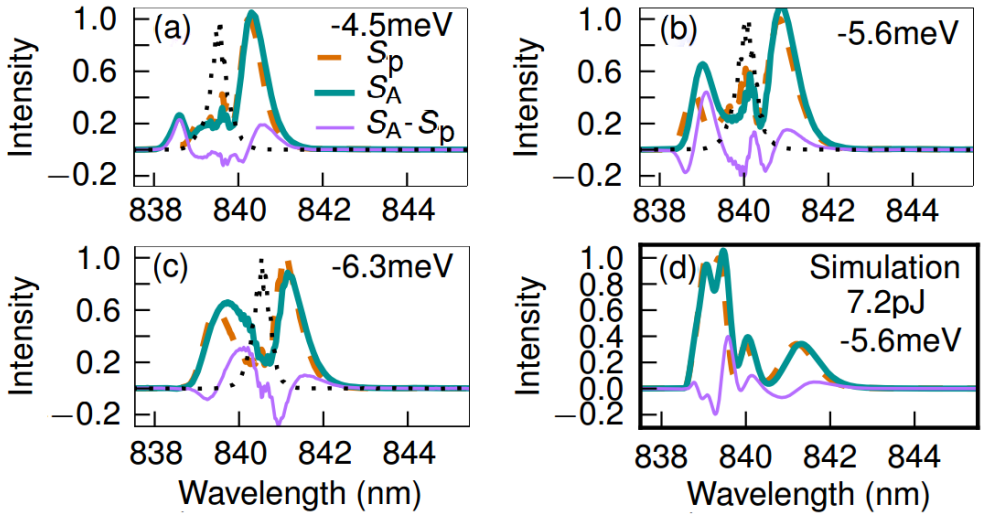

Figure 4.9: Nonlinear response combined with gain for 7.2 pJ probe pulses. (a-c) Integrals over the x direction of the amplified pulses spectra S_A (at the highest pump power) and spectra of the pulses with zero gain S_p for three different initial pulse detunings δ_0. (d) Simulation of panel (b). The black dotted curve shows the spectrum of the input pulse. All curves are normalized to the peak of the zero-pump spectrum S_p.(b and d published in [179])

The simulation of the spectra for the medium energy pulses (4.10 panel d) reproduced quantitively the results obtained experimentally. However, the simulation of the spectra for the high energy pulses (4.9) reproduced the broadening of the initially narrow pulse S_p but with significant differences in the total spectral shape. These differences between experiment and theory may arise from the one-dimensional nature of the simulations.

Simulations were performed in one dimension (z), meaning that they neglected that the pulse envelope in the x direction is free to evolve. This simplification works well for the cases of low pulse energy (72 fJ and 720 fJ) because the nonlinear defocussing is weak, giving us a good agreement between the experimental and simulated spectra (fig 4.10). The one dimension simplification breaks down for highest probe pulse energies (7.2 pJ), where the nonlinear defocussing is expected to be bigger. This may be the reason why the simulation does not reproduce the exact shape of the experimental spectrum in 4.9, even though the overall spectral broadening is accurate.

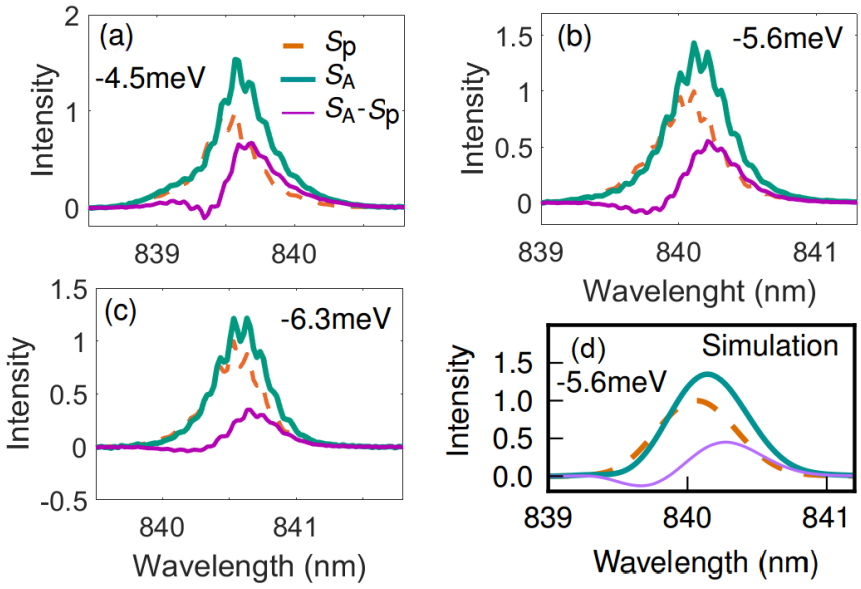

Figure 4.10: Nonlinear response combined with gain for 720 fJ probe pulses. (a-c) Integrals over the x direction of the amplified pulses spectra S_A (at the highest pump power) and spectra of the pulses with zero gain S_p for three different initial pulse detunings δ_0. (d) Simulation of panel (b). All curves are normalized to the peak of the zero-pump spectrum S_p.(b and f published in [179]).

4.4 Conclusions

We have shown amplification of high velocity propagating picosecond polariton pulses with enough gain to overcome losses. We have investigated the effect of probe pulse detuning and power and find a saturation of the gain for higher initial pulse powers. With these results and the corresponding theoretical simulation, we were able to show that the gain is mainly limited by depletion of the reservoir.

Semi-quantitative agreement between the experimental results and simulations was achieved. From the simulations presented in 4.10 and 4.9 we have proved that the spectral broadening present in high energy propagated pulses results from the polariton interactions. In addition, the change in spectrum with gain observed experimentally was successfully reproduced by the numerical model, showing that its main source was the interplay of the gain and the interactions.

We experimentally got a maximum gain of 4.3 dB for the pulse with minimum energy (72 fJ) and minimum detuning ($\delta_0 = -4.5\ meV$). More than 4 times

greater than the linear loss over the pump spot length (0.97 dB). The system could be improved (for greater amplification) by increasing the overlap of the pulses with the gain. One way to do it would be using a $\approx 4\ \mu m$ ridge waveguide to confine the propagating polariton and the pump region in the transversal direction.

We observed combined gain and nonlinear modulation of the pulse spectra in the same device at the same time, with the spectrum depending on the level of CW pumping. These findings open up the possibility of new classes of nonlinear sub-millimetre waveguide devices exploiting non-hermitian propagation of pico-Joule pulses.

Chapter 5

Cherenkov radiation in microwires

The study of the propagation of picosecond pulses in microwires is reported in the following two chapters. In this chapter I present the first observation of Cherenkov radiation in polariton microwires as a result of the propagation of bright polariton solitons.

Understanding of the effects accompanying guiding of polaritons in microcavity wires (MCWs) is important for the current work pursuing development of polaritonic chip scale devices for classical and quantum information manipulation. Here I show a model of microwire polariton solitons and of their inherent Cherenkov radiation followed by a collection of experimental results where we measured polariton-soliton pulse compression, pulse breaking and emission of the backward Cherenkov radiation.

The interest in using microcavity wires in this and the following chapter comes from the practicality of the system for future applications in polaritonic circuits and, as it will be explained in sections 5.1 and 5.3, particular properties such as a long polariton lifetime and the shape of the LPB, which has finite energy at k=0, are essential for the formation of Cherenkov radiation and conservative solitons.

A summary of the results (including some of the figures) presented here was already published in [191]. The sample used is described in 3.1.2, it was designed by P. M. Walker, grown by E. Clarke and then etched by B. Royall from the University of Sheffield. All the experimental results and part of the theory presented in this chapter were carried out by me and J. K. Chana, under the supervision of M. Sich, D.N. Krizhanovskii and M. S. Skolnick. Theory and simulations were

developed by D.V. Skryabin, Y.V. Kartashov and O.A. Egorov from University of Bath and ITMO University (see [191] for the full list of academic affiliations).

5.1 Introduction to Cherenkov Radiation

Cherenkov radiation was observed for the first time in 1934, when Pavel Cherenkov under the supervision of Sergey Vavilov noticed a blue light around a radioactive preparation under water. This phenomenon is also known as Vavilov-Cherenkov radiation. In 1937, Igor Tamm and Ilya Frank developed the complete theory behind it. The Physics Nobel Prize was awarded to P. Cherenkov, I. Tamm and I. Frank in 1958.

Cherenkov radiation occurs when charged particles travel through a medium at a speed higher than the speed of light in that medium, producing a shock wave in the electromagnetic field. The most popular form of Cherenkov radiation is the blueish light around nuclear reactors (Fig 5.1) which is produced by the beta particles (fast electrons) emitted by nuclear fission. The charged particles excite the electrons of the water molecules, which then emit photons as they return to equilibrium, because the charged particles travel faster than light in the medium, the shock wave produces constructive interference that forms the blue glow. The amount of energy radiated in this process is given by the Frank-Tamm formula [192].

Forward Cherenkov radiation has had multiple applications in high energy physics, optics, cosmic rays and atmospheric sciences and it is used in particle detectors and accelerators [192].

Backward (reversed) Cherenkov radiation refers to the radiation emitted in the direction opposite to the one of the moving particles radiating it. In 1964 Veselago theoretically predicted that materials with a negative refractive index should present a backward Cherenkov radiation [194]. Recently, it was observed experimentally in a left handed (negative index) all-metal metamaterial [195].

In photonics, the Cherenkov radiation is emitted by a quasi-soliton pulse, instead of a charged particle like an electron. The equivalence comes from the fact that the radiation source is a wave packet (the soliton) with a phase velocity faster than the linear phase velocity of the medium [196].

Cherenkov radiation has been observed as an accompanying effect of solitons in optical fibers for more than 30 years [197]. In 1995, it was theoretically shown

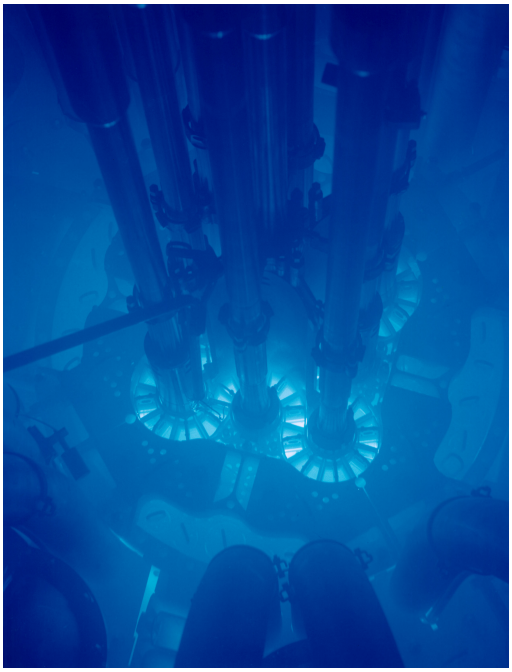

Figure 5.1: Cherenkov radiation glowing in an underwater nuclear reactor at the Idaho National Laboratory. Source: [193]

that the Cherenkov concept could be used for all processes in which solitons transfer power to linear waves [196]. More recently, Cherenkov radiation emitted by multiple solitons played an outstanding role in the generation of the supercontinuum in optical fibres [129, 130, 146]. Supercontinuum generation refers to the process where a narrow-band pulse experiences a several spectral broadening due to a collection of nonlinear effects. It has been shown that the effect of higher-order dispersion on the propagating solitons is necessary for the supercontinuum generation and that it is only when the initial emitted radiation has the chance to interact with the solitons (becoming the photonic Cherenkov radiation) that supercontinuum is achieved [129]. With the aim of understanding the details behind supercontinuum generation, in 2005, Efimov et al. studied the interaction between solitons and continuous waves; Figure 5.2 shows their observation of Cherenkov radiation in fiber optics.

Another important application occurs in microring resonators, where the formation of frequency combs is achieved by using the Cherenkov radiation emitted by solitons [199].

In this chapter, I present the first observation of backward Cherenkov radiation emitted by solitons. As it will be discussed in the following sections, the key

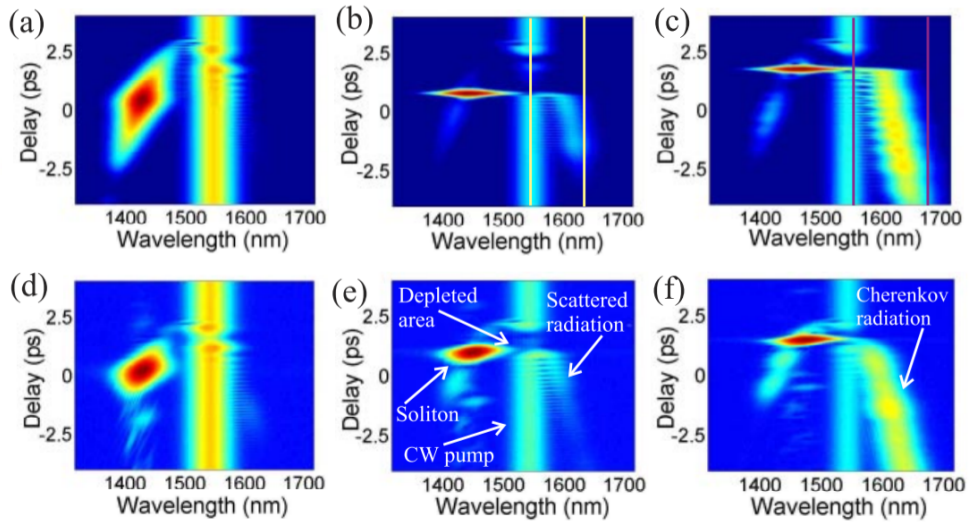

Figure 5.2: Cherenkov radiation observed in optical fibers as a result of the interaction between a soliton and a continuous wave. First row (a),(b),(c) numerical modeling, and second row (d),(e),(f) experimental measurements, showing XFROG diagrams resulting from the interaction between the continuous wave and the soliton. CW power is 100 mW and the propagation length is 0.90 m. Soliton peak power of (a,d) 1.7 kW, (b,e) 4.4 kW and (c,f) 7kW. Taken from [198].

feature allowing the backward Cherenkov radiation was the form of the dispersion in a microcavity polariton system.

Bright and dark solitons have been observed in polariton systems [19, 20, 54, 164, 169, 173], however Cherenkov radiation was never reported. One of the main issues obstructing the observation of Cherenkov radiation is that it requires polariton lifetimes long enough to allow propagation of polaritons over long distances and therefore of solitons without the pumping beam. Although bright dissipative polariton solitons have been studied in microcavities [19], the short polariton lifetimes make the use of a CW pump holding beam an essential requirement for losses compensation. However, the CW pump beam cannot support propagation of Cherenkov radiation since it only provides gain to soliton harmonics.

Here we decided to use a polariton microcavity wire (MCW) for observation of solitonic effects mainly because the vertical confinement [24, 26, 200, 201] reduces the power degradation due to defocusing in the transverse direction. In addition, a long 30 ps polariton lifetime was obtained thanks to the high quality DBRs in our sample. Because of these two reasons, our microwire proved to be a good sample to observe bright solitons without the use of the holding beam.

In addition, the strong nonlinearity characteristic of polariton systems [24, 164] represents an important advantage enhancing the intensity of the measured Cherenkov radiation.

5.2 Experimental Layout and sample characterization

We worked with the sample described in 3.1.2 which is a 1 mm long and 5 μm wide microwire. The characterization of the microwire was carried out using the setup described in 3.2.2. The obtained energy-momentum dispersions are showed in figure 5.3. We measured an exciton-photon detuning of $\simeq -2$ meV, a polariton lifetime of $\simeq 30$ ps and a polariton Rabi splitting $\hbar\Omega_R \simeq 4.5$ meV.

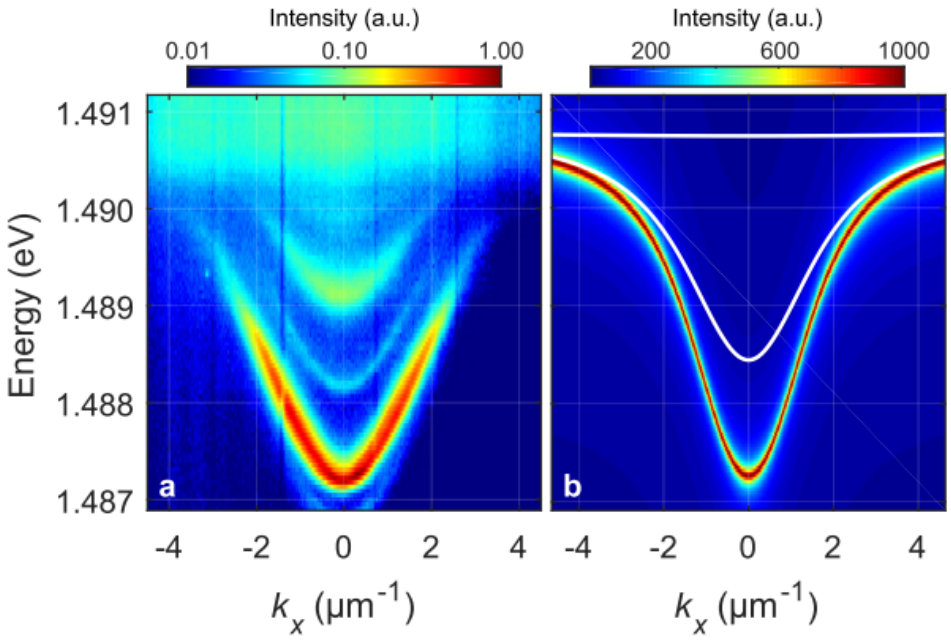

Figure 5.3: (a) Experimentally measured energy-momentum dispersion in the microwire. The brightest line corresponds to the ground state and the next line up to the first excited state. (b) Numerical simulation of the dispersion accounting for the 30 ps polariton lifetime. Continuous spectrum is located between the white lines [191].

The TE-TM splitting was also measured. As shown in figure 5.4, the TE-TM splitting changes with momentum (k_x), at $k_x = 0$ (panel a 5.4) it is close to 0

and at 2 μm^{-1} (panel c 5.4) it is about 20 - 30 μeV, which is in the limit of the spectrometer resolution of ~ 2 $\mathring{A}$.

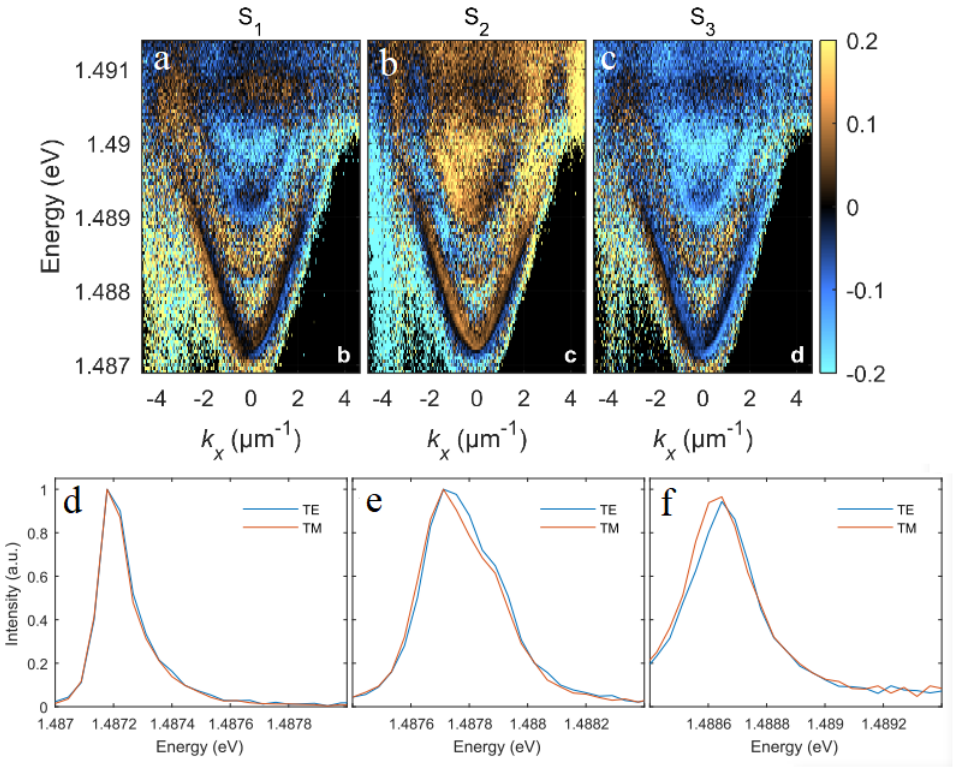

Figure 5.4: Microwire characterization: TE-TM energy splitting. (a-c) Measured dispersions at different polarization (linear, diagonal and circular). (d-f) TE and TM polarizations intensity vs energy at $k_y \simeq 0$ and for different values of k_x: (d) $k_x \simeq 0$, (e) $k_x \simeq 1\mu m^{-1}$, and (f) $k_x \simeq 2\mu m^{-1}$. (d-f) Published in [191].

In order to observe soliton formation, we worked in a transmission configuration with the setup described in 3.2.3, 3.2.4, and sent a TE-linearly polarized pulse beam quasi-resonantly to the microwire as showed in figure 5.5.

On the experiment we were able to vary the central wavelength, power and angle (along the x-axis) of the excitation beam, which is equivalent to the momentum k_x (in the following section 5.3, the parameter k is used instead of k_x, where $k = k_x L$). As I will show in the following sections, to achieve soliton formation we need to excite at high energy and momentum and these 2 parameters along with the excitation power determine the intensity, velocity and direction of the produced Cherenkov radiation.

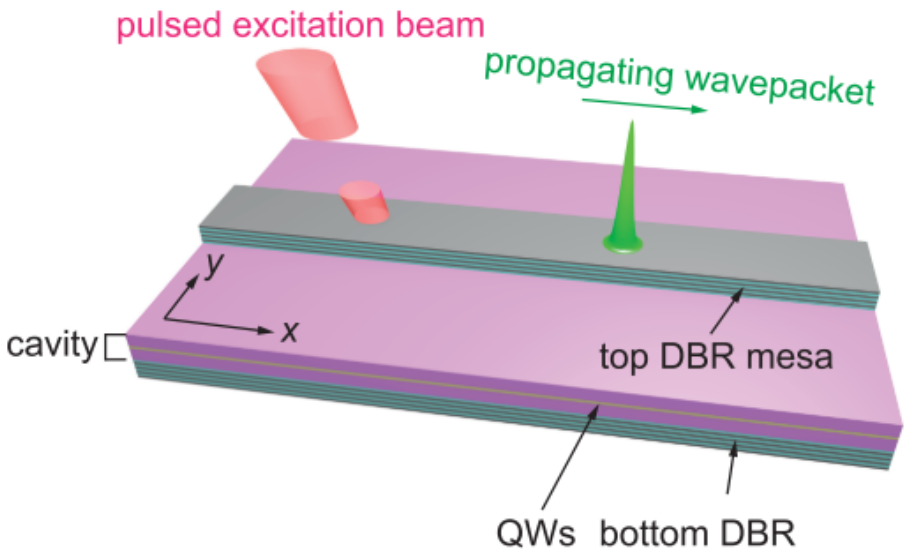

Figure 5.5: Excitation scheme. A 3D schematic view of the MCW. A pulsed laser (the excitation beam) is focused on the MCW at an angle along the x-axis to form the polariton wavepacket traveling in the x direction. Excitation energy, power and momentum where varied for the experiment to obtain polariton solitons and Cherenkov radiation [191].

5.3 Theoretical model of polariton Cherenkov radiation

As mentioned above, the theory and modelling of Cherenkov radiation in microwires were developed by D. V. Skryabin, Y. V. Kartashov and O. A. Egorov. This section summarizes their theory published in [191]. We present it before the experimental results with the aim to help the reader to understand the origin of the Cherenkov effect observed in the polariton system.

5.3.1 Model equations

The following dimensionless equations were developed to model the backward polariton Cherenkov radiation in microwires:

$$i\partial_t A_+ + (\partial_x^2 + \partial_y^2)A_+ + (i\gamma_c + \delta_c + \delta + U(y))A_+ = -\psi_+ + \varsigma(\partial_x - i\partial_y)^2 A_- \quad (5.1)$$

$$i\partial_t A_- + (\partial_x^2 + \partial_y^2)A_- + (i\gamma_c + \delta_c + \delta + U(y))A_- = -\psi_- + \varsigma(\partial_x - i\partial_y)^2 A_+ \quad (5.2)$$

$$i\partial_t \psi_+ + (i\gamma_e + \delta - |\psi_+|^2 - g|\psi_-|^2)\psi_+ = -A_+ \quad (5.3)$$

$$i\partial_t \psi_- + (i\gamma_e + \delta - |\psi_-|^2 - g|\psi_+|^2)\psi_- = -A_- \quad (5.4)$$

Here $A_\pm$ are the amplitudes of the σ_+ and σ_- polarized photonic modes coupled to the positive and negative spin-one coherent excitons $\psi_\pm$ in a microcavity [201]. The exciton-exciton interaction and the spin-orbit coupling effects between the photonic components (from the TE-TM photon energy splitting) were considered in the model. The photon γ_c and the exciton γ_e linewidth and detuning parameters δ_c and δ are normalised to the Rabi splitting of $\hbar\Omega_R = 4.5$ meV. For the polariton linewidth 0.1 meV, $\gamma_{c,e} = 0.02$. The parameters $\delta_c = -0.4$ and δ are dimensionless detunings of the cavity resonant frequency and of the pulse carrier frequency from the exciton resonance chosen by us as a reference.

Lateral confinement in the microwire is described by $U(y) = e^{-(2y/w)^8} - 1$ where w = 7 is the dimensionless wire width [201]. Spatial coordinates are normalised to the distance $L = \sqrt{\hbar/(2m_c\Omega_R)}$, where $m_c = 10^{-36}$ kg is the effective mass of the cavity photons.

The parameter g refers to the cross-spin exciton-exciton interaction which is weakly attractive, g=-0.05 [63].

ς characterises the spin-orbit coupling strength (the symbol ς is used instead of the β in [191] to avoid confusion with the propagation constant of waveguides used in the previous chapter). We measured a TE-TM energy splitting of 20-30 μeV (fig 5.4) which is well approximated by a $\varsigma = 0.02$. For the simulation of the energy vs momentum dispersion (Fig 5.3) of the MCW we set $A_\pm(x,y) = a_\pm(y,k)e^{ikx}$, $\psi_\pm(x,y) = \psi'_\pm(y,k)e^{ikx}$ where k is the momentum along the propagation direction. Then the resulting linear eigenvalue problem for $a_\pm(y,k)e^{ikx}$, $\psi'_\pm(y,k)e^{ikx}$ was solved numerically.

The energy spectrum of the lower polariton branch has a discrete part consisting of the two pairs of nearly degenerate TE and TM modes and a continuous part, which is located between the white lines in the figure 5.3. A pair of discrete energies corresponds to the even ground state and a second pair to the odd excited state. ς is the parameter responsible of the lifting of the degeneracy between the TE and TM modes within the pairs on the dispersion.

In the same way as that in a planar microcavity (2.5.3), the shape of the po-

lariton dispersion shows that the effective polariton mass ($m_{eff} = \hbar/(\Omega_R L^2 \partial_k^2 \varepsilon)$) changes its sign at some critical momentum. It means that the group velocity dispersion also changes its sign, from anomalous to normal, as discussed in 2.5.3, and hence a nonlinear self-focusing of polaritons can result from the repulsive exciton-exciton interaction.

5.3.2 Soliton solutions

To form a soliton from a polariton pulse, a balance between the pulse chirp induced by kinetic spreading and the chirp induced by polariton-polariton repulsion must be achieved (see 2.12.2). In order to do this, the polariton pulse prepared in the ground state (figure 5.6) needs to have a momentum high enough so that a large part of the pulse spectrum belongs to the negative mass range.

Our polariton model (Eqs 5.1-5.4), as many mathematical models, idealises the dispersion laws needed for soliton formation and disregards the dissipation always present in nature. For better understanding of the physics in our system, an approximated model with exact soliton solutions had to be developed. Several approximations were made to find the exact soliton solutions. We considered only one dimension: $\partial_y = 0$, and disregard $\partial_x^2 B_\pm$ and $\varsigma \partial_x B_\pm$ by assuming a narrow spectra of the pulses. We proceed by substituting

$$A_\pm = B_\pm(t,x)e^{ik_s x}, \psi_\pm = \phi_\pm(t,x)e^{ik_s x} \tag{5.5}$$

Where k_s is the soliton momentum, into Eqs 5.1 to 5.4. Resulting in:

$$\partial_t B_+ + i2k_s\partial_x B_+ + (\delta_c + \delta - k_s^2)B_+ = -\phi_+ - \varsigma k_s^2 B_- \tag{5.6}$$
$$\partial_t B_- + i2k_s\partial_x B_- + (\delta_c + \delta - k_s^2)B_- = -\phi_- - \varsigma k_s^2 B_+ \tag{5.7}$$
$$i\partial_t \phi_+ + (\delta - |\phi_+|^2 - g|\phi_-|^2)\phi_+ = -B_+ \tag{5.8}$$
$$i\partial_t \phi_- + (\delta - |\phi_-|^2 - g|\phi_+|^2)\phi_- = -B_- \tag{5.9}$$

Fig 5.6 shows (with dotted lines) the simulated dispersion of the ground state polariton modes using these equations.

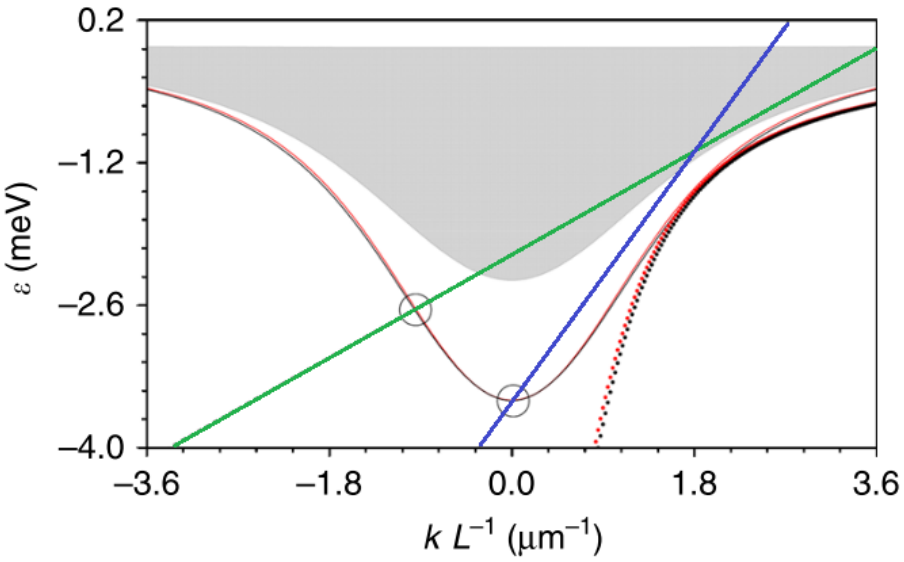

Figure 5.6: The lowest energy modes dispersion is shown with solid red (TE mode) and black (TM mode) lines: $\varepsilon = \hbar\omega_R\delta$ vs. polariton momentum kL^{-1}.The approximate dispersion giving the exact solitons is shown with the dotted lines. The TE-TM splitting is very small at the scale of the plot ($\approx 30\mu$eV, so that the red and black lines are very close. The grey shaded area represents continuous spectrum. Exact solitons dispersions are shown with straight lines and Cherenkov resonances with open circles. Blue line for a soliton centered at $\simeq 2\mu m^{-1}$ with $\delta = -0.35$, $k_s = 1.2$, $v = 0.366$ gives a Cherenkov resonance at zero and, green line for a soliton centered at $\simeq 2.4\mu m^{-1}$ and $\delta = -0.24$, $k_s = 1.5$, $v = 0.150$ results in a backwards Cherenkov radiation with resonance at $\simeq -0.9\mu m^{-1}$. The positions of the open circles representing Cherenkov resonances are given by the solutions of Eq. 5.14 [191].

The exact soliton solutions of the system are given by:

$$B_{\pm}(t,x) = b_{\pm}(\xi), \phi_{\pm}(t,x) = \varphi_{\pm}(\xi), \xi = x - vt \tag{5.10}$$

Where v is the group velocity. After solving numerically we got two families of linearly polarised solitons, TM-solitons when $b_+ = b_-$ and TE-solitons for $b_+ = -b_-$. To analyze the stability of the soliton families, equations 5.6-5.9 were linearised assuming that the solitons are perturbed by small-amplitude localised perturbations evolving in time as $e^{\lambda t}$, and solved the eigenvalue problem for the perturbations numerically. We found instability growth rates $\lambda\Omega_R$ of $\approx 1ps^{-1}$ for both families, however TM solitons are unstable in their entire existence domain

and can transform into a pair of quasi-solitons, while TE solitons are stable in the region before the $\sigma_\pm$ families split from them.

We decided to use the TE orientation in the experiments to reduce the complexity of the nonlinear dynamics.

5.3.3 Polariton Cherenkov radiation

The frequencies of the ground state modes in the microcavity wire are well approximated by:

$$\delta_{TE,TM} = -\frac{1}{2}(\delta_c - (1 \pm \varsigma)k^2) - \sqrt{\frac{1}{4}(\delta_c - (1 \pm \varsigma)k^2)^2 + 1} \tag{5.11}$$

where plus and minus signs correspond to the TE and TM modes, respectively. Eq. 5.11 is obtained from substituting the anzats containing the exact soliton solutions, $b_\pm$, $\varphi_\pm$ and the radiation field $\varepsilon_\pm, \alpha_\pm$:

$$A_\pm(t,x) = b_\pm(\xi)e^{ik_s x} + \varepsilon_\pm(\xi,t)e^{i\delta t} \tag{5.12}$$
$$\varphi_\pm(t,x) = \varphi_\pm(\xi)e^{ik_s x} + \alpha_\pm(\xi,t)e^{i\delta t} \tag{5.13}$$

into equation 5.1 with $\partial_y = 0 = \gamma_{c,e}$, and linearise around $\varepsilon_\pm, \alpha_\pm$ (see supplementary material of [191] for more details).

Soliton's dispersion is shown in figure 5.6, it is a straight line because a soliton is a wavepacket with suppressed group velocity dispersion. The soliton group velocity is given by the tilt of that line. A blue shift of the nonlinear polariton wave is produced by the repulsive nonlinearity, meaning that the soliton dispersion is shifted upwards from the linear spectrum. When the soliton dispersion intersects the energy spectrum of the linear polaritons (circles in fig 5.6) it produces a resonance momentum and the soliton is expected to emit dispersive waves with the spectrum centred at this momentum. Those waves are the Cherenkov radiation.

Hence, considering the soliton dispersion $\delta_+ v(k - k_s)$, which is a straight line, the Cherenkov resonance conditions are:

$$\delta + v(k - k_s) = \delta_{TE,TM} \tag{5.14}$$

Depending on the soliton momentum, the intersection with the dispersion of the linear polaritons can be at $k \leq 0$. Therefore the Cherenkov radiation

momentum and group velocity can be zero or negative, referring to radiation that stays near to where it was emitted or propagates in the opposite direction of the solitons generating it.

Simulations of backwards Cherenkov radiation obtained from the 2D modeling of Eq. 5.1-5.4 are shown in Fig. 5.7.

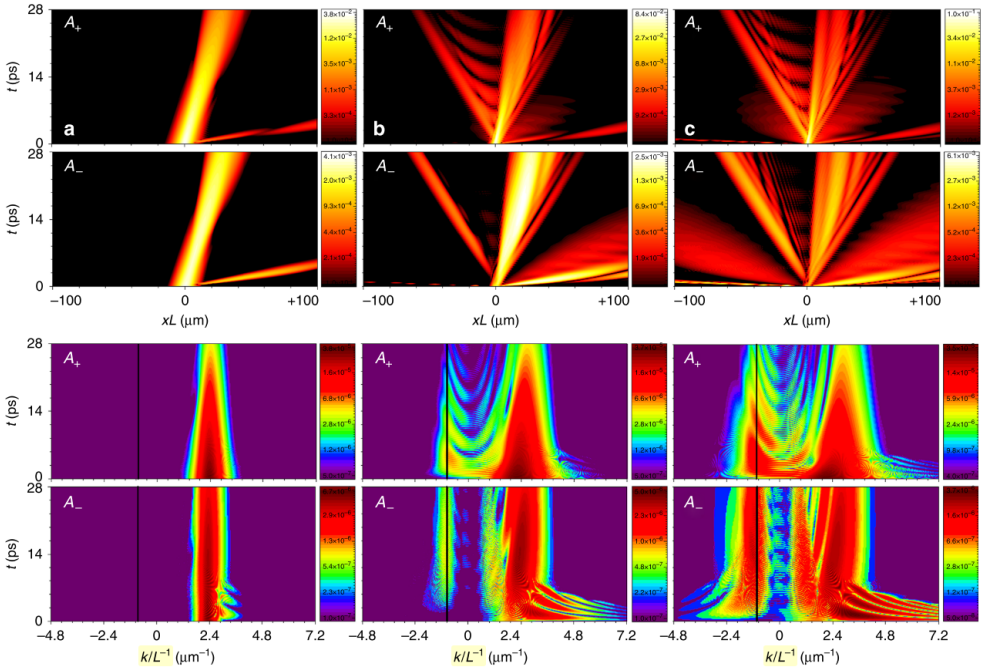

Figure 5.7: Emission of the backward Cherenkov radiation. Results of the 2D modelling of Eqs. 5.1-5.4 showing evolution of the quasi-solitons and of the backward-emitted Cherenkov radiation with the negative momentum and negative group velocity. (x, t)-plots show the space-time dynamics of $|A_{\pm}(x,t)|$ and (k, t)-plots show the corresponding evolution of the photon density in the momentum space. The waves deviating towards negative values of x in the (x, t)-plots in columns b and c are the backward Cherenkov radiation. Vertical black lines on the (k, t)-plots show theoretically predicted momenta of the Cherenkov radiation [191].

5.4 Experimental Results

Experiments were carried out as described in 5.2. We performed two series of experiments to firstly demonstrate bright soliton formation and then Cherenkov

radiation.

To achieve soliton formation, we excited with a TE-linearly polarised pulsed laser (Tsunami spectra physics, see 3.2.3) of $\simeq 5$ ps-long full width at half maximum (FWHM). We needed to excite the polariton pulses in the negative effective mass region (as explained in the previous section). Therefore, we adjusted the momentum of the excitation pulse above the inflection point of the lower polariton branch, at $k_x \simeq 2.2\mu m^{-1}$.

The excitation beam couples more efficiently to the ground polariton mode than to the first excited mode and creates a polariton pulse $\simeq 30\ \mu m$ wide that propagates along the x direction.

The results of varying the power of the excitation beam are showed in figure 5.8. We observed quasi-linear propagation at low powers (10 μW) and solitonic compression at high powers (100 μW). A snake-like pattern appears in real space (Fig. 5.8 panels a-c) due to the superposition of the ground and first polariton modes [202].

At low power (10 μW), the pulse propagates until the photoluminescence signal decays to the noise level (Fig 5.8 a, b). Pulse width stays quasi-linear without showing compression. In real space, the pulse changes its shape with time through the group velocity dispersion.

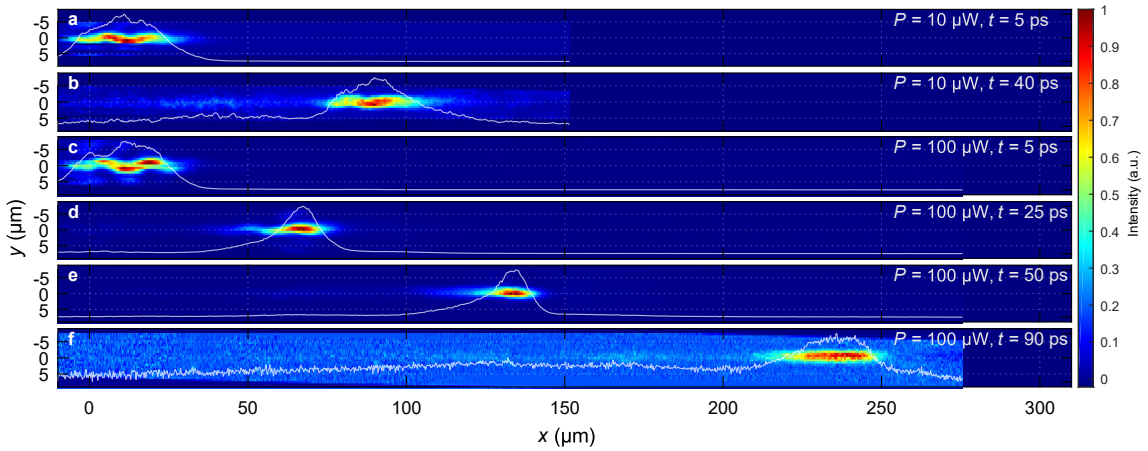

Figure 5.8: Real space evolution of pulses in time. (a,b) Low excitation power P=10 μW polariton pulse at (a) 5 ps and (b) at 40 ps. (c-f) Polariton pulses with high excitation power P=100 μW, showing soliton shrinking effect (d,e) followed by expansion (f), captured at (c) 5 ps, (d) 25 ps, (e) 50 ps and (f) 90 ps. Time t=0 corresponds to the arrival of the excitation pulse. White lines show the normalised intensity profiles integrated over y [191].

At higher power (100 μW), solitons are observed. The pulse width decreases to $\simeq$ 12 μm in the first 40 ps (Figs 5.8d,e and 5.9 a). The shrinking of the pulse width indicates that the chirps produced by the dispersion and the nonlinearity are compensated by each other, allowing the formation of bright solitons. After the soliton width reaches its maximum of compression it can either start spreading out or break up into a train of weaker solitons. In this case, the point of minimum spreading occurs at around 40 ps, and then the soliton starts to expand adiabatically (Fig 5.9).

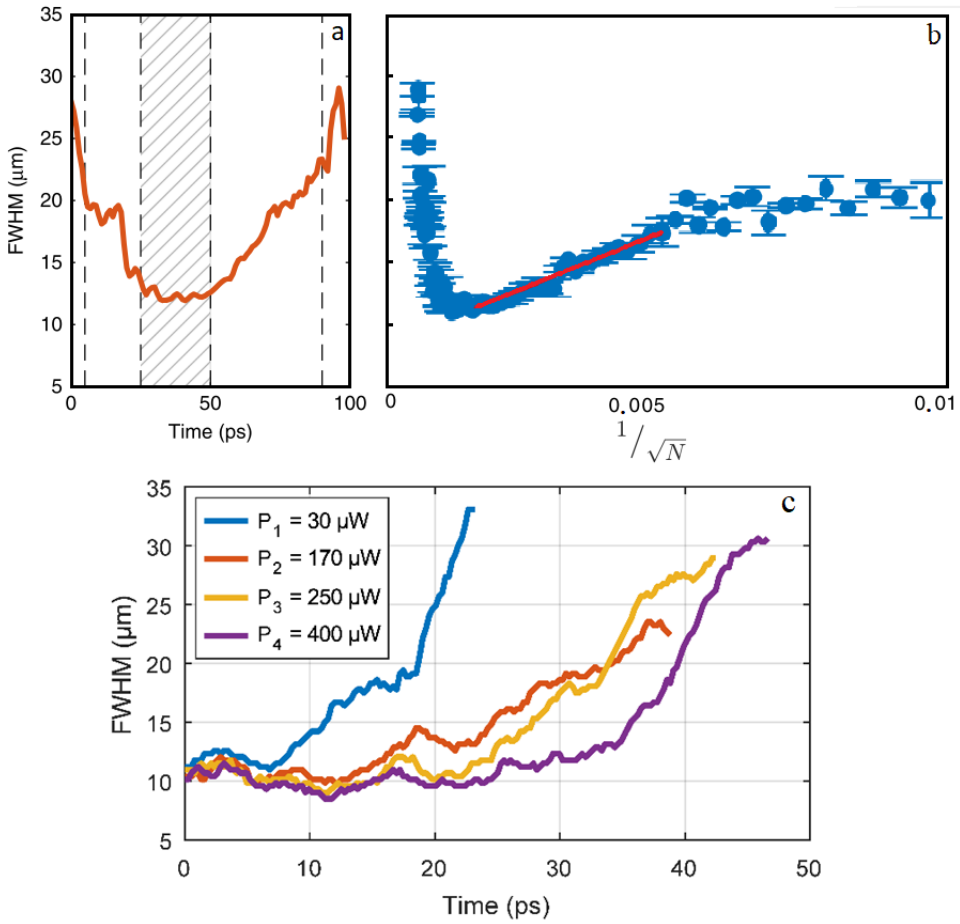

Figure 5.9: Soliton compression effect (a) FWHM vs time. 5 ps excitation pulse, P=100 μW. The pulse undergoes an initial compression during the first 40 ps and then spreads out. [191] (b)5 ps excitation pulse, 100 μW. FWHM vs $1/\sqrt{N(t)}$, where N is the polariton density proportional to the emission intensity (c) FWHM evolution for a 2 ps excitation pulse at different powers.

The width of a bright conservative soliton w can be approximated by the healing length of the polariton fluid, which is obtained by equating the kinetic

energy due to dispersion to the potential energy due to the polariton-polariton interactions and is described by $w(t) = 2\hbar/\sqrt{2MgN(t)}$ where N(t) is the polariton density, g is the interparticle interaction coefficient and M is the polariton effective mass [19]. Figure 5.9 panel b shows the evolution of the polariton emission intensity (proportional to the polariton density) vs the wavepacket width. Between 40 and 80 ps, when there is an increment of the size of the wavepacket (Fig. 5.9(a)), there is a linear dependence of the wavepacket width with $1/\sqrt{(N)}$ (Fig. 5.9(b)) in agreement with the predicted solitonic behaviour.

In this regime, (5 ps excitation pulse at $k_p \simeq 2.2\mu m^{-1}$ and 30 μm wide) we achieved the formation of bright solitons when their Cherenkov radiation is either negligible or inexistent.

To observe Cherenkov radiation we performed a second experiment, where the excitation pulse was shorter (2 ps) and smaller in real space ($\simeq 11$ μm (FWHM)). The pulse momentum was chosen higher, at $k_p \simeq 2.4$ μm^{-1} for a Cherenkov resonance of -0.9 μm^{-1} (see Fig 5.6) to produce Cherenkov radiation traveling in the opposite direction of the solitons.

We varied the excitation power from 30 μW to 15 mW. As shown in Fig 5.9c, at the lowest power, the FWHM quickly increases up to 30 μm, because at this power the weak nonlinearity is unable to compensate the spreading out of the pulse caused by the polariton dispersion. At higher powers (≥ 170 μW), the nonlinearity due to polariton-polariton interaction becomes strong enough to balance the dispersion resulting in non-dispersive propagation of the pulse for about 30 ps. The non-dispersive propagation lasts longer for higher powers. For 400 μW, the pulse width fluctuates slightly between 8 and 12 μm (Fig 5.9b) for about 30 ps, while for P=170 μW it starts spreading out at t ≈20 ps.

As predicted in the theory (5.3), the group velocity and momentum of the Cherenkov radiation depends of the excitation power and momentum. For low power, the soliton dispersion shifts closer to the dispersion of the linear polaritons and intersects it at $k_x \approx 0$. It produces Cherenkov radiation with a velocity around zero (fig5.6). At higher powers, the repulsive nonlinearity is bigger and the soliton dispersion is shifted upwards from the linear spectrum and towards negative momenta in the range between 0 and $-2\mu m^{-1}$.

Figures 5.10 and 5.11 show the recorded soliton traces in both real space (x coordinate vs time) and far field (k_x momentum vs time). The soliton width (FWHM) evolution in time is shown in figure 5.9 c.

Figure 5.10 shows that Cherenkov radiation emerges at the critical power of $P \simeq 770$ μW after $\simeq 20$ ps. The radiation appears as a nonpropagating polari-

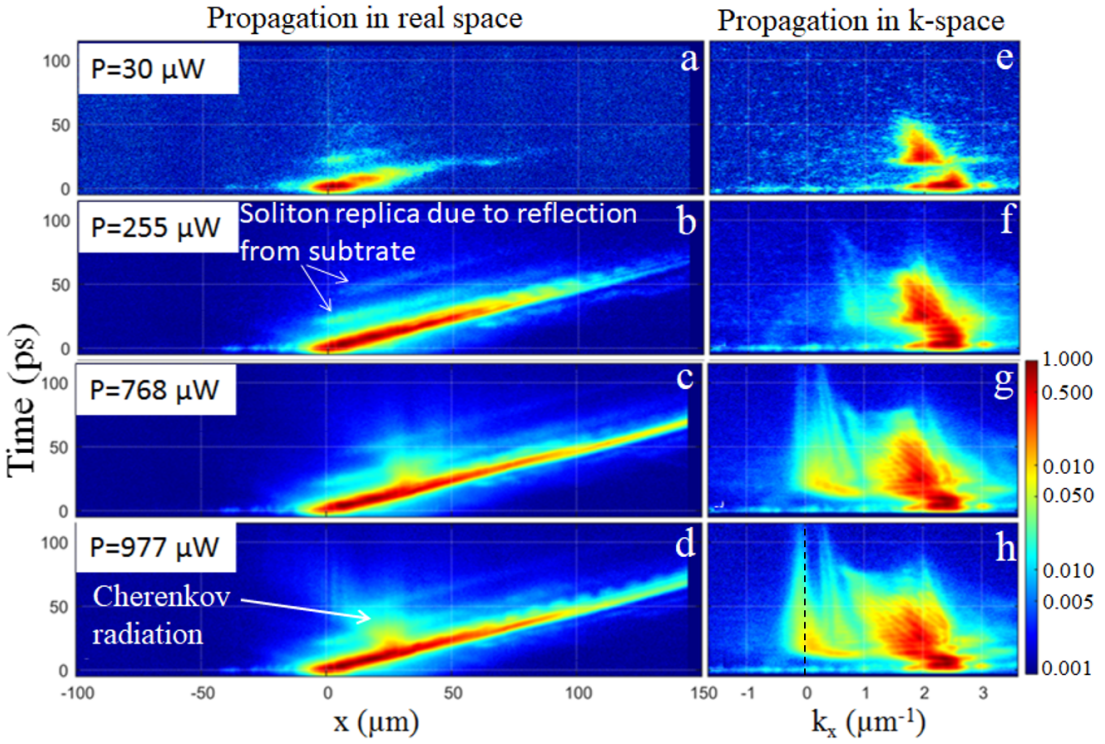

Figure 5.10: Experimental data showing non propagating Cherenkov radiation at low excitation powers. (a-d) Real space images of the polariton emission intensity vs time and the propagation direction x measured at the centre of the microwire ($y = 0 \pm 0.2\mu m$) for different excitation beam powers (< 1 mW). Time t=0 corresponds to the arrival of the excitation pulse. (e-h) Far field images of the polariton emission intensity vs time and k_x momentum recorded at $k_y \simeq 0$ for increasing excitation powers. In panel (h) a dotted line shows the position of $k_{cr} = 0$. [191]

ton emission at $k_{cr} \simeq 0$. The corresponding image in k-space shown in panel g consists of a broad range of harmonics with different k-vectors populated by polariton-polariton scattering from the initially excited state, thus triggering the Cherenkov radiation at $k \approx 0$. When increasing the excitation power (panel d and h), Cherenkov radiation starts propagating backwards, with negative momentum at $k_x \simeq -0.2\mu m^{-1}$. As predicted, Cherenkov radiation momentum and group velocity increases with the excitation power, from 0 at 768 μW to $k \simeq -0.5\ \mu m^{-1}$ at 15 mW (fig 5.11), corresponding to fast backward-propagating Cherenkov radiation in real space (fig 5.11c).

Figure 5.11 shows the real space and k space evolution of the Cherenkov radiation at higher excitation powers. At P=3 mW the input pulse splits creating

a weak second quasi-soliton at $\simeq$ 50 ps, in a similar process to the well-known soliton fission observed in optical fibres [130]. At P=15 mW the pulse transforms into a complex spatio-temporal multi-peak structure. In k-space (panel g) we also observe a modulated spectrum.

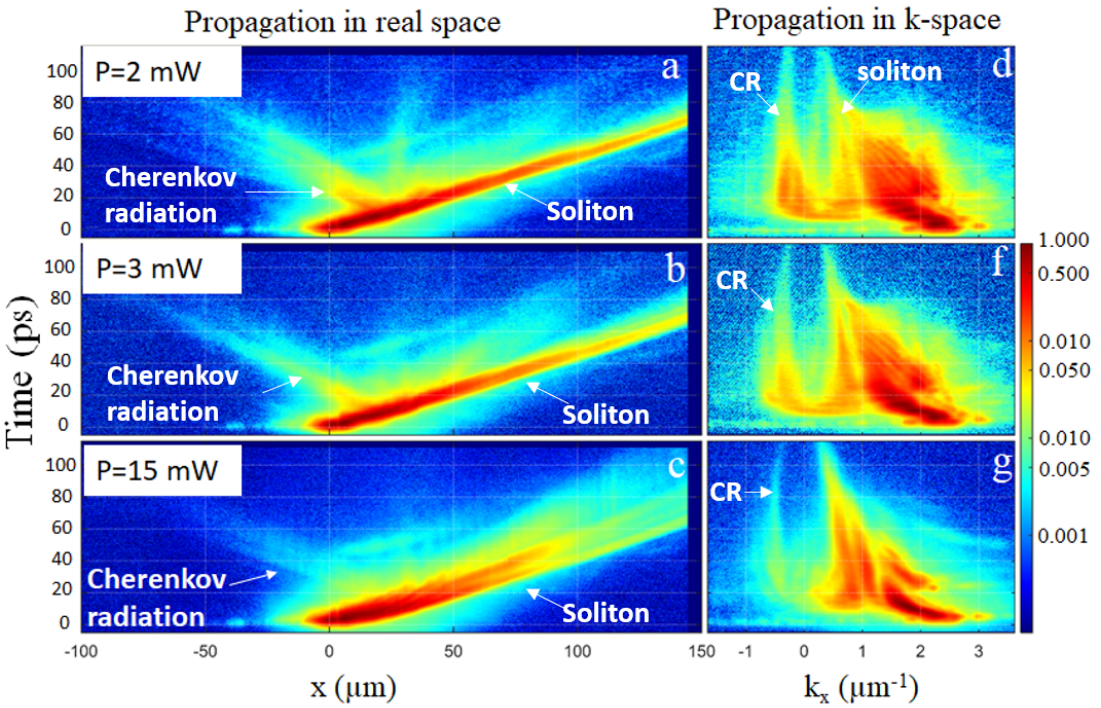

Figure 5.11: Experimental data showing backward Cherenkov radiation at high excitation powers. (a-d) Real space images of the polariton emission intensity vs time and the propagation direction x measured at the centre of the microwire ($y = 0 \pm 0.2\mu m$) for different excitation beam powers ($\geq$ 2 mW). Time t=0 corresponds to the arrival of the excitation pulse. (e-h) Far field images of the polariton emission intensity vs time and k_x momentum recorded at $k_y \simeq 0$ for increasing excitation powers. [191]

Wavepackets that propagate in the same direction than the main soliton but with a smaller velocity appear at powers greater than 2 mW (Fig 5.11). They emerge 5-10 ps after the backward Cherenkov radiation. These wavepackets correspond to the expected forward Cherenkov radiation emitted by the evolving soliton due to gradual photonic losses of polaritons.

Also at high powers (2-15 mW), we observed a reduction of the width and central wavelength of the momentum distribution over time (fig 5.11 right column). This happens due to polariton free-carrier, polariton-phonon and polariton-polariton

scattering that gradually relaxes their momentum to zero. In real space, spatio-temporal maps (left column in fig 5.11) does not show a visible change in the group velocity because the solitons central momentum is near the point of inflection in the LPB (fig 5.6), where the velocity is close to independent of momentum.

In general, we observed good agreement between the theory (5.3) and our experimental results including spatio-temporal maps in both real and k space.

5.5 Conclusions

In this chapter I have shown our study of the nonlinear effects accompanying the ultra-short pulse propagation in a pump free microwire guiding exciton-polaritons.

We have introduced an approximate model that has exact soliton solutions and demonstrated theoretically and experimentally the existence of backward Cherenkov radiation emitted by the polariton solitons in the microwires.

Our experimental results are in excellent qualitative agreement with the numerically modelled spatio-temporal patterns developed by Skryabin et al. (Fig 5.7).

We have experimentally measured backwards and non-propagating Cherenkov radiation, bright soliton formation and nonlinear pulse compression. We observed that at low powers, solitons appear without Cherenkov emission and after a threshold (> 0.76 mW in our measurements) Cherenkov radiation emerges. At low powers, we recorded Cherenkov radiation with velocities near zero. When increasing the excitation power (>2 mW) we observed an increment in the radiation momentum and velocities, until reaching fast backward Cherenkov radiation moving at similar velocities to the quasi-solitons emitting it.

Backwards Cherenkov radiation can be considered an independent signature of high-power solitons in microwires.

Polariton microcavity wires are seen as the future building blocks of polariton information processing circuits [203], where the bright conservative solitons and Cherenkov effects studied in this chapter are expected to play a role as significant as they have done in fibre optics [129, 130] and nanophotonics [199].

Chapter 6

Spin domains in one-dimensional conservative bright solitons

As part of our study of the propagation of picosecond pulses in microwires, I present in this chapter the formation of spin domains observed through the polarization resolved measurements of conservative bright solitons.

A summary of the results presented here was already published in [204]. All the experimental results shown in this chapter were obtained by me with the guidance of Maksym Sich, Maurice Skolnick and Dmitry Krizhanovskii. Theory and modelling were developed by H. Sigurdsson, Ivan Shelykh, Evgeny Sedov, Alexey V. Kavokin and Dmitry Skryabin.

As mentioned in the previous chapter, the study of the effects occurring when guiding polaritons in microwires is of vital importance for future applications in polaritonic devices, and the presence of the spin domains, which will be shown in this chapter, could represent a new possibility for polariton spinoptronic devices such as soliton-based logic gates [7] or spin transistors [205] .

6.1 Introduction to optical polarization (or spin) domains

Temporal and/or spatial domain formation have played an important role in many sciences, such as biology, magnetism and optics. In biology, it has been shown that domain formation on cell membranes is related to certain processes,

including membrane sorting, signal transduction, virus trafficking and protein processing [206]. In physics, magnetic domains are the responsible of the magnetic behaviour of ferromagnetic materials. Their most popular application occurs in computer's hard drives, where the information is stored in the magnetic layer below the surface of the disk by creating small magnetic domains.

In optics, polarisation domain formation is a nonlinear process where neighbouring domains are separated by a domain wall, a form of topological defect arising from modulational instability in the media [207]. It has been shown that polarization domains in self-defocussing Kerr media is directly linked to soliton formation [208]. Polarization domain walls were observed in optical fibres in 2017, confirming their solitonic nature and their possible application as topological bits for data transmission [209].

Because of their high optical nonlinearity, exciton-polaritons are a natural option for the study of polarization domains. The spin of polaritons is directly linked with the polarization of the emitted light from the microcavity, the two possible spin projections on the growth direction correspond to right and left circular polarisations. Polariton-polariton interactions are also spin dependent, polaritons with the same spin projections repel each other, while polaritons with opposite spin only weakly interact and can even attract each other (see 2.5.1).

Nonlinear polarisation phenomena that have been previously observed in polariton systems includes spin-selective filtering [210], spin switching [8], polarisation dependent stability of dissipative solitons [211] and dark half solitons [54]. The first observation of spin domains in a polariton system, is presented in this chapter.

6.1.1 Poincaré sphere

As explained in 2.5.1, the spin of polaritons can be described with the same pseudospin notation extensively used for electrons. A pure spin state $|\psi\rangle$ is written as

$$|\psi\rangle = cos\frac{\theta}{2}|\uparrow\rangle + e^{i\varphi}sin\frac{\theta}{2}|\downarrow\rangle \tag{6.1}$$

All these states can be represented as a point on a sphere surface, where θ gives the inclination angle and φ the azimuth angle. This sphere formed by the pseudospins is called the Bloch sphere and is shown in figure 6.1b.

The polariton pseudospin is directly linked to the emitted light polarization (2.5.1). Each spin state corresponds one to one to a Stokes vector, which fully describes the polarization of the light coming out from the cavity (fig 6.1a).

The Stokes vector (normalised to unity) is defined as: $S^* = (S_1^*,\ S_2^*,\ S_3^*)$ where each of its components is the degree of linear, diagonal and circular polarization respectively and are defined as follows:

$$S_1^* = \frac{\psi_+\psi_-^* + \psi_+^*\psi_-}{|\psi_+|^2 + |\psi_-|^2} = \frac{I_h - I_v}{I_h + I_v} \tag{6.2}$$

$$S_2^* = i\frac{\psi_+\psi_-^* - \psi_+^*\psi_-}{|\psi_+|^2 + |\psi_-|^2} = \frac{I_d - I_{ad}}{I_d + I_{ad}} \tag{6.3}$$

$$S_3^* = \frac{|\psi_+|^2 - |\psi_-|^2}{|\psi_+|^2 + |\psi_-|^2} = \frac{I_{\sigma^+} - I_{\sigma^-}}{I_{\sigma^+} + I_{\sigma^-}} \tag{6.4}$$

Here the total intensity in the circular basis of the cavity light $(\psi_+;\psi_-)$ is given by $S_0 = |\psi_+|^2 + |\psi_-|^2$. And I_P are the intensities in the horizontal (h), vertical (v), diagonal (d), antidiagonal (ad), left-hand circular (σ^-) and right-hand circular (σ^+) polarization.

It can be noted that $S_0^2 \leq S_1^{*2} + S_2^{*2} + S_3^{*2}$ is the equation of a sphere in the Stokes parameter space. It is known as the Poincaré sphere and its surface represents the total of the polarization states of light.

In the following sections we use the Poincaré sphere, and Stokes vectors, to present the evolving polarization of conservative solitons in a microcavity wire.

6.2 Experimental Layout

We used the same 5 μm wide microwire than in the previous chapter (3.1.2).

A similar experiment to the one where we observed Cherenkov radiation was carried out (see 5.2). A pulsed laser was focused on the microwire resulting in the propagation of a soliton in one direction and Cherenkov radiation in the opposite way.

In this chapter we studied the polarization of the propagating soliton as a function of time and the spatial coordinate. Polarization time resolved measure-

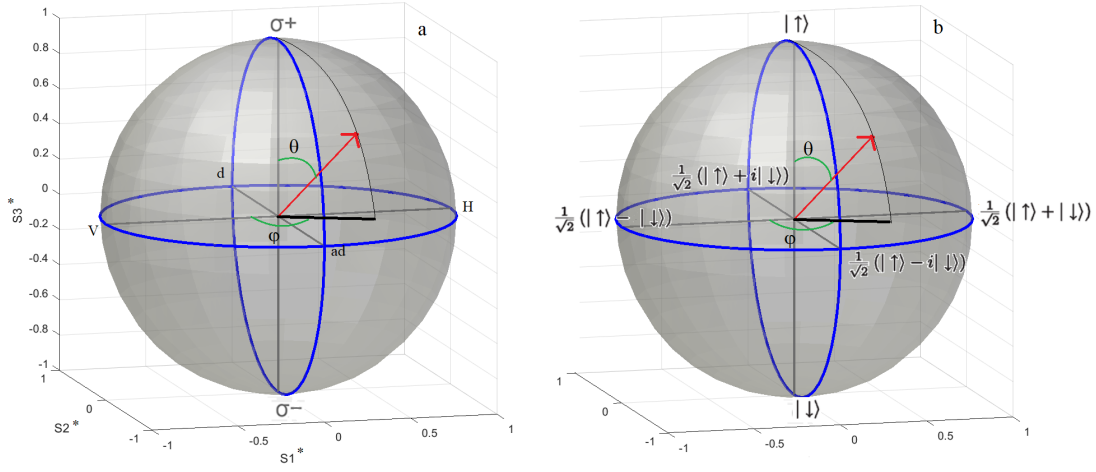

Figure 6.1: Poincaré and Bloch spheres showing the one to one correspondence between a Stoke vector and a spin vector. (a) Poincaré sphere. The red arrow shows a Stoke vector that characterizes the polarization of light. Each point on the sphere surface represents a polarized state. (b) Bloch sphere. Here the red arrow is a spin vector. The poles correspond to the spin up and spin down states. The vertical axis corresponds to the z axis (growth direction) in a microcavity system.

ments were done using the optical setup described in 3.7, with the final mirror sending the signal to the streak camera.

Our control parameters in the experiment were the pulse power, centre wavelength, angle of incidence and polarization angle. However, as in the previous chapter (5.2), to achieve soliton formation we fixed the wavelength to be quasi-resonantly with the LPB and the excitation k-vector above the point of inflection at $k_x \simeq 2.2\ \mu m^{-1}$. The pulse duration was $\simeq 5$ ps (FWHM). It was linearly polarized, we varied the angle of its polarization with a halfwave plate (fig 3.7).

In the following sections polarization angles are defined according to the laboratory frame, the figure 6.2 shows the polarization relative to the microwire position.

6.3 Experimental Results

We performed the experiment described in the previous section, starting with the case of excitation with vertical (TE) polarization. We separately measured

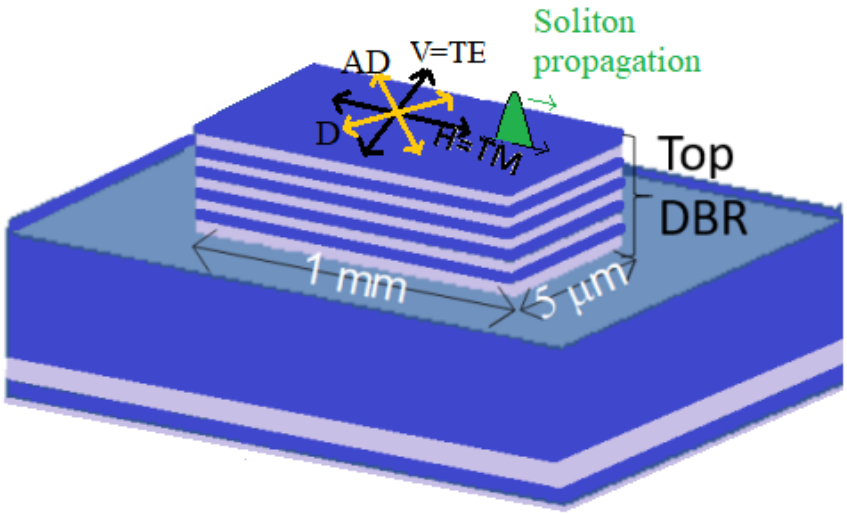

Figure 6.2: Scheme of the experiment showing the polarization relative to the microwire position. We excited with a pulsed laser from the back of the sample. The microwire is aligned along the x direction, which corresponds to the horizontal polarization (TM). Vertical polarization (TE) is aligned perpendicular to the wire. Diagonal (D) and antidiagonal (AD) polarization directions are also showed in the image.

the emission intensity of each polarization: horizontal, vertical, diagonal, antidiagonal, right hand circular and left hand circular and recorded each of the components of the Stokes vector (see equations 6.2). We varied the excitation pulsed pump power from 13 μW to 3.1 mW and observed soliton formation and Cherenkov radiation as in the results showed in chapter 5.

The polarization-resolved propagation of the soliton at low excitation powers is shown in figure 6.3. At the lowest power (P=13 μW) the soliton has not formed yet, the polariton nonlinearity is very weak thus the wavepacket propagates in the linear regime, spreading due to the dispersion. At 87 μW the polariton nonlinearity becomes strong enough to balance the dispersion allowing the non-spreading propagation of a soliton. The evolution in time of the polarization of the soliton at this low power is plotted over the Poincaré sphere in fig 6.4.

We note that at time t=0, the measured polarization already has diagonal and circular components, even though the excitation beam is completely TE (vertically) polarized. This could be due to birefringence in the substrate and the influence of the edges of the microwire on the polarization of the pump.

At low power (87 μW) we observed polarization precession along the soliton

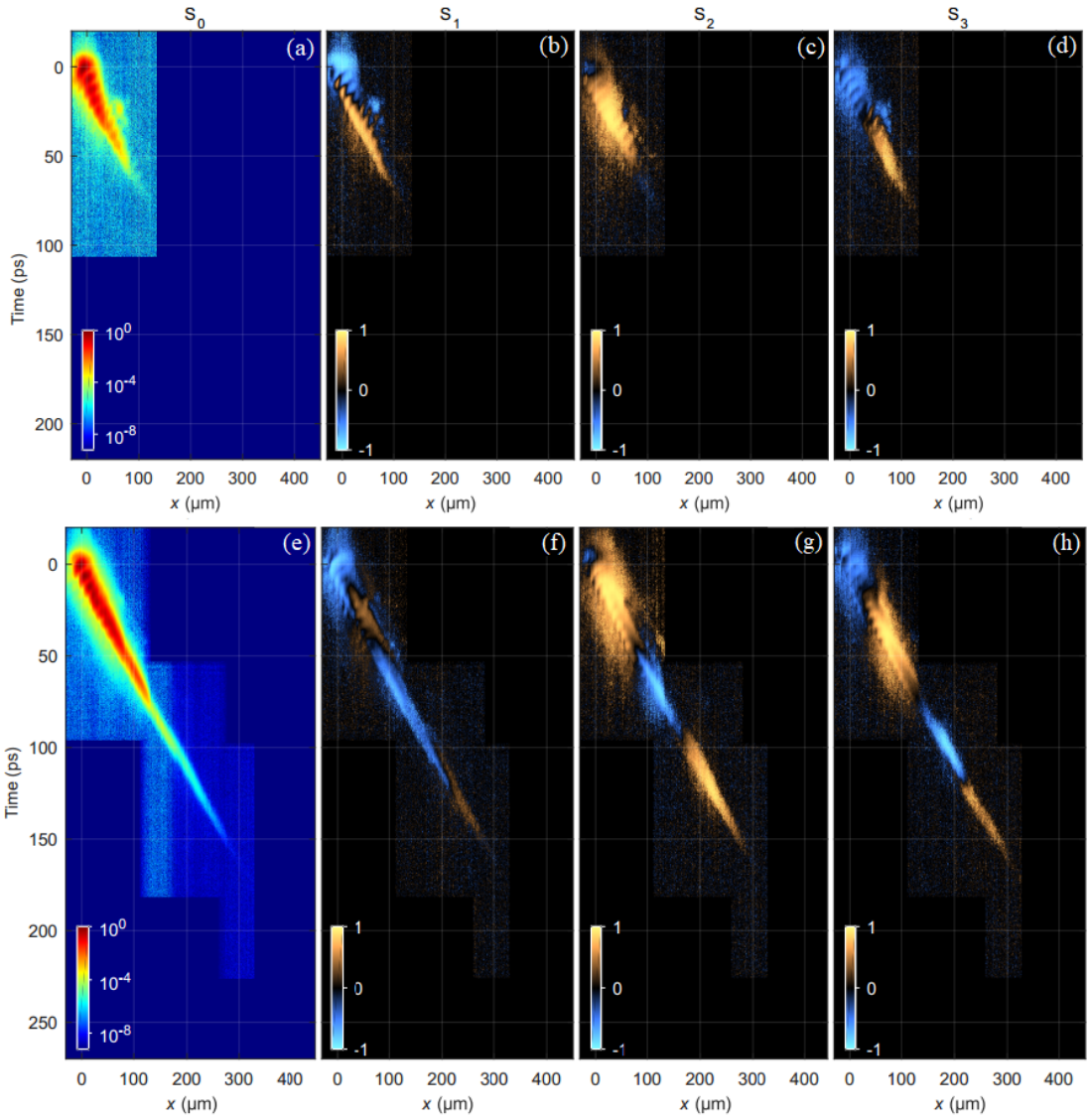

Figure 6.3: Polarization-resolved propagation of the soliton in real space. Polariton emission intensity (S_0) and polarization Stokes components (S_1^*, S_2^* and S_3^*) are shown separately for 2 different low excitation powers: (a-d) 13 μW and (e-h) 87 μW. All the data was taken at $y = 0 \pm 0.5$ μm. [204]

propagation (Figures 6.3 and 6.4). We observed that the three components of the Stokes vector oscillate between positive and negative values with time. The polarization beats in Fig 6.3 f-h, correspond to the motion of the Stokes vector around the Poincaré sphere showed in 6.4d, in which the precession of the vector as the soliton propagates is clearly visible. Note, that for clarity we plotted the Stokes vector scaled to 1, while the experimentally measured degree of polariza-

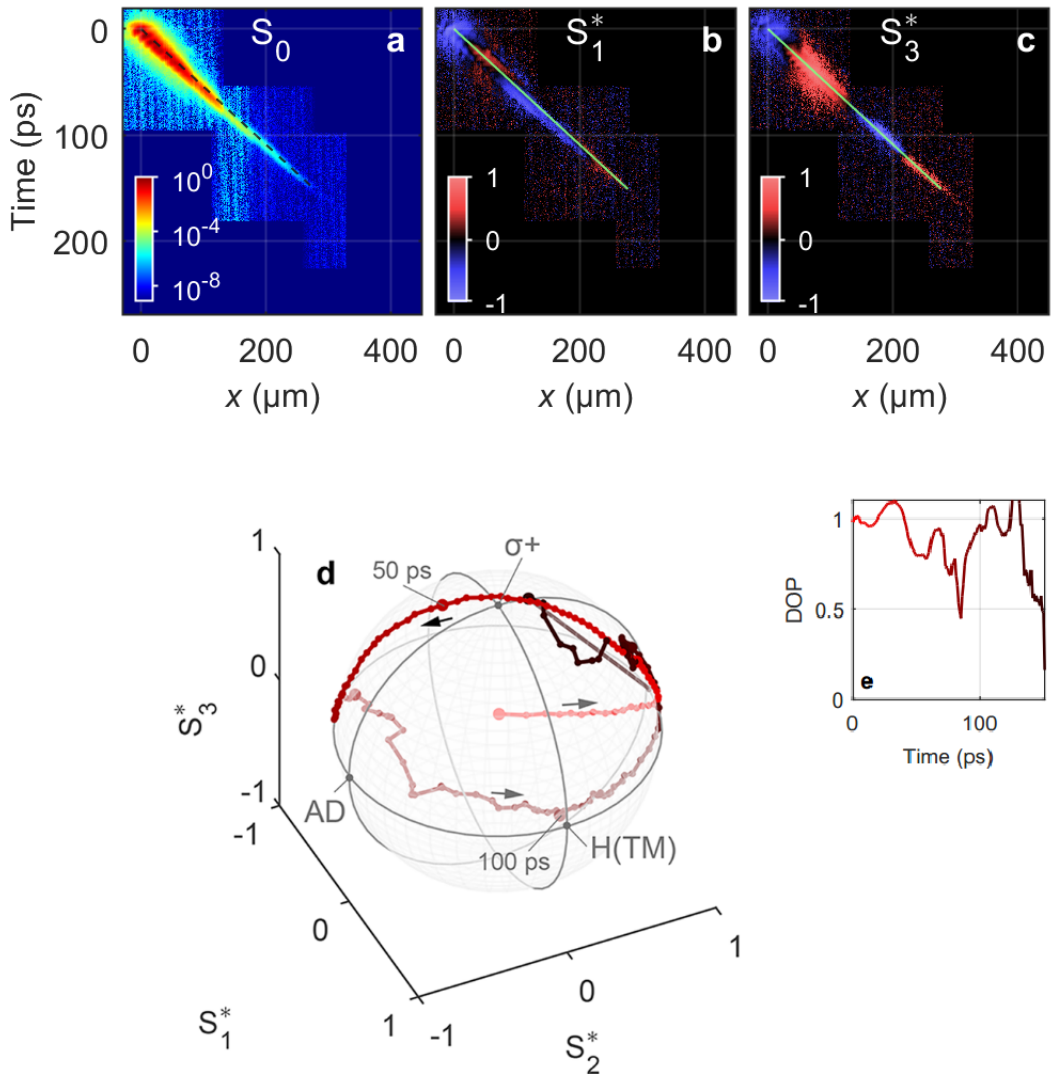

Figure 6.4: P=87 μW. (a,b,c) Show the S_0, S_1^* and S_3^* Stokes components. The green line (dotted line in a) shows the spatial points of the soliton profile where we measured the values of the Stokes vector for the reconstruction in panel d. (d) Evolution of the Stokes vector plotted on the surface of the Poincaré sphere. The brighter (dimmer) lines correspond to the evolution of the vector on the front (back) surface of the sphere. The length of the experimental Stokes vector is normalised to unity. (e) Degree of polarization vs time along the plotted points on panel d. [204]

tion ($DOP = \sqrt{S_1^{*2} + S_2^{*2} + S_3^{*2}}$) differs from 1 and the Stokes vector usually lies inside the sphere (Fig. 6.4e). It is not clear what leads to the observed

depolarization, it may be some fast oscillation of the Stokes vector not detected experimentally or a depolarization occurring during the soliton emission because of the interaction with the edges of the microwire.

The observed polarization rotation can be described as a polariton pseudospin precession around a time-varying effective magnetic field [212]. Three different mechanisms are involved in the creation of this effective magnetic field: splitting between D and AD polarized components induced by strain, electronic anisotropy or crystallographic anisotropy [213,214]; TE-TM splitting [54,215]; and polariton-polariton interactions. The effective magnetic field induces an energy splitting of $\Delta_{eff} = 2\hbar/T \simeq 22\ \mu eV$ according to the measured precession period $T \simeq 60$ ps.

At higher powers a completely new behaviour appears. Whilst at P=0.24 mW polarization precession is still present, especially in the diagonal and circular components (figure 6.5), at P=0.95 mW we observe formation of stable propagating domains in all the Stokes vector components. This drastic change in the polarization behaviour is accompanied by the appearance of Cherenkov radiation and the transformation of the single soliton observed at lower powers into a soliton doublet at $t \simeq 50$ ps (around 20 ps after the emission of Cherenkov radiation). The two almost orthogonally-polarised domains are spatially separated and correspond to each of the soliton doublet spatial components. This domain formation is observable in all the polarization components, but it is most pronounced in the S_1^* (H-V linear polarisation basis). Polarization precession is still present; however, its scope is reduced and polarizations of the front and back domains remain nearly orthogonal.

The evolution of the Stokes vectors at this intermediate power (P=0.95 mW) is plotted over the Poincaré sphere in Figure 6.6, with one soliton of the doublet in each panel. During the first 50 ps of the solitons propagation, we observed a very fast precession around the poles of the Poincaré sphere. This precession has a period of T $\simeq$ 10ps (for the trace 1), corresponding to an induced energy splitting of $\Delta_{eff} \simeq 130\ \mu eV$ due to an effective magnetic field arising from the spin-dependent polariton nonlinearity.

At later times ($t > 50$ ps), after the soliton doublet is clearly formed, the polariton density and nonlinearity decreases producing a slower polarization precession with a period of 120-125 ps. The precession remains orthogonal for each domain. Polarization continues moving around the poles of the Poincaré sphere, depending on each soliton of the doublet: the first one (trace1) moves around the south pole ($\sigma^+ = 1$) and the second one (trace2) around the north pole corresponding to $\sigma^- = 1$ or left-handed circular polarization.

At the highest pump power, P = 3.1 mW, we observed a further onset of

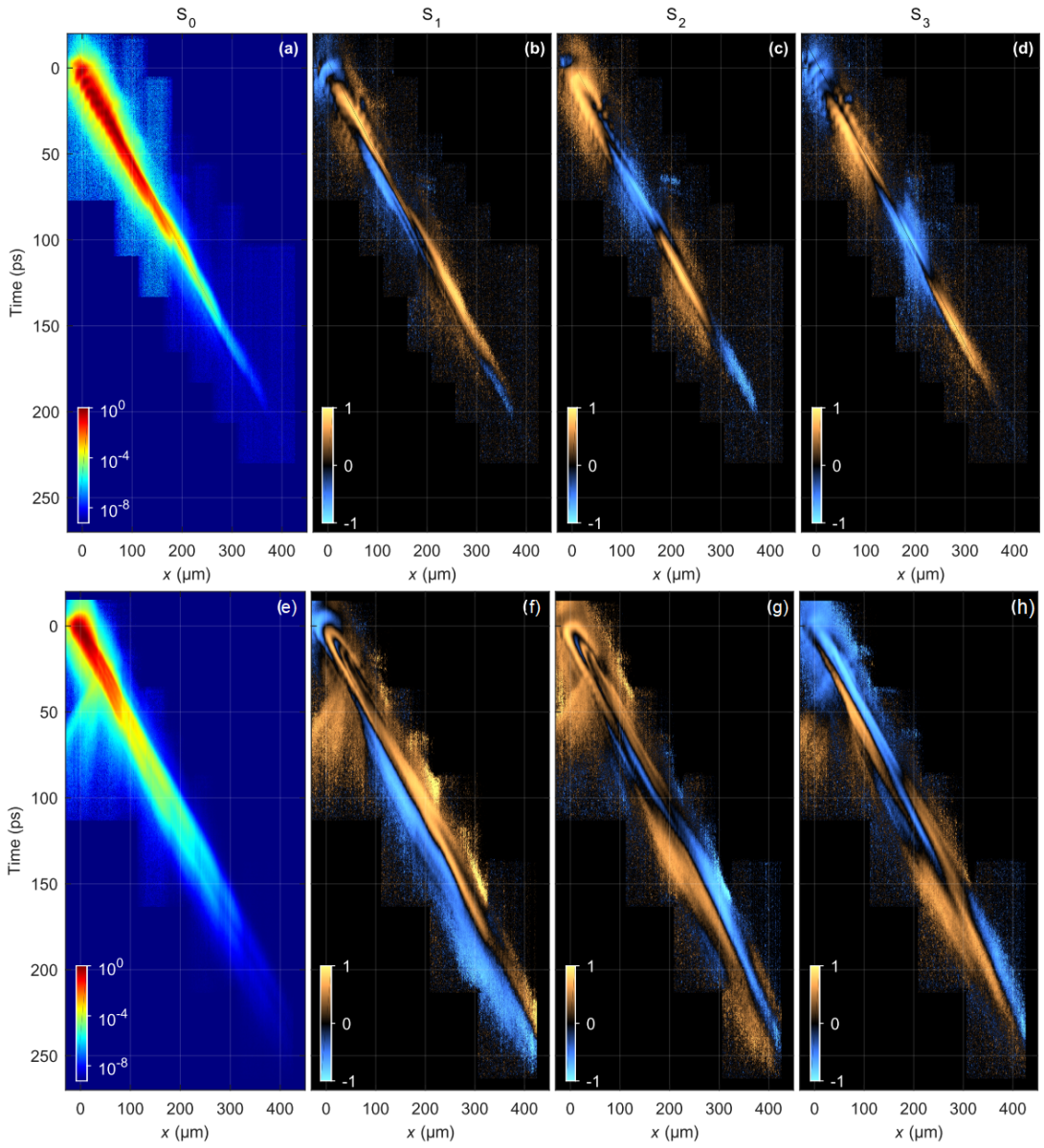

Figure 6.5: Polarization-resolved propagation of the soliton in real space. Polariton emission intensity (S_0) and polarization Stokes components (S_1^*, S_2^* and S_3^*) are shown separately for 2 different intermediate pump powers: (a-d) 0.24 mW and (e-h) 0.95 mW. All the data was taken at $y = 0 \pm 0.5\ \mu m$. [204]

cascaded polariton-polariton scattering resulting in a complex emission pattern, as discussed in the previous chapter (5). Because of the high power, polariton relaxation results in the additional occupation of states with positive effective mass, this results in the propagation of a spreading polariton wavepacket traveling

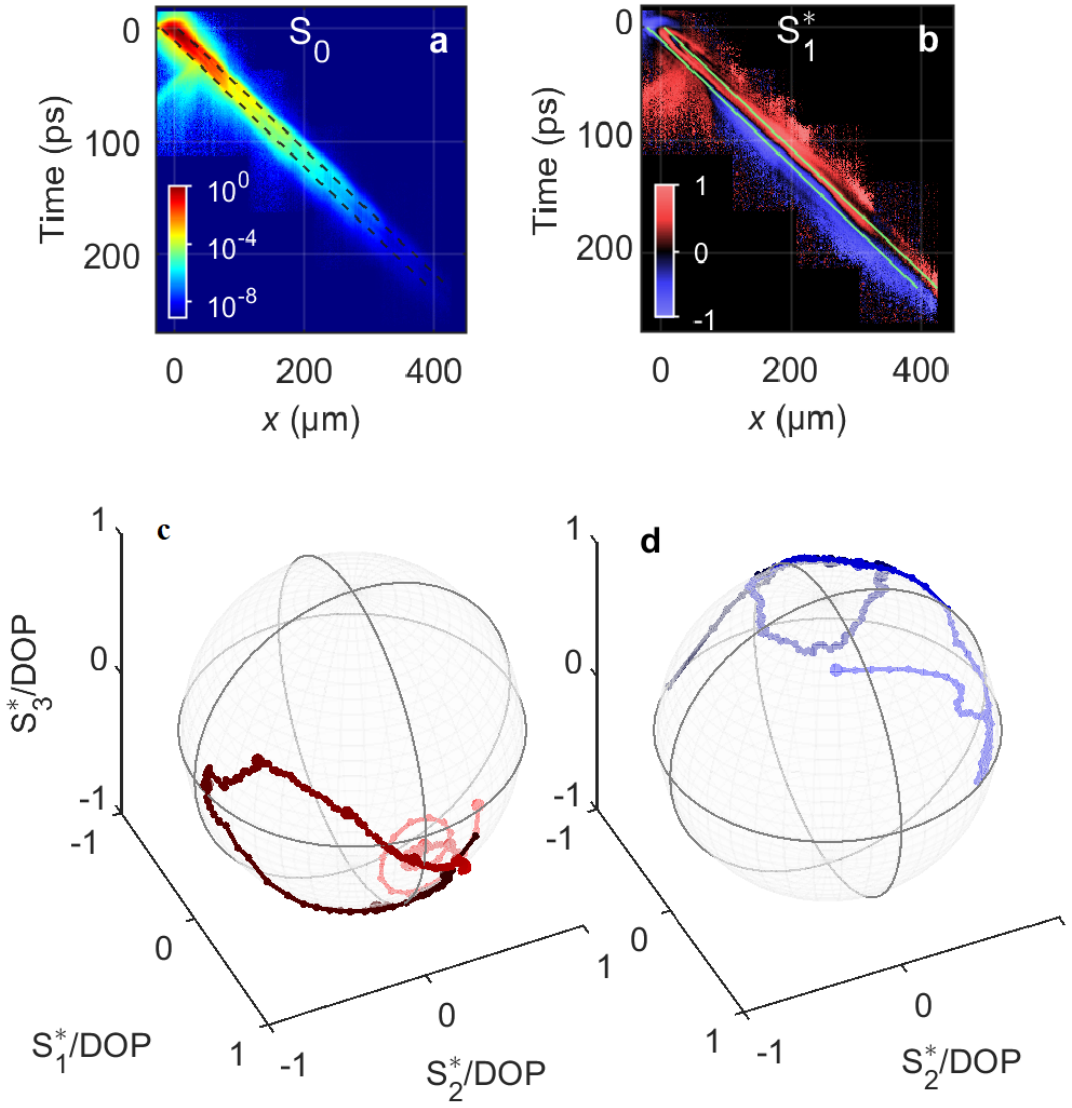

Figure 6.6: P=0.95 mW. (a,b) Show the total intensity (S_0) and linear polarization (S_1^*) Stokes components. Traces 1 and 2 showed as green lines (dotted lines in a) show the spatial points of the soliton profile where we measured the values of the Stokes vector for the reconstruction in panels c and d. (c,d) Evolution of the Stokes vector for traces 1 (c) and 2 (d) plotted on the surface of the Poincaré sphere. The brighter (dimmer) lines correspond to the evolution of the vector on the front (back) surface of the sphere. The length of the experimental Stokes vectors is normalised to unity. [204]

in the same direction as the coexisting solitons. A more complex polarization dynamics emerges, while circular polarization domains still remain for the first

≈ 50 ps after ejection of the Cherenkov radiation wavepacket, similar to the case of the intermediate power (see S_3^* in figure 6.7). At later times, the nonlinearity becomes weaker and the wavepacket breaks into a spray of precessing polarization domains.

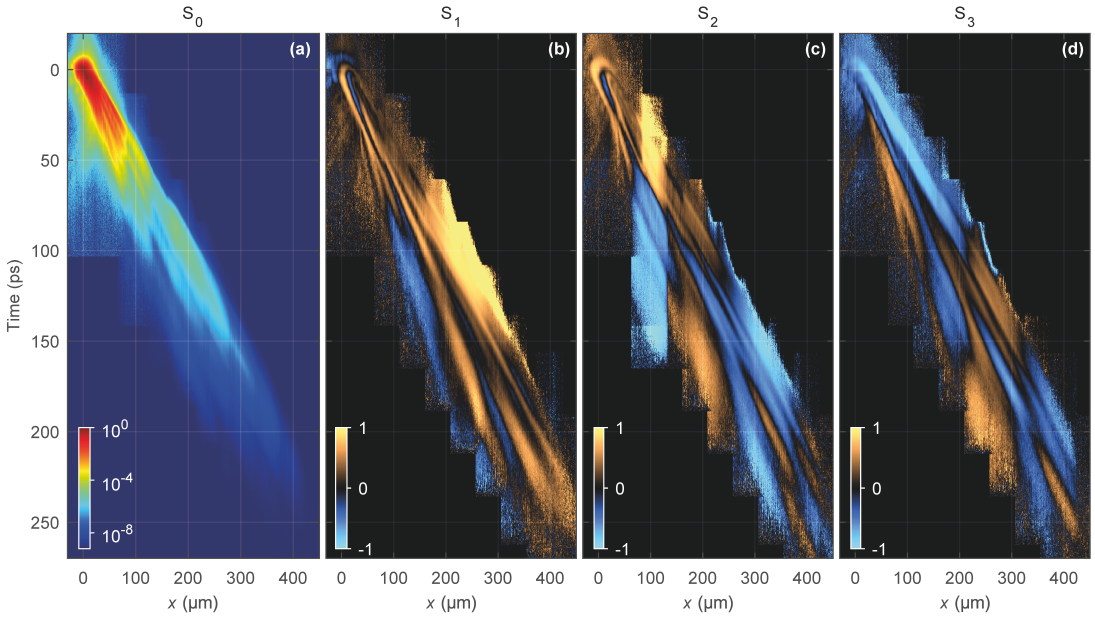

Figure 6.7: Polarization-resolved propagation of the soliton in real space at high excitation power P=3.1 mW. Polariton emission intensity (S_0) and polarization Stokes components (S_1^*, S_2^* and S_3^*) are shown separately. All the data was taken at $y = 0 \pm 0.5\ \mu m$. [204]

Figure 6.8 shows the evolution of the Stokes vectors along the two profiles showed in panels a and b. We notice a much more complex polarization dynamics which originates from the out-of-plane effective magnetic field induced by the spin-dependent polariton nonlinearity.

In a second experiment, we varied the initial conditions of the excitation pump (by changing the angle of the polarization) to investigate how these affect the spin pattern formation. At low power, $P \simeq 80\ \mu W$, we observed polarization precession in the 3 components of the Stokes vector, depending on the angle of the initial polarization of the excitation beam (Fig 6.9).

The Stokes vector components for higher excitation power (P=1 mW) are showed in 6.10. At this power, a soliton doublet appears as in the previous experiment where the excitation beam was vertically polarized (Fig 6.6). Cherenkov radiation is also observed as expected. The Cherenkov radiation shows polarization precession, confirming its linear nature discussed in chapter 5. Spin domains

are observed depending on the excitation polarization. We notice clear domains in the S_2^* component for the horizontal and antidiagonal (-45°) excitation. Precession in the circular component is still present, especially for the diagonal excitation. We can observe precessing domains in the rest of polarization components and excitation angles, similar to the case of S_3^* with a vertical polarization pump.

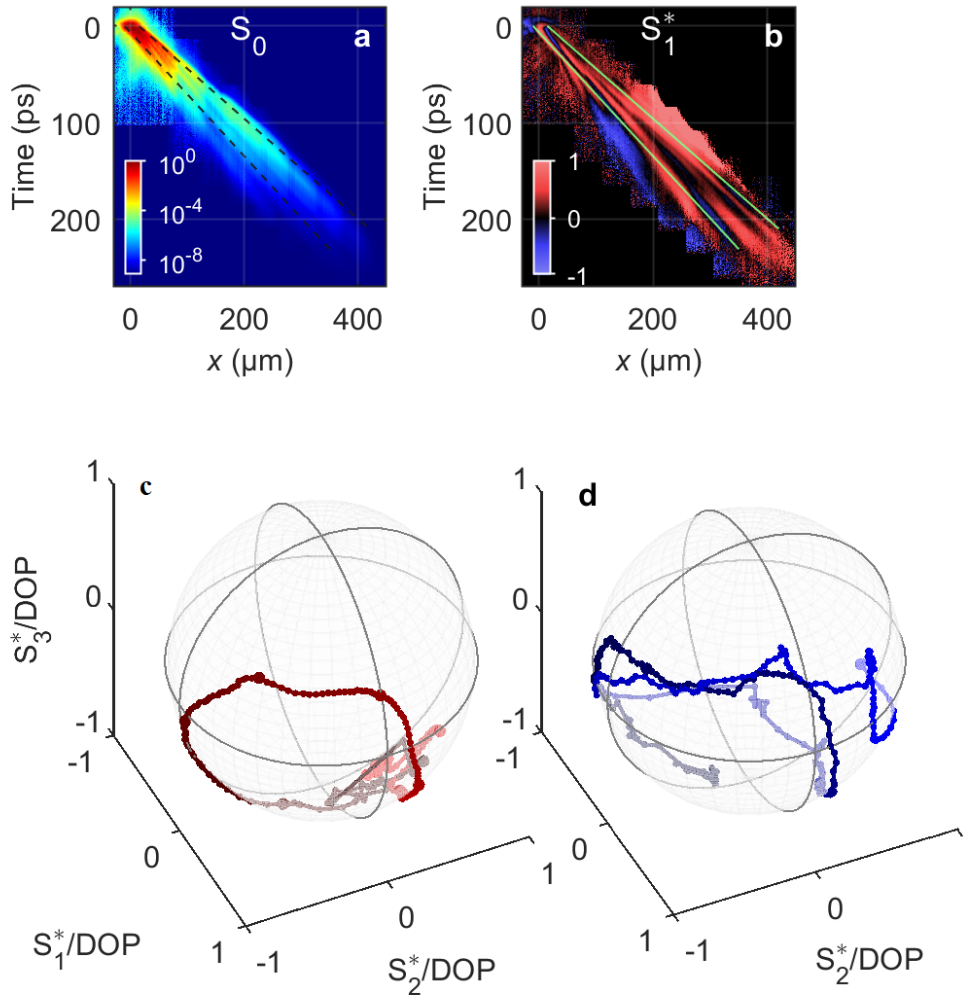

Figure 6.8: P=3.1 mW. (a,b) Show the total intensity (S_0) and linear polarization (S_1^*) Stokes components. Traces 1 and 2 showed as green lines (dotted lines in a) show the spatial points of the soliton profile where we measured the values of the Stokes vector for the reconstruction in panels c and d. (c,d) Evolution of the Stokes vector for traces 1 (c) and 2 (d) plotted on the surface of the Poincaré sphere. The brighter (dimmer) lines correspond to the evolution of the vector on the front (back) surface of the sphere. The length of the experimental Stokes vectors is normalised to unity. [204]

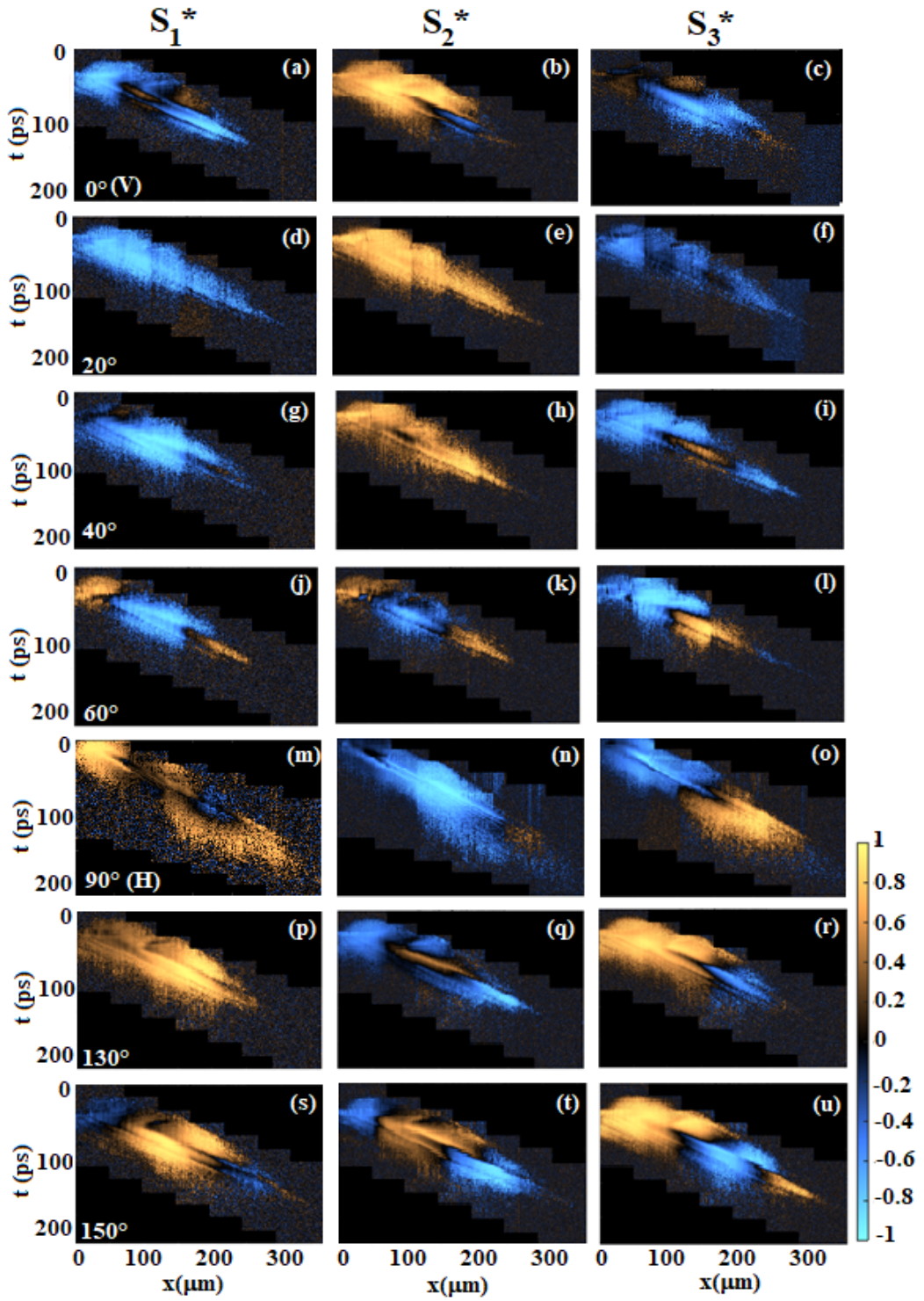

Figure 6.9: Polarization Stokes components (S_1^*, S_2^* and S_3^*) for low power excitation P=80 μW. The initial linear polarization excitation is rotated different angles with respect to the vertical (TE), each row has the same angle of excitation which is showed in white on the S_1^* panel. Polarization precession is present for all the angles.

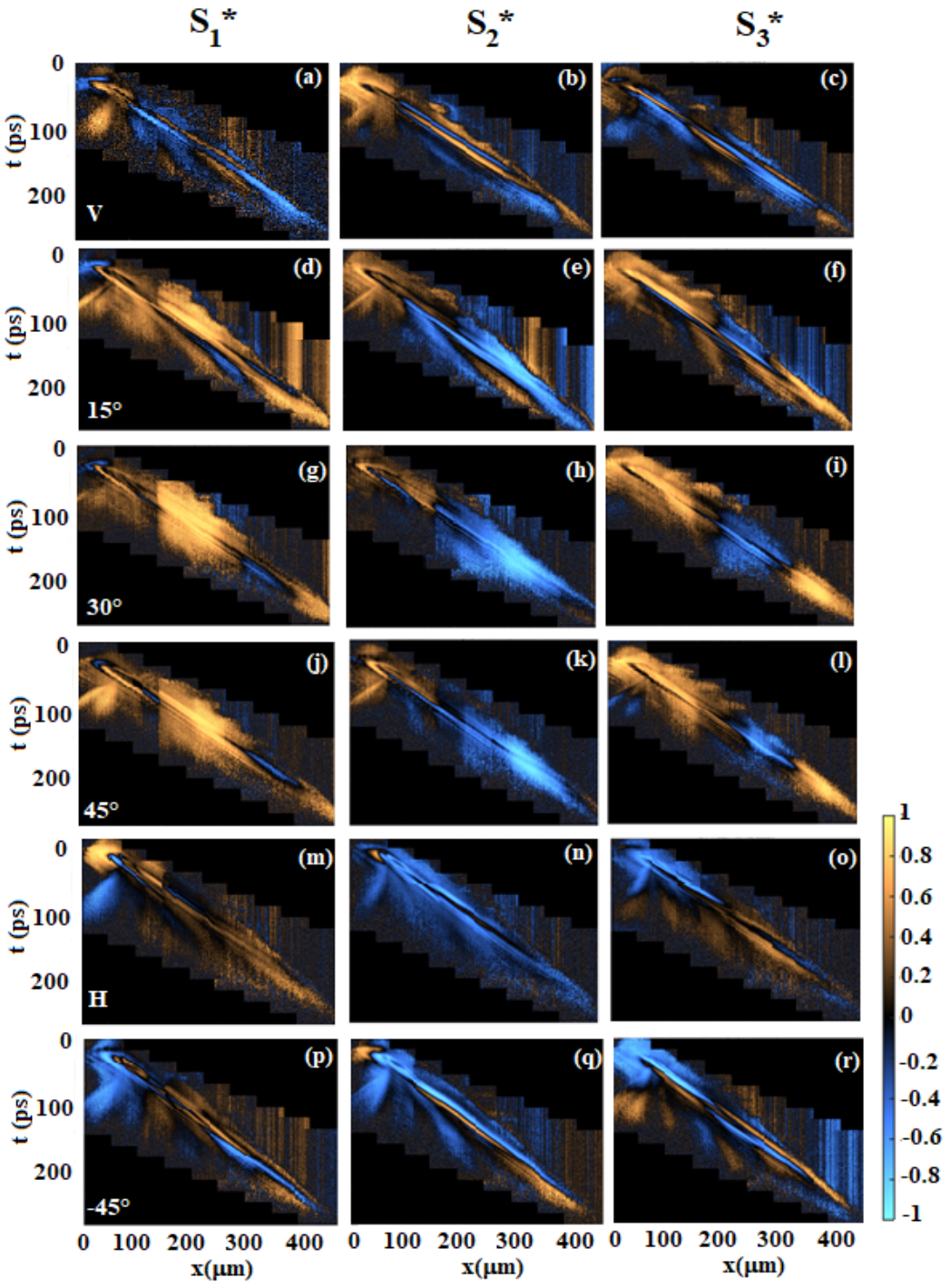

Figure 6.10: Polarization Stokes components (S_1^*, S_2^* and S_3^*) for intermediate power excitation P=1.0 mW. The initial linear polarization excitation is rotated different angles with respect to the vertical (TE), each row has the same angle of excitation which is showed in white on the S_1^* panel. Soliton formation and Cherenkov radiation is present for all the excitation polarizations at this power. Spin domains are formed depending on the excitation polarization.

6.4 Theoretical Model and Simulations

To develop a theoretical model that could reproduce the polarization dynamics observed experimentally, we used the exciton wave function in the circular polarization basis: $\chi = (\chi_+, \chi_-)^T$ and the coupled spinor macroscopic cavity photon field: $\psi = (\psi_+, \psi_-)^T$.

We consider an infinite rectangular potential well width w_y and a photon wave function of the form $\psi_\pm(t,r) = \sqrt{2/w_y}cos(\pi y/w_y)exp(-i\varepsilon_y t/\hbar)\psi_\pm(t,x)$. Then, considering the 1D nature of the microwire, the coupled equations for the polariton envelope $\psi_\pm(t,x)$ propagating in the x-direction are given by:

$$i\hbar\frac{\partial\psi_\pm}{\partial t} = [-\frac{\hbar^2}{2m}\frac{\partial^2}{\partial x^2}+\Delta-i\frac{\hbar\Gamma}{2}]\psi_\pm+(\Sigma_x\mp i\delta)\psi_\mp+\frac{\hbar\Omega}{2}\chi_\pm+E_\pm e^{-i(\omega_p t-k_p x-ix^2/2w_x^2-it^2/2w_t^2)} \tag{6.5}$$

$$i\hbar\frac{\partial\chi_\pm}{\partial t} = [\alpha_1|\chi_\pm|^2+\alpha_2|\chi_\mp|^2 I\frac{\hbar\Gamma_\chi}{2}]\chi+\frac{\hbar\Omega}{2}\psi_\pm \tag{6.6}$$

Where m is the cavity photons effective mass (which we took as $m = 5{\cdot}10^{-5}m_0$ for modelling); Δ is the exciton photon detuning (measured as -2 meV in our microwire); δ gives the splitting of the diagonal polarizations due to electronic and optical anisotropy (for modelling, $\delta = 20\mu eV$); Γ is cavity photon decay rates corresponding to photons leaking from the cavity (given by the inverse of the polariton lifetime: $1/30\ ps^{-1}$); Γ_χ is the exciton decay rates corresponding to nonradiative dephasing processes (for the simulations presented in this chapter, H. Sigurdsson et al. used $\Gamma_\chi = 0.066\ ps^{-1} = 2\Gamma$); $\hbar\Omega$ is the Rabi splitting (4.12 meV for our sample and simulations).

$\Sigma_x = -B(\partial_x^2+\pi^2/w_y^2)$ is the real space TE-TM operator along the wire where B is a splitting constant. For modelling we used $B = 12\ \mu eV\mu m^2$.

The parameter α_1 is the interaction constant in the triplet configuration (parallel spin), we used $\alpha_1 = 2\ \mu eV\ \mu m$. α_2 is the interaction constant in the singlet configuration (opposite spin), we used $\alpha_2 = 0.1\alpha_1$ for the simulations showed in 6.11.

The resonant optical pumping is described by the last term of equation 6.5, where w_x and w_t are the spatial and temporal pulse width respectively; $\hbar w_p$ is the pump energy; and k_p the pulse wavevector along the microcavity wire.

6.4.1 Simulations

Simulations of the polarization dynamics for the case of vertical (TE) polarization excitation were carried out. To fit the experimental results, (together with the parameters described in the previous subsection) we used: $E_+ = E_-$ and $E_- = 2.65e^{i\phi}E_0$ where $\phi = 1.9$ and E_0 denotes the overall amplitude of the beam.

Simulations (Fig 6.11) successfully reproduce the polarization behaviour observed in the experiment (Fig 6.3, 6.5 and 6.7) at different pump powers.

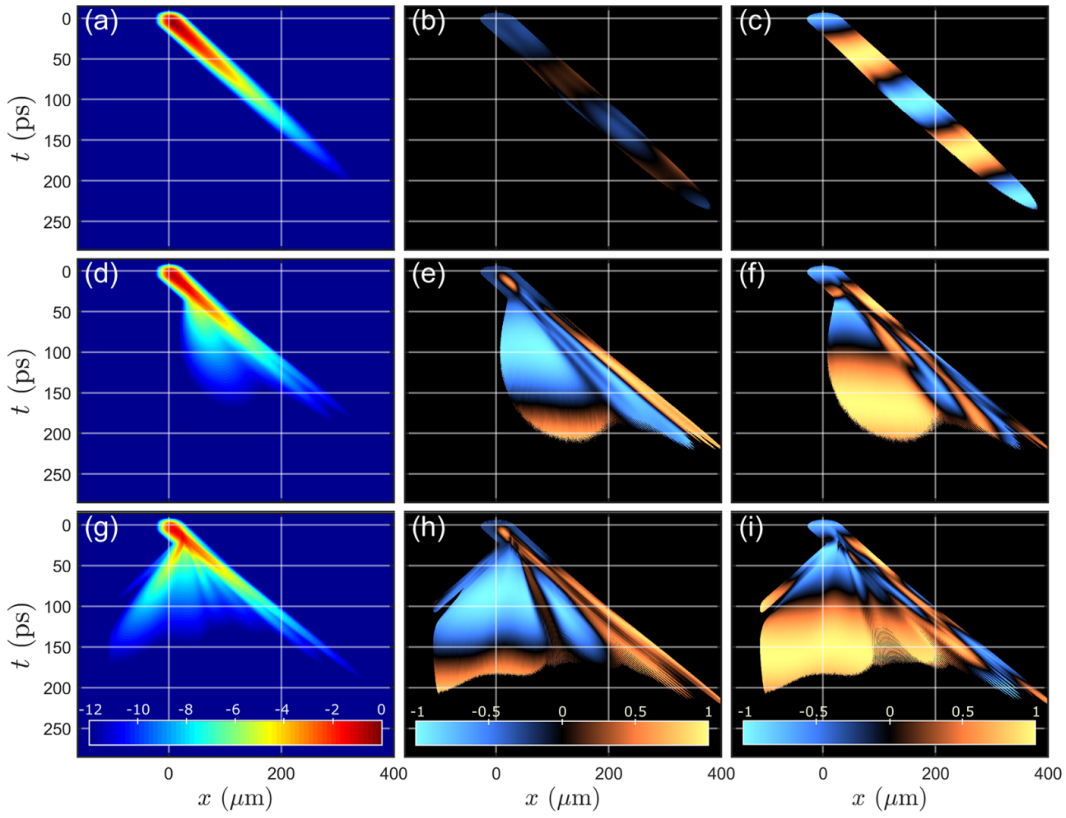

Figure 6.11: Simulations of the polarization dynamics of a polariton pulse for 3 different excitation powers. $E_0 = 0.4$, 1.5, 2.0 meV $\mu m^{1/2}$ respectively for top, middle, and bottom panel rows. (a, d, g) Total intensity S_0 (logarithmic scale) and degrees of linear, S_1^* (b, e, h), and circular, S_3^* (c, f, i) polarizations. [204]

We note that at low powers, the oscillations in the linear polarization S_1^* do not arise from the effective magnetic field induced by the TE-TM splitting since it is oriented in the x direction, but from the additional splitting δ occurring between

the diagonal polarizations. At higher powers, the formation of the soliton doublet, Cherenkov radiation and polarization domains are reproduced by the theoretical model.

In addition, we noticed that the initial formation of solitons is mainly a scalar effect. The polarization domain pattern due to the nonlinear pseudomagnetic field, appears on top of the solitonic total-intensity pattern (see Supplementary Material of [204]). This is also supported experimentally as soliton formation is not affected by the initial excitation polarization angle (Fig 6.10).

6.5 Conclusion

In this chapter, I have presented the study of the polarization of bright solitons propagating in a microwire by resolving the full Stokes vector of the emission. We observed nonlinear spin dynamics of polariton wavepackets for different excitation powers and initial polarization angles.

At low excitation powers, we measured polarization precession during the propagation of the wavepacket. This initial spin precession occurs due to an effective magnetic field induced by splittings between linearly polarized components.

We noticed that both magnitude and direction of the total effective magnetic field inside the cavity, and therefore the speed of the polarization precession, depends on the polariton density.

At higher densities (higher excitation powers) spin domains appear. The extra pump-induced magnetic field coupled with anisotropic spin interactions and finite ellipticity of the pump beam creates an imbalance in the two polariton eigen-spin populations, resulting in formation of spatially separated polarisation domains. Due to the finite polariton lifetime, once the polariton density (and hence the effective magnetic field) drops, polarization domains remain.

We observed that the polarization domains experience little dispersion over the propagation distance, it is likely that solitons, due to their non-spreading nature, are helping to preserve the spin domains. However, we should remark that the soliton formation is mainly a scalar effect and that the polarization domains observed happen on top of the total intensity pattern. As showed in the results for different pump polarization angles, soliton formation is independent of the excitation polarization.

These results open the possibility for further fundamental studies, such as description of the mechanisms involved in the formation of domain walls. From a technological point of view, the polarization domains in polariton conservative solitons could be used for nonbinary information encoding and transfer.

Chapter 7

Conclusions and future plans

This thesis has been devoted to the study of polariton propagation in waveguides and microwires, both of them promising building blocks for future circuit applications.

In Chapter 4, we investigated the nonlinear amplification of polariton pulses in waveguides. We showed that the gain is big enough to overcome losses and obtained a maximum gain of 4.3 dB. We observed nonlinear modulation and gain at the same time in the same device. By comparison with a numerical model we explained the observed combination of gain and nonlinearity as a result of the amplification of the polariton field by stimulated scattering from an incoherent continuous wave reservoir and showed that the main source for saturation of the gain is the depletion of the mentioned reservoir.

We propose two possible ways to increase the amount of gain, the first one is by using shorter pulses as the depletion of the reservoir is less. The second one is the use of a ridge edge waveguide, around 4 μm wide, to confine the propagating polaritons and pump region in the transversal direction and therefore achieve a bigger overlap of the pulses and the gain.

In chapter 5 and chapter 6 we studied the formation of conservative bright solitons in microwires and its accompanying effects. In chapter 5 we showed that the emission of backward Cherenkov radiation by the solitons is possible due to the particular shape of the microcavity dispersion, which has regions of positive and negative group velocity. We showed that the velocity of the Cherenkov radiation is determined by the energy, momentum and power of the excitation beam. We experimentally measured polariton-soliton pulse compression, pulse breaking and emission of the intense backward Cherenkov radiation. We showed

that the Cherenkov radiation appears after a power threshold and that it can be seen as an independent signature of soliton formation in microcavity wires.

Chapter 6 was dedicated to study the polarization of the observed bright solitons in microwires. We measured polarization precession at low powers and domain formation at higher powers. By comparison with the theoretical model, we explain the polarization domain formation as a result of spin-dependent polariton-polariton interactions and a spin imbalance in the initial polariton wavepackets inducing an out of plane effective magnetic field. We observed that the polarization domains appear over the total intensity pattern and conclude that even though soliton formation is mainly a scalar effect it likely helps to preserve the polarization domains over the propagation distance.

In the context of technological applications, the work carried out in waveguides and microwires open possibilities for polaritonic devices. The observation of strong gain and nonlinearity in waveguides make them a promising candidate for future low-power all-optical information processors where control over losses is an important feature. In addition, Ciers et al. recently reported polariton propagation in III-nitride slab waveguides [216], which could potentially work at room temperatures, facilitating their use in optical circuits.

On the other hand, microwires could also be used for information processing circuits [203] where the studied Cherenkov radiation could play an important role as it already does in fibre optics [130]. The observed solitons point out the possibility of using microwires for information transmission and soliton-based logical gates [7]. While the observation of spin domains in the propagating solitons may be used for nonbinary encoding and transfer.

In addition to the possible technological applications, the present investigation is also relevant from a fundamental point of view. The future possibility of studying Parity-Time symmetry in polariton waveguides, arises from the observation of gain and losses in combination with strong nonlinearity. And, while the study of solitons and its properties is already a matter of pure research, the observed polarization domains could be the starting point for the study of fundamental processes such as domain wall formation.

The study of topological polaritons and solitons is another possibility for future investigation. Topological polaritons arise when single photons and excitons are combined under certain conditions, producing nontrivial polaritonic bands with chiral edge modes. As proposed in [217], a dielectric slab waveguide could be used to confine the photonic modes allowing the formation of topological polaritons. As the study of polariton topological insulators is becoming a reality [23], topological solitons are expected to appear [218]. They would form

from wavepackets of topological edge modes, due to the strong nonlinearity in polariton systems [219].

Bibliography

[1] C. Weisbuch, M. Nishioka, A. Ishikawa, and Y. Arakawa, "Observation of the Coupled Exciton-Photon Mode Splitting in a Semiconductor Microcavity," *Physical Review Letters*, vol. 69, no. 23, pp. 3314–3317, 1992.

[2] C. Ciuti and I. Carusotto, "Quantum fluid effects and parametric instabilities in microcavities," *physica status solidi (b)*, vol. 242, no. 11, pp. 2224–2245, 2005.

[3] A. Amo, J. Lefrère, S. Pigeon, C. Adrados, C. Ciuti, I. Carusotto, R. Houdré, E. Giacobino, and A. Bramati, "Superfluidity of polaritons in semiconductor microcavities," *Nature Physics*, vol. 5, pp. 805–810, 2009.

[4] J. Kasprzak, M. Richard, S. Kundermann, A. Baas, P. Jeambrun, J. M. J. Keeling, F. M. Marchetti, M. H. Szymańska, R. André, J. L. Staehli, V. Savona, P. B. Littlewood, B. Deveaud, and L. S. Dang, "Bose-Einstein condensation of exciton polaritons," *Nature*, vol. 443, no. 28, pp. 409–414, 2006.

[5] C. Schneider, A. Rahimi-Iman, N. Y. Kim, J. Fischer, I. G. Savenko, M. Amthor, M. Lermer, A. Wolf, L. Worschech, V. D. Kulakovskii, I. A. Shelykh, M. Kamp, S. Reitzenstein, A. Forchel, Y. Yamamoto, and S. Höfling, "An electrically pumped polariton laser," *Nature*, vol. 497, pp. 348–352, 2013.

[6] C. Antón, T. C. H. Liew, J. Cuadra, M. D. Martín, P. S. Eldridge, Z. Hatzopoulos, G. Stavrinidis, P. G. Savvidis, and L. Viña, "Quantum reflections and shunting of polariton condensate wave trains: Implementation of a logic AND gate," *Phys. Rev. B*, vol. 88, p. 245307, Dec 2013.

[7] E. Cancellieri, J. K. Chana, M. Sich, D. N. Krizhanovskii, M. S. Skolnick, and D. M. Whittaker, "Logic gates with bright dissipative polariton solitons in Bragg cavity systems," *Phys. Rev. B*, vol. 92, p. 174528, Nov 2015.

[8] A. Amo, T. C. H. Liew, C. Adrados, R. Houdré, E. Giacobino, A. V. Kavokin, and A. Bramati, "Exciton-polariton spin switches," *Nature Photonics*, vol. 4, no. 6, pp. 361–366, 2010.

[9] S. I. Pekar, "Theory of electromagnetic waves in a crystal in which excitons arise," *J. Exp. Teor. Fiz. USSR*, no. 33, pp. 1022–1036, 1957.

[10] J. J. Hopfield, "Theory of the contribution of excitons to the complex dielectric constant of crystals," *Physical Review*, vol. 112, no. 5, pp. 1555–1567, 1958.

[11] L. C. Andreani, "Optical transitions, excitons, and polaritons in bulk and low-dimensional semiconductor structures," in *Confined Electrons and Photons* (W. C. Burstein E., ed.), vol. 340 of *NATO ASI Series (Series B: Physics)*, Boston, MA: Springer, 1995.

[12] D. Fröhlich, E. Mohler, and P. Wiesner, "Observation of Exciton Polariton Dispersion in CuCl," *Phys. Rev. Lett.*, vol. 26, pp. 554–556, Mar 1971.

[13] B. Hönerlage, R. Lévy, J. Grun, C. Klingshirn, and K. Bohner, "The dispersion of excitons, polaritons and biexcitons in direct-gap semiconductors," *Physics Reports*, vol. 124, no. 3, pp. 161 – 253, 1985.

[14] K. Ogawa, T. Katsuyama, and H. Nakamura, "Time-of-flight measurement of excitonic polaritons in a GaAs/AlGaAs quantum well," *Applied Physics Letters*, vol. 53, no. 12, p. 1077, 1988.

[15] P. M. Walker, L. Tinkler, M. Durska, D. M. Whittaker, I. J. Luxmoore, B. Royall, D. N. Krizhanovskii, M. S. Skolnick, I. Farrer, and D. A. Ritchie, "Exciton polaritons in semiconductor waveguides," *Applied Physics Letters*, vol. 102, p. 012109, 2013.

[16] A. Amo, S. Pigeon, C. Adrados, J. Lefrère, C. Ciuti, I. Carusotto, R. Houdré, A. Bramati, and E. Giacobino, "Quantum fluid properties of polaritons in semiconductor microcavities," *Journal of Modern Optics*, vol. 57, no. 19, pp. 1900–1907, 2010.

[17] A. Kavokin, G. Malpuech, and M. Glazov, "Optical Spin Hall Effect," *Phys. Rev. Lett.*, vol. 95, p. 136601, Sep 2005.

[18] P. G. Savvidis, J. J. Baumberg, R. M. Stevenson, M. S. Skolnick, D. M. Whittaker, and J. S. Roberts, "Angle-Resonant Stimulated Polariton Amplifier," *Physical Review Letters*, vol. 84, no. 7, pp. 1547–1550, 2000.

[19] M. Sich, D. N. Krizhanovskii, M. S. Skolnick, A. V. Gorbach, R. Hartley, D. V. Skryabin, E. A. Cerda-Méndez, K. Biermann, R. Hey, and P. V. Santos, "Observation of bright polariton solitons in a semiconductor microcavity," *Nature photonics*, vol. 6, no. January, pp. 50–55, 2011.

[20] L. A. Smirnov, D. A. Smirnova, E. A. Ostrovskaya, and Y. S. Kivshar, "Dynamics and stability of dark solitons in exciton-polariton condensates," *Phys. Rev. B*, vol. 89, p. 235310, Jun 2014.

[21] G. Roumpos, M. D. Fraser, A. Löffler, S. Höfling, A. Forchel, and Y. Yamamoto, "Single vortex-antivortex pair in an exciton-polariton condensate," *Nature Physics*, vol. 7, pp. 129–133, 2010.

[22] C. E. Whittaker, E. Cancellieri, P. M. Walker, B. Royall, L. E. Tapia Rodriguez, E. Clarke, D. M. Whittaker, H. Schomerus, M. S. Skolnick, and D. N. Krizhanovskii, "Effect of photonic spin-orbit coupling on the topological edge modes of a Su-Schrieffer-Heeger chain," *Phys. Rev. B*, vol. 99, p. 081402, Feb 2019.

[23] S. Klembt, T. H. Harder, O. A. Egorov, K. Winkler, R. Ge, M. A. Bandres, M. Emmerling, L. Worschech, T. C. H. Liew, M. Segev, C. Schneider, and S. Höfling, "Exciton-polariton topological insulator," *Nature*, vol. 562, pp. 552–556, 2018.

[24] L. Ferrier, E. Wertz, R. Johne, D. D. Solnyshkov, P. Senellart, I. Sagnes, A. Lemaître, G. Malpuech, and J. Bloch, "Interactions in confined polariton condensates," *Phys. Rev. Lett.*, vol. 106, p. 126401, Mar 2011.

[25] G. H. Wannier, "The structure of electronic excitation levels in insulating crystals," *Physical Review*, vol. 52, no. 3, p. 191, 1937.

[26] A. Kavokin, J. J. Baumberg, G. Malpuech, and F. P. Laussy, *Microcavities*. Oxford Science Publications, 2007.

[27] R. Houdré, C. Weisbuch, R. Stanley, U. Oesterle, P. Pellandini, and M. Ilegems, "Measurement of cavity-polariton dispersion curve from angle-resolved photoluminescence experiments," *Physical Review Letters*, vol. 73, no. 15, p. 2043, 1994.

[28] D. Whittaker, P. Kinsler, T. Fisher, M. Skolnick, A. Armitage, A. Afshar, M. Sturge, and J. Roberts, "Motional narrowing in semiconductor microcavities," *Physical review letters*, vol. 77, no. 23, p. 4792, 1996.

[29] F. Li, *Fabrication and Characterization of ZnO-based Microcavities Working in the Strong Coupling Regime: Polariton Laser*. PhD thesis, Université de Nice-Sophia Antipolis, 2013.

[30] P. Y. Yu and M. Cardona, *Fundamentals of Semiconductors*. Springer-Verlag, second ed., 1999.

[31] D. Sarchi, *Bose-Einstein Condensation of Microcavity Polaritons*. PhD thesis, Ecole Polytechnique Fédérale de Lausanne, 2007.

[32] M. S. Skolnick, T. A. Fisher, and D. M. Whittaker, "Strong coupling phenomena in quantum microcavity structures," *Semiconductor Science and Technology*, vol. 13, no. 7, pp. 645–669, 1998.

[33] O. El Daïf, *0D Microcavity Polaritons Trapping Light-Matter Quasiparticles*. PhD thesis, Ecole Polytechnique Fédérale de Lausanne, 2007.

[34] B. E. A. Saleh and M. C. Teich, *Fundamentals of photonics*, vol. 32 of *Wiley Series in Pure and Applied Optics*. Wiley, second ed., 2007.

[35] B. Nelsen, G. Liu, M. Steger, D. W. Snoke, R. Balili, K. West, and L. Pfeiffer, "Dissipationless flow and sharp threshold of a polariton condensate with long lifetime," *Phys. Rev. X*, vol. 3, p. 041015, Nov 2013.

[36] H. Soda, K. Iga, C. Kitahara, and Y. Suematsu, "GaInAsP/InP Surface Emitting Injection Lasers," *Japanese Journal of Applied Physics*, vol. 18, no. 12, p. 2329, 1979.

[37] J. Orton and T. Foxon, *Molecular Beam Epitaxy: a short history*. Oxford University Press, 2015.

[38] U. Oesterle, R. P. Stanley, and R. Houdré, "MBE growth of high finesse microcavities," *physica status solidi (b)*, vol. 242, no. 11, pp. 2157–2166, 2005.

[39] K. Biermann, E. A. Cerda-Méndez, M. Höricke, P. V. Santos, and R. Hey, "Controlled growth of exciton-polariton microcavities using in situ spectral reflectivity measurements," *Journal of Crystal Growth*, vol. 323, no. 1, pp. 56–59, 2011.

[40] P. Uusimaa, A. Rinta-Mykky, S. Orsila, A. Salokatve, and M. Pessa, "MBE growth of monolithic MgZnSSe/ZnSSe/CdZnSe microcavity LED structures," *Journal of Crystal Growth*, vol. 184-185, pp. 783 – 786, 1998.

[41] L. F. Lastras-Martínez, E. Cerda-Méndez, N. Ulloa-Castillo, R. Herrera-Jasso, L. E. Tapia-Rodríguez, O. Ruiz-Cigarrillo, R. Castro-García, K. Biermann, and P. V. Santos, "Microscopic optical anisotropy of exciton-polaritons in a GaAs-based semiconductor microcavity," *Phys. Rev. B*, vol. 96, p. 235306, Dec 2017.

[42] K. Regiski, J. Muszalski, M. Bugajski, T. Ochalski, J. Kubica, M. Zbroszczyk, J. Ktcki, and J. Ratajczak, ""MBE growth of planar microcavities with distributed Bragg reflectors"," *Thin Solid Films*, vol. 367, no. 1, pp. 290 – 294, 2000.

[43] A. C. Jones and M. L. Hitchman, *Chemical Vapour Deposition. Precursors, Processes and Applications*. Royal Society of Chemistry, 2009.

[44] M. Young, *Optics and Lasers*. Springer Series in Optical Sciences, Springer-Verlag Berlin Heidelberg, second ed., 1984.

[45] L. Tinkler, *Optical nonlinearities in semiconductor polariton waveguides*. PhD thesis, University of Sheffield, 2015.

[46] M. A. Mohammad, M. Muhammad, S. K. Dew, and M. Stepanova, *Fundamentals of Electron Beam Exposure and Development*. Springer Science and Business Media, 2011.

[47] D. Ballarini, *Dynamics of microcavity polaritons at the non-linear regime crossover*. PhD thesis, Universidad Autonoma de Madrid, 2008.

[48] V. Savona, A. Quattropani, L. Andreani, and P. Schwendimann, "Quantum well excitons in semiconductor microcavities : unified treatment of weak and strong coupling regimes," *Solid State Communications*, vol. 93, pp. 733–739, 1995.

[49] S. Schmitt-Rink, D. S. Chemla, and D. A. B. Miller, "Theory of transient excitonic optical nonlinearities in semiconductor quantum-well structures," *Physical Review B*, vol. 32, no. 10, pp. 6601–6609, 1985.

[50] I. A. Shelykh, A. V. Kavokin, and G. Malpuech, "Spin dynamics of exciton polaritons in microcavities," *Physica Status Solidi (B) Basic Research*, vol. 242, no. 11, pp. 2271–2289, 2005.

[51] G. Panzarini, L. C. Andreani, A. Armitage, D. Baxter, M. S. Skolnick, V. N. Astratov, J. S. Roberts, A. V. Kavokin, M. R. Vladimirova, and M. A. Kaliteevski, "Exciton-light coupling in single and coupled semiconductor microcavities: Polariton dispersion and polarization splitting," *Phys. Rev. B*, vol. 59, pp. 5082–5089, Feb 1999.

[52] M. Z. Maialle, E. A. de Andrada e Silva, and L. J. Sham, "Exciton spin dynamics in quantum wells," *Phys. Rev. B*, vol. 47, pp. 15776–15788, Jun 1993.

[53] F. Manni, K. G. Lagoudakis, T. K. Paraïso, R. Cerna, Y. Léger, T. C. H. Liew, I. A. Shelykh, A. V. Kavokin, F. Morier-Genoud, and B. Deveaud-Plédran, "Spin-to-orbital angular momentum conversion in semiconductor microcavities," *Phys. Rev. B*, vol. 83, p. 241307, Jun 2011.

[54] R. Hivet, H. Flayac, D. D. Solnyshkov, D. Tanese, T. Boulier, D. Andreoli, E. Giacobino, J. Bloch, A. Bramati, G. Malpuech, and A. Amo, "Half-solitons in a polariton quantum fluid behave like magnetic monopoles," *Nature Physics*, vol. 8, pp. 724–728, 2012.

[55] A. Kuther, M. Bayer, T. Gutbrod, A. Forchel, P. A. Knipp, T. L. Reinecke, and R. Werner, "Confined optical modes in photonic wires," *Physical Review B*, vol. 58, no. 23, pp. 15744–15748, 1998.

[56] R. Paschotta, *Field Guide to Optical Fiber Technology*. SPIE Digital Library, 2010.

[57] E. Wertz, L. Ferrier, D. D. Solnyshkov, R. Johne, D. Sanvitto, A. Lemaître, I. Sagnes, R. Grousson, A. V. Kavokin, P. Senellart, G. Malpuech, and J. Bloch, "Spontaneous formation and optical manipulation of extended polariton condensates," *Nature Physics*, vol. 6, no. 11, pp. 860–864, 2010.

[58] A. I. Tartakovskii, V. D. Kulakovskii, A. Forchel, and J. P. Reithmaier, "Exciton-photon coupling in photonic wires," *Physical Review B*, vol. 57, no. 12, pp. R6807–R6810, 1998.

[59] T. B. Norris, J.-K. Rhee, C.-Y. Sung, Y. Arakawa, M. Nishioka, and C. Weisbuch, "Time-resolved vacuum Rabi oscillations in a semiconductor quantum microcavity," *Phys. Rev. B*, vol. 50, pp. 14663–14666, Nov 1994.

[60] V. Savona, *Fifteen years of microcavity polaritons*, pp. 1–31. Wiley-VCH, 2008.

[61] F. Tassone, C. Piermarocchi, V. Savona, A. Quattropani, and P. Schwendimann, "Bottleneck effects in the relaxation and photoluminescence of microcavity polaritons," *Phys. Rev. B*, vol. 56, pp. 7554–7563, Sep 1997.

[62] C. Ciuti, V. Savona, C. Piermarocchi, A. Quattropani, and P. Schwendimann, "Role of the exchange of carriers in elastic exciton-exciton scattering in quantum wells," *Physical Review B*, vol. 58, pp. 7926–7933, Sep 1998.

[63] M. Vladimirova, S. Cronenberger, D. Scalbert, K. V. Kavokin, A. Miard, A. Lemaître, J. Bloch, D. Solnyshkov, G. Malpuech, and A. V. Kavokin, "Polariton-polariton interaction constants in microcavities," *Phys. Rev. B*, vol. 82, p. 075301, Aug 2010.

[64] M. M. Glazov, H. Ouerdane, L. Pilozzi, G. Malpuech, A. V. Kavokin, and A. D'Andrea, "Polariton-polariton scattering in microcavities: A microscopic theory," *Physical Review B*, vol. 80, p. 155306, Oct 2009.

[65] C. Ciuti, P. Schwendimann, and A. Quattropani, "Parametric luminescence of microcavity polaritons," *Physical Review B*, vol. 63, p. 041303, Jan 2001.

[66] C. Ciuti, P. Schwendimann, and A. Quattropani, "Theory of polariton parametric interactions in semiconductor microcavities," *Semiconductor Science and Technology*, vol. 18, no. 10, p. S279, 2003.

[67] F. Boeuf, R. André, R. Romestain, L. Si Dang, E. Péronne, J. F. Lampin, D. Hulin, and A. Alexandrou, "Evidence of polariton stimulation in semiconductor microcavities," *Phys. Rev. B*, vol. 62, pp. R2279–R2282, Jul 2000.

[68] A. I. Tartakovskii, M. S. Skolnick, D. N. Krizhanovskii, V. D. Kulakovskii, R. M. Stevenson, R. Butté, J. J. Baumberg, D. M. Whittaker, and J. S. Roberts, "Stimulated polariton scattering in semiconductor microcavities: New physics and potential applications," *Advanced Materials*, vol. 13, no. 22, pp. 1725–1730, 2001.

[69] D. V. Vishnevsky and F. Laussy, "Effective attractive polariton-polariton interaction mediated by an exciton reservoir," *Phys. Rev. B*, vol. 90, p. 035413, Jul 2014.

[70] M. Maragkou, A. Grundy, T. Ostatnickỳ, and P. Lagoudakis, "Longitudinal optical phonon assisted polariton laser," *Applied Physics Letters*, vol. 97, no. 11, p. 111110, 2010.

[71] L. Orosz, F. Réveret, F. Médard, P. Disseix, J. Leymarie, M. Mihailovic, D. Solnyshkov, G. Malpuech, J. Zuniga-Pérez, F. Semond, M. Leroux, S. Bouchoule, X. Lafosse, M. Mexis, C. Brimont, and T. Guillet, "LO-phonon-assisted polariton lasing in a ZnO-based microcavity," *Phys. Rev. B*, vol. 85, p. 121201, Mar 2012.

[72] P. Corfdir, J. Levrat, G. Rossbach, R. Butté, E. Feltin, J.-F. Carlin, G. Christmann, P. Lefebvre, J.-D. Ganière, N. Grandjean, and B. Deveaud-Plédran, "Impact of biexcitons on the relaxation mechanisms of polaritons in iii-nitride based multiple quantum well microcavities," *Phys. Rev. B*, vol. 85, p. 245308, Jun 2012.

[73] R. Boyd, *Nonlinear Optics*. Academic Press, 2008.

[74] R. M. Stevenson, V. N. Astratov, M. S. Skolnick, D. M. Whittaker, M. Emam-Ismail, A. I. Tartakovskii, P. G. Savvidis, J. J. Baumberg, and

J. S. Roberts, "Continuous Wave Observation of Massive Polariton Redistribution by Stimulated Scattering in Semiconductor Microcavities," *Phys. Rev. Lett.*, vol. 85, pp. 3680–3683, Oct 2000.

[75] H. Deng, G. Weihs, C. Santori, J. Bloch, and Y. Yamamoto, "Condensation of Semiconductor Microcavity Exciton Polaritons," *Science*, vol. 298, no. 5591, pp. 199–202, 2002.

[76] O. A. Egorov, D. V. Skryabin, and F. Lederer, "Parametric polariton solitons in coherently pumped semiconductor microcavities," *Phys. Rev. B*, vol. 84, p. 165305, Oct 2011.

[77] S. Kundermann, M. Saba, C. Ciuti, T. Guillet, U. Oesterle, J. L. Staehli, and B. Deveaud, "Coherent Control of Polariton Parametric Scattering in Semiconductor Microcavities," *Phys. Rev. Lett.*, vol. 91, p. 107402, Sep 2003.

[78] W. Langbein, "Spontaneous parametric scattering of microcavity polaritons in momentum space," *Phys. Rev. B*, vol. 70, p. 205301, Nov 2004.

[79] R. Butté, M. S. Skolnick, D. M. Whittaker, D. Bajoni, and J. S. Roberts, "Dependence of stimulated scattering in semiconductor microcavities on pump power, angle, and energy," *Phys. Rev. B*, vol. 68, p. 115325, Sep 2003.

[80] A. Tartakovskii, D. Krizhanovskii, and V. Kulakovskii, "Polariton-polariton scattering in semiconductor microcavities: Distinctive features and similarities to the three-dimensional case," *Physical Review B*, vol. 62, p. R13298, 11 2000.

[81] J. J. Baumberg, P. G. Savvidis, R. M. Stevenson, A. I. Tartakovskii, M. S. Skolnick, D. M. Whittaker, and J. S. Roberts, "Parametric oscillation in a vertical microcavity: A polariton condensate or micro-optical parametric oscillation," *Phys. Rev. B*, vol. 62, pp. R16247–R16250, Dec 2000.

[82] C. Ciuti, P. Schwendimann, B. Deveaud, and A. Quattropani, "Theory of the angle-resonant polariton amplifier," *Phys. Rev. B*, vol. 62, pp. R4825–R4828, Aug 2000.

[83] M. Saba, C. Ciuti, J. Bloch, V. Thierry-Mieg, R. André, L. S. Dang, S. Kundermann, A. Mura, G. Bongiovanni, J. L. Staehli, and B. Deveaud, "High-temperature ultrafast polariton parametric amplification in semiconductor microcavities," *Nature*, vol. 414, pp. 731–735, 2001.

[84] A. Imamoglu, R. J. Ram, S. Pau, and Y. Yamamoto, "Nonequilibrium condensates and lasers without inversion: Exciton-polariton lasers," *Physical Review A*, vol. 53, no. 6, pp. 4250–4253, 1996.

[85] J. Kasprzak, *Condensation of Exciton Polaritons*. PhD thesis, Université Joseph Fourier - Grenoble 1, 2006.

[86] A. Einstein, "Quantentheorie des einatomigen idealen gases," *Sitzungsberichte der Preussischen Akademie der Wissenshaften*, vol. 2, pp. 261–267, 1924.

[87] A. Griffin, D. W. Snoke, and S. Stringari, *Bose-Einstein condensation*. Cambridge University Press, 1995.

[88] L. Pitaevskii and S. Stringari, *Bose-Einstein condensation*. Oxford University Press, 2003.

[89] A. J. Leggett, "Bose-Einstein condensation in the alkali gases: Some fundamental concepts," *Rev. Mod. Phys.*, vol. 73, pp. 307–356, Apr 2001.

[90] O. Penrose and L. Onsager, "Bose-Einstein Condensation and Liquid Helium," *Phys. Rev.*, vol. 104, pp. 576–584, Nov 1956.

[91] M. H. Anderson, J. R. Ensher, M. R. Matthews, C. E. Wieman, and E. A. Cornell, "Observation of Bose-Einstein Condensation in a Dilute Atomic Vapor," *Science*, vol. 269, no. 5221, pp. 198–201, 1995.

[92] M. R. Andrews, C. G. Townsend, H.-J. Miesner, D. S. Durfee, D. M. Kurn, and W. Ketterle, "Observation of interference between two bose condensates," *Science*, vol. 275, no. 5300, pp. 637–641, 1997.

[93] W. Ketterle, "Nobel lecture: When atoms behave as waves: Bose-Einstein condensation and the atom laser," *Rev. Mod. Phys.*, vol. 74, pp. 1131–1151, Nov 2002.

[94] J. M. Blatt, K. W. Böer, and W. Brandt, "Bose-Einstein Condensation of Excitons," *Phys. Rev.*, vol. 126, pp. 1691–1692, Jun 1962.

[95] S. A. Moskalenko, "Reversible optico-hydrodynamic phenomena in a non ideal exciton gas," *Soviet Physics Solid State*, vol. 4, p. 199, 1996.

[96] J. M. Ziman, *Principles of the Theory of Solids*. Cambridge University Press, 1972.

[97] V. Gergel, R. Kazarinov, and R. Suris, "Optical Properties of an Exciton Condensate in a Semiconductor," *Soviet Physics JETP*, vol. 26, no. 2, 1968.

[98] E. Del Valle, D. Sanvitto, A. Amo, F. P. Laussy, R. André, C. Tejedor, and L. Viña, "Dynamics of the Formation and Decay of Coherence in a Polariton Condensate," *Phys. Rev. Lett.*, vol. 103, p. 096404, Aug 2009.

[99] D. N. Krizhanovskii, E. A. Cerda-Méndez, S. Gavrilov, D. Sarkar, K. Guda, R. Bradley, P. V. Santos, R. Hey, K. Biermann, M. Sich, F. Fras, and M. S. Skolnick, "Effect of polariton-polariton interactions on the excitation spectrum of a nonequilibrium condensate in a periodic potential," *Phys. Rev. B*, vol. 87, p. 155423, Apr 2013.

[100] T. Byrnes, N. Y. Kim, and Y. Yamamoto, "Exciton-polariton condensates," *Nature Physics*, vol. 10, no. 11, pp. 803–813, 2014.

[101] C.-C. Chien, J.-H. She, and F. Cooper, "Mean-field description of pairing effects, bkt physics, and superfluidity in 2d bose gases," *Annals of Physics*, vol. 347, pp. 192 – 206, 2014.

[102] D. N. Krizhanovskii, K. G. Lagoudakis, M. Wouters, B. Pietka, R. A. Bradley, K. Guda, D. M. Whittaker, M. S. Skolnick, B. Deveaud-Plédran, M. Richard, R. André, and L. S. Dang, "Coexisting nonequilibrium condensates with long-range spatial coherence in semiconductor microcavities," *Phys. Rev. B*, vol. 80, p. 045317, Jul 2009.

[103] F. P. Laussy, G. Malpuech, A. Kavokin, and P. Bigenwald, "Spontaneous Coherence Buildup in a Polariton Laser," *Phys. Rev. Lett.*, vol. 93, p. 016402, Jun 2004.

[104] P. Kapitza, "Viscosity of Liquid Helium below the λ-Point," *Nature*, vol. 141, p. 74, 1938.

[105] J. F. Allen and A. D. Misener, "Flow of Liquid Helium II," *Nature*, vol. 141, p. 75, 1938.

[106] F. London, "On the bose-einstein condensation," *Phys. Rev.*, vol. 54, pp. 947–954, Dec 1938.

[107] L. Tisza, "Transport phenomena in helium II," *Nature*, vol. 141, no. 3577, p. 913, 1938.

[108] A. J. Leggett, "Superfluidity," *Reviews of Modern Physics*, vol. 71, no. 2, pp. 318–323, 1999.

[109] R. P. Feynman and M. Cohen, "Energy Spectrum of the Excitations in Liquid Helium," *Phys. Rev.*, vol. 102, pp. 1189–1204, Jun 1956.

[110] L. Landau, "Theory of the Superfluidity of Helium II," *Phys. Rev.*, vol. 60, pp. 356–358, Aug 1941.

[111] I. Carusotto and C. Ciuti, "Probing Microcavity Polariton Superfluidity through Resonant Rayleigh Scattering," *Phys. Rev. Lett.*, vol. 93, p. 166401, Oct 2004.

[112] A. Amo, D. Sanvitto, F. P. Laussy, D. Ballarini, E. d. Valle, M. D. Martin, A. Lemaître, J. Bloch, D. N. Krizhanovskii, M. S. Skolnick, C. Tejedor, and L. Viña, "Collective fluid dynamics of a polariton condensate in a semiconductor microcavity," *Nature*, vol. 457, pp. 291–295, 2009.

[113] E. Cancellieri, T. Boulier, R. Hivet, D. Ballarini, D. Sanvitto, M. H. Szymanska, C. Ciuti, E. Giacobino, and A. Bramati, "Merging of vortices and antivortices in polariton superfluids," *Phys. Rev. B*, vol. 90, p. 214518, Dec 2014.

[114] K. G. Lagoudakis, M. Wouters, M. Richard, A. Baas, I. Carusotto, R. André, L. S. Dang, and B. Deveaud-Plédran, "Quantized vortices in an excitonpolariton condensate," *Nature Physics*, vol. 4, p. 706, 2008.

[115] M. Richard, J. Kasprzak, R. André, R. Romestain, L. S. Dang, G. Malpuech, and A. Kavokin, "Experimental evidence for nonequilibrium Bose condensation of exciton polaritons," *Physical Review B*, vol. 72, no. 20, p. 201301, 2005.

[116] J. S. Russell, "Report on waves," in *14th meeting of the British Association for the Advancement of Science*, pp. 311–390, 1844.

[117] A. S. Davydov, "Solitons in molecular systems," *Physica Scripta*, vol. 20, no. 3-4, p. 387, 1979.

[118] Z. Sinkala, "Soliton/exciton transport in proteins," *Journal of theoretical biology*, vol. 241, no. 4, pp. 919–927, 2006.

[119] L. V. Yakushevich, "Is dna a nonlinear dynamical system where solitary conformational waves are possible?," *Journal of Biosciences*, vol. 26, pp. 305–313, Sep 2001.

[120] K. Dysthe, H. E. Krogstad, and P. Müller, "Oceanic rogue waves," *Annu. Rev. Fluid Mech.*, vol. 40, pp. 287–310, 2008.

[121] F. C. Adams and M. Fatuzzo, "Nonlinear waves and Solitons in Molecular Clouds," *The Astrophysical Journal*, vol. 403, pp. 142–157, 1993.

[122] P. G. Drazin and R. Johnson, *Solitons: an Introduction*. Cambridge University Press, 1989.

[123] J. S. Aitchison, A. M. Weiner, Y. Silberberg, M. K. Oliver, J. L. Jackel, D. E. Leaird, E. M. Vogel, and P. W. E. Smith, "Observation of spatial optical solitons in a nonlinear glass waveguide," *Optics Letters*, vol. 15, no. 9, pp. 471—-473, 1990.

[124] P. Colman, C. Husko, S. Combri, I. Sagnes, C. W. Wong, and A. De Rossi, "Temporal solitons and pulse compression in photonic crystal waveguides," *Nature Photonics*, vol. 4, pp. 862–868, 2010.

[125] L. F. Mollenauer, R. H. Stolen, and J. P. Gordon, "Experimental Observation of Picosecond Pulse Narrowing and Solitons in Optical Fibers," *Phys. Rev. Lett.*, vol. 45, pp. 1095–1098, Sep 1980.

[126] L. F. Mollenauer, M. J. Neubelt, S. G. Evangelides, J. P. Gordon, J. R. Simpson, and L. G. Cohen, "Experimental study of soliton transmission over more than 10,000 km in dispersion-shifted fiber," *Opt. Lett.*, vol. 15, pp. 1203–1205, Nov 1990.

[127] A. Hasegawa, *Optical solitons in fibers: theoretical review*, p. 129. Cambridge Studies in Modern Optics, Cambridge University Press, 1992.

[128] L. F. Mollenauer and R. H. Stolen, "The soliton laser," *Opt. Lett.*, vol. 9, pp. 13–15, Jan 1984.

[129] J. M. Dudley, G. Genty, and S. Coen, "Supercontinuum generation in photonic crystal fiber," *Reviews of modern physics*, vol. 78, no. 4, pp. 1135–1184, 2006.

[130] D. V. Skryabin and A. V. Gorbach, "Colloquium: Looking at a soliton through the prism of optical supercontinuum," *Reviews of Modern Physics*, vol. 82, no. 2, pp. 1287–1299, 2010.

[131] D. Duncan, "John Scott Russell's soliton wave re-created." Heriot-Watt University, 15/11/1995, Available at http://www.ma.hw.ac.uk/solitons/press.htmll.

[132] H. Dobler, "Australia-Morning Glory." Available at http://www.stemme-powergliders.ch/en/flight-reports/australia—morning-glory-cloud/index.html.

[133] K. E. Strecker, G. B. Partridge, A. G. Truscott, and R. G. Hulet, "Formation and propagation of matter-wave soliton trains," *Nature*, vol. 417, pp. 150–153, 2002.

[134] V. V. Afanasyev, Y. S. Kivshar, V. V. Konotop, and V. N. Serkin, "Dynamics of coupled dark and bright optical solitons," *Optics Letters*, vol. 14, pp. 805–807, Aug 1989.

[135] Y. Kivshar and G. Agrawal, *Optical Solitons: From Fibers to Photonic Crystals*. Academic Press, 2001.

[136] K. Bhambri and N. Gupta, "Dispersion managed solitons transmission in 54,000 km optical link," in *Radar, Communication and Computing (ICRCC), 2012 International Conference on*, pp. 312–314, IEEE, 2012.

[137] J. Zhang, Q. Lin, G. Piredda, R. W. Boyd, G. P. Agrawal, and P. M. Fauchet, "Optical solitons in a silicon waveguide," *Opt. Express*, vol. 15, pp. 7682–7688, Jun 2007.

[138] A. Shabat and V. Zakharov, "Exact theory of two-dimensional self-focusing and one-dimensional self-modulation of waves in nonlinear media," *Soviet Physics JETP*, vol. 34, no. 1, pp. 62–69, 1972.

[139] V. Tikhonenko, J. Christou, and B. Luther-Davies, "Three Dimensional Bright Spatial Soliton Collision and Fusion in a Saturable Nonlinear Medium," *Phys. Rev. Lett.*, vol. 76, pp. 2698–2701, Apr 1996.

[140] A. R. Seadawy and D. Lu, "Bright and dark solitary wave soliton solutions for the generalized higher order nonlinear schrdinger equation and its stability," *Results in Physics*, vol. 7, pp. 43 – 48, 2017.

[141] D. R. Andersen, D. E. Hooton, G. A. Swartzlander, and A. E. Kaplan, "Direct measurement of the transverse velocity of dark spatial solitons," *Opt. Lett.*, vol. 15, pp. 783–785, Jul 1990.

[142] G. A. Swartzlander, D. R. Andersen, J. J. Regan, H. Yin, and A. E. Kaplan, "Spatial dark-soliton stripes and grids in self-defocusing materials," *Phys. Rev. Lett.*, vol. 66, pp. 1583–1586, Mar 1991.

[143] A. Piccardi, A. Alberucci, and G. Assanto, "Dark Spatial Solitons in Liquid Crystals," *Molecular Crystals and Liquid Crystals*, vol. 558, no. 1, pp. 168–175, 2012.

[144] M. Taya, M. C. Bashaw, M. M. Fejer, M. Segev, and G. C. Valley, "Observation of dark photovoltaic spatial solitons," *Phys. Rev. A*, vol. 52, pp. 3095–3100, Oct 1995.

[145] G. Duree, M. Morin, G. Salamo, M. Segev, B. Crosignani, P. Di Porto, E. Sharp, and A. Yariv, "Dark photorefractive spatial solitons and photorefractive vortex solitons," *Phys. Rev. Lett.*, vol. 74, pp. 1978–1981, Mar 1995.

[146] J. K. Ranka, R. S. Windeler, and A. J. Stentz, "Visible continuum generation in air–silica microstructure optical fibers with anomalous dispersion at 800 nm," *Opt. Lett.*, vol. 25, pp. 25–27, Jan 2000.

[147] T. A. Birks, W. J. Wadsworth, and P. S. J. Russell, "Supercontinuum generation in tapered fibers," *Opt. Lett.*, vol. 25, pp. 1415–1417, Oct 2000.

[148] G. P. Agrawal, *Chapter2: Pulse propagation in Fibers*. Optics and Photonics Ser., Nonlinear Fiber Optics, Elsevier Science & Technology, 2006.

[149] A. M. Weiner, J. P. Heritage, R. J. Hawkins, R. N. Thurston, E. M. Kirschner, D. E. Leaird, and W. J. Tomlinson, "Experimental Observation of the Fundamental Dark Soliton in Optical Fibers," *Phys. Rev. Lett.*, vol. 61, pp. 2445–2448, Nov 1988.

[150] P. Emplit, J. Hamaide, F. Reynaud, C. Froehly, and A. Barthelemy, "Picosecond steps and dark pulses through nonlinear single mode fibers," *Optics Communications*, vol. 62, no. 6, pp. 374 – 379, 1987.

[151] I. Amiri, A. Afroozeh, I. Nawi, M. Jalil, A. Mohamad, J. Ali, and P. Yupapin, "Dark Soliton Array for communication security," *Procedia Engineering*, vol. 8, pp. 417–422, 2011.

[152] D. Tang, J. Guo, Y. Song, H. Zhang, L. Zhao, and D. Shen, "Dark soliton fiber lasers," *Optics express*, vol. 22, no. 16, pp. 19831–19837, 2014.

[153] L. Khaykovich, F. Schreck, G. Ferrari, T. Bourdel, J. Cubizolles, L. D. Carr, Y. Castin, and C. Salomon, "Formation of a Matter-Wave Bright Soliton," *Science*, vol. 296, no. May, pp. 1290–1294, 2002.

[154] S. Burger, K. Bongs, S. Dettmer, W. Ertmer, K. Sengstock, A. Sanpera, G. V. Shlyapnikov, and M. Lewenstein, "Dark Solitons in Bose-Einstein Condensates," *Phys. Rev. Lett.*, vol. 83, pp. 5198–5201, Dec 1999.

[155] J. Denschlag, J. E. Simsarian, D. L. Feder, C. W. Clark, L. A. Collins, J. Cubizolles, L. Deng, E. W. Hagley, K. Helmerson, W. P. Reinhardt, S. L. Rolston, B. I. Schneider, and W. D. Phillips, "Generating Solitons by Phase Engineering of a Bose-Einstein Condensate," *Science*, vol. 287, no. 5450, pp. 97–101, 2000.

[156] H. Sakaguchi and B. Malomed, "Positive- and negative-mass solitons in Bose-Einstein condensates with optical lattices," *Mathematics and Computers in Simulation*, vol. 69, no. 5, pp. 492 – 501, 2005. Nonlinear Waves: Computation and Theory IV.

[157] B. Eiermann, T. Anker, M. Albiez, M. Taglieber, P. Treutlein, K.-P. Marzlin, and M. K. Oberthaler, "Bright bose-einstein gap solitons of atoms with repulsive interaction," *Phys. Rev. Lett.*, vol. 92, p. 230401, Jun 2004.

[158] D. N. Christodoulides and R. I. Joseph, "Vector solitons in birefringent nonlinear dispersive media," *Opt. Lett.*, vol. 13, pp. 53–55, Jan 1988.

[159] M. Segev, G. C. Valley, S. R. Singh, M. I. Carvalho, and D. N. Christodoulides, "Vector photorefractive spatial solitons," *Opt. Lett.*, vol. 20, pp. 1764–1766, Sep 1995.

[160] M. Marconi, J. Javaloyes, S. Barland, S. Balle, and M. Giudici, "Vectorial dissipative solitons in vertical-cavity surface-emitting lasers with delays," *Nature Photonics*, vol. 9, pp. 450–455, 2015.

[161] S. T. Cundiff, B. C. Collings, N. N. Akhmediev, J. M. Soto-Crespo, K. Bergman, and W. H. Knox, "Observation of Polarization-Locked Vector Solitons in an Optical Fiber," *Phys. Rev. Lett.*, vol. 82, pp. 3988–3991, May 1999.

[162] A. Baas, J. P. Karr, H. Eleuch, and E. Giacobino, "Optical bistability in semiconductor microcavities," *Phys. Rev. A*, vol. 69, p. 023809, Feb 2004.

[163] V. B. Taranenko, C. O. Weiss, and B. Schäpers, "From coherent to incoherent hexagonal patterns in semiconductor resonators," *Phys. Rev. A*, vol. 65, p. 013812, Dec 2001.

[164] P. M. Walker, L. Tinkler, D. V. Skryabin, A. Yulin, B. Royall, I. Farrer, D. A. Ritchie, M. S. Skolnick, and D. N. Krizhanovskii, "Ultra-low-power hybrid light-matter solitons," *Nature Communications*, vol. 6 article number: 8317, 2015.

[165] A. Amo, S. Pigeon, D. Sanvitto, V. G. Sala, R. Hivet, I. Carusotto, F. Pisanello, G. Leménager, R. Houdré, E. Giacobino, C. Ciuti, and A. Bramati, "Polariton Superfluids Reveal Quantum Hydrodynamic Solitons," *Science*, vol. 332, no. 6034, pp. 1167–1170, 2011.

[166] I. Carusotto, S. X. Hu, L. A. Collins, and A. Smerzi, "Bogoliubov-Čerenkov Radiation in a Bose-Einstein Condensate Flowing against an Obstacle," *Phys. Rev. Lett.*, vol. 97, p. 260403, Dec 2006.

[167] S. Pigeon, I. Carusotto, and C. Ciuti, "Hydrodynamic nucleation of vortices and solitons in a resonantly excited polariton superfluid," *Physical Review B*, vol. 83, no. 144513, pp. 1–6, 2011.

[168] P. Cilibrizzi, H. Ohadi, T. Ostatnicky, A. Askitopoulos, W. Langbein, and P. Lagoudakis, "Linear wave dynamics explains observations attributed to dark solitons in a polariton quantum fluid," *Phys. Rev. Lett.*, vol. 113, p. 103901, Sep 2014.

[169] P. M. Walker, L. Tinkler, B. Royall, D. V. Skryabin, I. Farrer, D. A. Ritchie, M. S. Skolnick, and D. N. Krizhanovskii, "Dark Solitons in High Velocity Waveguide Polariton Fluids," *Physical Review Letters*, vol. 119, no. 9, p. 097403, 2017.

[170] B. Nelsen, G. Liu, M. Steger, D. W. Snoke, R. Balili, K. West, and L. Pfeiffer, "Dissipationless Flow and Sharp Threshold of a Polariton Condensate with Long Lifetime," *Phys. Rev. X*, vol. 3, p. 041015, Nov 2013.

[171] O. A. Egorov, D. V. Skryabin, A. V. Yulin, and F. Lederer, "Bright cavity polariton solitons," *Phys. Rev. Lett.*, vol. 102, p. 153904, Apr 2009.

[172] O. A. Egorov, A. V. Gorbach, F. Lederer, and D. V. Skryabin, "Two-dimensional localization of exciton polaritons in microcavities," *Phys. Rev. Lett.*, vol. 105, p. 073903, Aug 2010.

[173] M. Sich, D. V. Skryabin, and D. N. Krizhanovskii, "Soliton physics with semiconductor exciton-polaritons in confined systems," *Comptes Rendus Physique*, vol. 17, no. 8, pp. 908 – 919, 2016. Polariton physics / Physique des polaritons.

[174] T. Gao, P. S. Eldridge, T. C. H. Liew, S. I. Tsintzos, G. Stavrinidis, G. Deligeorgis, Z. Hatzopoulos, and P. G. Savvidis, "Polariton condensate transistor switch," *Phys. Rev. B*, vol. 85, p. 235102, Jun 2012.

[175] D. Tanese, H. Flayac, D. Solnyshkov, A. Amo, A. Lemaître, E. Galopin, R. Braive, P. Senellart, I. Sagnes, G. Malpuech, and J. Bloch, "Polariton condensation in solitonic gap states in a one-dimensional periodic potential," *Nature Communications*, vol. 4, article number: 1749, 2013.

[176] J. K. Chana, *Dynamics of Nonlinear Polariton Wavepackets and Pattern Formation in Microcavity Structures*. PhD thesis, University of Sheffield, 2016.

[177] M. Sich, J. K. Chana, O. A. Egorov, H. Sigurdsson, I. A. Shelykh, D. V. Skryabin, P. M. Walker, E. Clarke, B. Royall, M. S. Skolnick, and D. N.

Krizhanovskii, "Transition from Propagating Polariton Solitons to a Standing Wave Condensate Induced by Interactions," *Physical Review Letters*, vol. 120, no. 167402, 2018.

[178] L. Tinkler, P. M. Walker, E. Clarke, D. N. Krizhanovskii, F. Bastiman, M. Durska, and M. S. Skolnick, "Design and characterization of high optical quality InGaAs/GaAs/AlGaAs-based polariton microcavities," *Applied Physics Letters*, vol. 106, p. 021109, 2015.

[179] L. E. T. Rodriguez, P. M. Walker, H. Sigurdsson, B. Royall, I. Farrer, D. A. Ritchie, A. V. Yulin, I. A. Shelykh, M. S. Skolnick, and D. N. Krizhanovskii, "Amplification of nonlinear polariton pulses in waveguides," *Opt. Express*, vol. 27, pp. 10692–10704, Apr 2019.

[180] D. D. Solnyshkov, H. Tercas, and G. Malpuech, "Optical amplifier based on guided polaritons in GaN and ZnO," *Applied Physics Letters*, vol. 105, no. 231102, 2014.

[181] O. Jamadi, F. Réveret, P. Disseix, F. Médard, J. Leymarie, A. Moreau, D. Solnyshkov, C. Deparis, M. Leroux, J. Zuniga-Perez, and G. Malpuech, "Edge-emitting polariton laser and amplifier based on a ZnO waveguide," *Light: Science and Applications*, vol. 7, article number: 82, 2018.

[182] N. A. Olsson, "Lightwave systems with optical amplifiers," *Journal of Lightwave Technology*, vol. 7, no. 7, pp. 1071–1082, 1989.

[183] G. P. Agrawal and N. A. Olsson, "Self-phase modulation and spectral broadening of optical pulses in semiconductor laser amplifiers," *IEEE Journal of Quantum Electronics*, vol. 25, no. 11, pp. 2297–2306, 1989.

[184] S. V. Suchkov, A. A. Sukhorukov, J. Huang, S. V. Dmitriev, C. Lee, and Y. S. Kivshar, "Nonlinear switching and solitons in PT-symmetric photonic systems," *Laser and Photonics Reviews*, vol. 10, no. 2, pp. 177–213, 2016.

[185] V. V. Konotop, J. Yang, and D. A. Zezyulin, "Nonlinear waves in PT - symmetric systems," *Reviews of Modern Physics*, vol. 88, no. 3, pp. 1–59, 2016.

[186] C. E. Rüter, K. G. Makris, R. El-Ganainy, D. N. Christodoulides, M. Segev, and D. Kip, "Observation of parity-time symmetry in optics," *Nature Physics*, vol. 6, no. 3, pp. 192–195, 2010.

[187] W. Chen, S. K. Özdemir, G. Zhao, J. Wiersig, and L. Yang, "Exceptional points enhance sensing in an optical microcavity," *Nature*, vol. 548, pp. 192–196, 2017.

[188] K. Inoue, T. Mukai, and T. Saitoh, "Gain saturation dependence on signal wavelength in a travelling-wave semiconductor laser amplifier," *Electronics Letters*, vol. 23, pp. 328 – 329, 02 1987.

[189] R. Huang, F. Tassone, and Y. Yamamoto, "Experimental evidence of stimulated scattering of excitons into microcavity polaritons," *Physical Review B*, vol. 61, no. 12, p. R7854, 2000.

[190] A. Brichkin, S. Novikov, A. Larionov, V. Kulakovskii, M. Glazov, C. Schneider, S. Höfling, M. Kamp, and A. Forchel, "Effect of Coulomb interaction on exciton-polariton condensates in GaAs pillar microcavities," *Physical Review B*, vol. 84, no. 19, p. 195301, 2011.

[191] D. V. Skryabin, Y. V. Kartashov, O. A. Egorov, M. Sich, J. K. Chana, L. E. Tapia Rodriguez, P. M. Walker, E. Clarke, B. Royall, M. S. Skolnick, and D. N. Krizhanovskii, "Backward Cherenkov radiation emitted by polariton solitons in a microcavity wire," *Nature Communications*, vol. 8, article number: 1554, 2017.

[192] J. V. Velley, "Cerenkov radiation and its applications," *British Journal of Applied Physics*, vol. 6, p. 227, 1955.

[193] A. N. Laboratory, "Advanced Test Reactor core, Idaho National Laboratory." Available at *https : //commons.wikimedia.org/wiki/File : Advanced_Test_Reactor.jpg*.

[194] V. G. Veselago, "The electrodynamics of substances with simultaneously negative values of ϵ AND μ," *Soviet Physics Uspekhi*, vol. 10, no. 4, pp. 509–514, 1968.

[195] Z. Duan, X. Tang, Z. Wang, Y. Zhang, X. Chen, M. Chen, and Y. Gong, "Observation of the reversed Cherenkov radiation," *Nature Communications*, vol. 8, no. 4, p. 14901, 2017.

[196] N. Akhmediev and M. Karlsson, "Cherenkov radiation emitted by solitons in optical fibers," *Physical Review A*, vol. 51, no. 3, pp. 2602–2607, 1995.

[197] P. K. A. Wai, C. R. Menyuk, H. H. Chen, and Y. C. Lee, "Soliton at the zero-group-dispersion wavelength of a single-model fiber," *Opt. Lett.*, vol. 12, pp. 628–630, Aug 1987.

[198] A. Efimov, A. V. Yulin, D. V. Skryabin, J. C. Knight, N. Joly, F. G. Omenetto, A. J. Taylor, and P. Russell, "Interaction of an optical soliton with a dispersive wave," *Phys. Rev. Lett.*, vol. 95, p. 213902, Nov 2005.

[199] V. Brasch, M. Geiselmann, T. Herr, G. Lihachev, M. Pfeiffer, M. L. Gorodetsky, and T. J. Kippenberg, "Photonic chip–based optical frequency comb using soliton Cherenkov radiation," *Science*, vol. 351, no. 6271, pp. 357–360, 2016.

[200] G. Dasbach, M. Schwab, M. Bayer, D. Krizhanovskii, and A. Forchel, "Tailoring the polariton dispersion by optical confinement: Access to a manifold of elastic polariton pair scattering channels," *Physical Review B*, vol. 66, no. 20, p. 201201, 2002.

[201] G. Slavcheva, A. Gorbach, A. Pimenov, A. Vladimirov, and D. Skryabin, "Multi-stability and polariton solitons in microcavity wires," *Optics letters*, vol. 40, no. 8, pp. 1787–1790, 2015.

[202] C. Antón, T. C. H. Liew, G. Tosi, M. D. Martín, T. Gao, Z. Hatzopoulos, P. S. Eldridge, P. G. Savvidis, and L. Viña, "Energy relaxation of exciton-polariton condensates in quasi-one-dimensional microcavities," *Phys. Rev. B*, vol. 88, p. 035313, Jul 2013.

[203] D. Sanvitto and S. Kéna-Cohen, "The road towards polaritonic devices," *Nature Materials*, vol. 15, no. 10, pp. 1061–1073, 2016.

[204] M. Sich, L. E. Tapia-Rodriguez, H. Sigurdsson, P. M. Walker, E. Clarke, I. A. Shelykh, B. Royall, E. S. Sedov, A. V. Kavokin, D. V. Skryabin, M. S. Skolnick, and D. N. Krizhanovskii, "Spin Domains in One-Dimensional Conservative Polariton Solitons," *ACS Photonics*, vol. 5, no. 12, pp. 5095–5102, 2018.

[205] D. D. Solnyshkov, R. Johne, I. A. Shelykh, and G. Malpuech, "Chaotic josephson oscillations of exciton-polaritons and their applications," *Phys. Rev. B*, vol. 80, p. 235303, Dec 2009.

[206] E. London, "How principles of domain formation in model membranes may explain ambiguities concerning lipid raft formation in cells," *Biochimica et Biophysica Acta (BBA) - Molecular Cell Research*, vol. 1746, no. 3, pp. 203 – 220, 2005. Lipid Rafts: From Model Membranes to Cells.

[207] A. L. Berkhoer and V. Zakharov, "Self Excitation of Waves with Different Polarizations in Nonlinear Media," *Soviet Journal of Experimental and Theoretical Physics*, vol. 31, no. 3, p. 486, 1970.

[208] A. P. Sheppard and M. Haelterman, "Polarization-domain solitary waves of circular symmetry in Kerr media," *Opt. Lett.*, vol. 19, pp. 859–861, Jun 1994.

[209] M. Gilles, P.-Y. Bony, J. Garnier, A. Picozzi, M. Guasoni, and J. Fatome, "Polarization domain walls in optical fibres as topological bits for data transmission," *Nature Photonics*, vol. 11, pp. 102–107, 2017.

[210] T. Gao, C. Antón, T. C. H. Liew, M. D. Martín, Z. Hatzopoulos, L. Viña, P. S. Eldridge, and P. G. Savvidis, "Spin selective filtering of polariton condensate flow," *Applied Physics Letters*, vol. 107, no. 1, p. 011106, 2015.

[211] M. Sich, F. Fras, J. K. Chana, M. S. Skolnick, D. N. Krizhanovskii, A. V. Gorbach, R. Hartley, D. V. Skryabin, S. S. Gavrilov, E. A. Cerda-Méndez, K. Biermann, R. Hey, and P. V. Santos, "Effects of spin-dependent interactions on polarization of bright polariton solitons," *Phys. Rev. Lett.*, vol. 112, p. 046403, Jan 2014.

[212] K. V. Kavokin, I. A. Shelykh, A. V. Kavokin, G. Malpuech, and P. Bigenwald, "Quantum theory of spin dynamics of exciton-polaritons in microcavities," *Phys. Rev. Lett.*, vol. 92, p. 017401, Jan 2004.

[213] A. Amo, T. C. H. Liew, C. Adrados, E. Giacobino, A. V. Kavokin, and A. Bramati, "Anisotropic optical spin Hall effect in semiconductor microcavities," *Phys. Rev. B*, vol. 80, p. 165325, Oct 2009.

[214] M. M. Glazov and L. E. Golub, "Spin and transport effects in quantum microcavities with polarization splitting," *Phys. Rev. B*, vol. 82, p. 085315, Aug 2010.

[215] W. Langbein, I. Shelykh, D. Solnyshkov, G. Malpuech, Y. Rubo, and A. Kavokin, "Polarization beats in ballistic propagation of exciton-polaritons in microcavities," *Phys. Rev. B*, vol. 75, p. 075323, Feb 2007.

[216] J. Ciers, J. G. Roch, J.-F. Carlin, G. Jacopin, R. Butté, and N. Grandjean, "Propagating polaritons in iii-nitride slab waveguides," *Phys. Rev. Applied*, vol. 7, p. 034019, Mar 2017.

[217] T. Karzig, C.-E. Bardyn, N. H. Lindner, and G. Refael, "Topological polaritons," *Phys. Rev. X*, vol. 5, p. 031001, Jul 2015.

[218] Y. Lumer, Y. Plotnik, M. C. Rechtsman, and M. Segev, "Self-localized states in photonic topological insulators," *Phys. Rev. Lett.*, vol. 111, p. 243905, Dec 2013.

[219] D. R. Gulevich, D. Yudin, D. V. Skryabin, I. V. Iorsh, and I. A. Shelykh, "Exploring nonlinear topological states of matter with exciton-polaritons: Edge solitons in kagome lattice," *Scientific Reports*, vol. 7, no. 1780, pp. 2045–2322, 2017.